WESTERN ALEUTIAN VOLCANISM; DEFINING MAGMATIC SERIES TRANSITIONS AND PETROGENETIC ORIGINS

by

SAMUEL OXHORN

(Under the Direction of MATTIA PISTONE)

ABSTRACT

Western Aleutian volcanoes have been characterized as erupting predominantly high Mg# [(MgO/(MgO+FeO)*100) >60)] calc-alkaline andesites that distinguish them from all other volcanic centers within the Aleutian arc. By using a combination of whole-rock chemistry and mineral chemistry analysis, thermobarometry, and thermodynamic modeling, a gradational shift in both primary magmatic composition and subsequent differentiation trends is present within the distal Aleutians. Evidence is presented for classifying Gareloi (179°W) as a high-K tholeiitic volcanic center with magmas predominantly differentiated in a shallow crustal reservoir (1–4 kbar) and Kiska (182°W) as a calc-alkaline center with magmas that have undergone polybaric differentiation at 0.8–3.9 kbar and 4.6–7.5 kbar. A common high-Al basalt parent is proposed for both volcanoes. West of Kiska, magmas have high Mg# (>60), Sr/Y (>50), and La/Yb (>9) suggesting a transitional shift to magmas influenced by a subducted slab melt of mid-ocean ridge basalt (MORB) at eclogite facies.

INDEX WORDS: Volcanology, Petrology, Geochemistry, Aleutian Arc, Subduction Zone

WESTERN ALEUTIAN VOLCANISM; DEFINING MAGMATIC SERIES TRANSITIONS AND PETROGENETIC ORIGINS

by

SAMUEL OXHORN

B.S., University of Florida, 2019

A Thesis Submitted to the Graduate Faculty of The University of Georgia in Partial Fulfillment of the Requirements for the Degree

MASTER OF SCIENCE

ATHENS, GEORGIA

2022

WESTERN ALEUTIAN VOLCANISM; DEFINING MAGMATIC SERIES TRANSITIONS AND PETROGENETIC ORIGINS

by

SAMUEL OXHORN

Major Professor:	Mattia Pistone
Committee:	Douglas E. Crowe
	Michael R. Perfit

Electronic Version Approved:

Ron Walcott
Vice Provost for Graduate Education and Dean of the Graduate School
The University of Georgia
May 2022

ACKNOWLEDGEMENTS

I would like to thank Mattia Pistone for his support and encouragement in pursuing my interest in Aleutian volcanism. His willingness to always put in time for my questions, even if it meant working late nights and weekends, made this thesis possible. I would like to thank Michael Perfit for making me a petrologist and sparking my interest in the Aleutians. I would like to thank Doug Crowe for introducing me to the world of economic geology. I give special thanks to Steve Holland for his phenomenal course in data analysis. His instruction in using R has been instrumental in completing this thesis. I would like to thank the UGA Geology Department for their support and funding. I would like to thank the Marine Geological Samples Laboratory of the Graduate School of Oceanography of the University of Rhode Island for providing samples from Kiska. I would like to thank the Geological Society of America Mineralogy, Geochemistry, Petrology, & Volcanology Division for providing funding for this project through the Lipman Research Award. Lastly, I would like to thank my Australian Cattle Dog Naboo for her tireless dedication to sleeping on the couch behind me while I wrote this entire thesis.

TABLE OF CONTENTS

LIST OF TABLES

Page

LIST OF FIGURES

Page

CHAPTER 1

INTRODUCTION

The distal portion of the Aleutian volcanic arc (177°W–187°W; Fig.1A) remains an elusive yet important area of study within the geosciences. This is in part due to its geographic remoteness, association with juvenile continental crust production (Kelemen et al., 2003a), volcanic hazards (Coombs et al., 2008), and as a key area to determine the processes that drive island arc magmatic differentiation trends (Yogodzinski et al., 2010). Within the past decade, the region has seen a marked increase in bulk major and trace element chemistry data for active volcanoes. In many instances, these data have not been fully utilized to address magmatic differentiation trends at individual volcanic centers, nor along-strike trends.

An important distinction must be made between the terms primary, primitive, and parental when describing a magma. A primary magma is one that has not been modified since leaving its source. Primitive magmas (Mg# >60) are those that have undergone minimal fractionation or contamination. Parental magmas are those that more evolved magmas are thought to be derived from (Gust and Perfit, 1987). Magmatic compositions within the distal Aleutians have been characterized as predominately primitive calc-alkaline andesites derived from a primary hybrid melt of subducted slab basalt at eclogites facies and mantle peridotite (Kelemen et al., 2003a). However, recent studies have reported that multiple active volcanoes within the region have been found to follow a tholeiitic differentiation trend (e.g. Coombs et al., 2012, Coombs et al., 2018). Early in this study, a gradational along-strike linear shift from tholeiitic (e.g. Gareloi) to highly calc-alkaline (e.g. Western Cones) magmas was discovered within the region (Fig. 2). Tholeiitic

magmas are more characteristic of the central portion of the arc and are hypothesized to evolve predominately by shallow crustal fractional crystallization of basalts (Kay and Kay, 1994). In contrast, the highly calc-alkaline magmas of the western sea floor lavas consist of primitive (Mg# >60) andesitic–rhyolitic rocks hypothesized to derive their anomalous geochemical signature predominately from the interaction between subducted basalt at eclogite facies with peridotite in the mantle wedge (Yogodzinski et al., 2015). Given the spatial continuum in magmatic series present within the distal Aleutians, this study will assess the hypothesis that magmas in the eastern portion of the distal Aleutians are differentiated primarily by shallow crustal fractional crystallization and that differentiation gradationally shifts to greater depths westward until subsiding at the Western Cones wherein magmas are near primary mantle melts.

To test this hypothesis, new samples as well published data from previous studies have been analyzed to assess along-strike variations in geochemical composition and associated differentiation trends for all active volcanoes within the region. A particular emphasis has been placed on Gareloi (179°W) and Kiska (182°W) volcanoes which both serve as compositional endmember volcanoes that reside on crust of relatively equal thickness (38.5 ± 2.9 km; Janiszewski et al., 2013). Gareloi has been characterized as a predominately high-K tholeiitic volcanic center (Coombs et al., 2012). Whereas Kiska samples prior to this study were sparse but followed an apparent calc-alkaline trend (Miller et al., 1998). This study presents the results of a combination of whole-rock chemistry analysis for all distal Aleutian volcanoes, mineral chemistry analysis and thermobarometry for Gareloi and Kiska volcanoes, as well as thermodynamic modeling. The results indicate a gradational shift in both primary magmatic composition and subsequent differentiation trends within the distal Aleutians. A transition from the common Aleutian primary magma generated by partial melting of mantle peridotite grades to an end member primary magma

influenced by a subducted slab basaltic melt at eclogite facies. This unique transitional feature of distal Aleutians magmas makes the region one of the most important subduction zone segments on the planet for understanding the petrogenesis of magmas underlying volcanic arcs.

CHAPTER 2

GEOLOGY

The Aleutian Subduction Zone

The Aleutian volcanic arc spans over 4,000 km from mainland Alaska in the east to the Kamchatka Peninsula in the west (Fig.1; Buurman et al., 2014). Within its boundaries are over eighty major volcanoes which have erupted throughout the Holocene, making the arc one of the most volcanically active locations on the planet (Miller et al., 1998). The arc and its associated volcanism are often inferred to be the result of the northwestward subduction of the Pacific Plate beneath the North American Plate (e.g. Fournelle et al., 1994). However, seismic data suggests the presence of an independent Bering plate that is undergoing slow clockwise rotation as a result of terrane accretion in southern Alaska (Mackey et al., 1997). Therefore, the Aleutian arc resides along the boundary of the Pacific and Bearing plate (Jicha and Kay, 2018). Based on $^{40}Ar/^{39}Ar$ radiometric dating of plutonic, submarine, and subaerial rocks, volcanism is thought to have initiated in the Middle Eocene (~46 Ma; Jicha et al., 2006). This timing is coincident with the shift in trajectory of the Pacific Plate relative to the Hawaiian hot spot (Duncan and Keller, 2004). The age of the subducting lithosphere entering the Aleutian trench does not change along strike of the arc (~50–60 Ma; Geist et al., 1988; Atwater, 1989). The back-arc region of the Aleutians consists of a trapped piece of Mesozoic oceanic crust and therefore no back-arc spreading has occurred (Kay and Kay, 1994). A transition from continental to oceanic crust is present at the break in the slope of the continental shelf at 164°W (House and Jacob, 1983).

Pacific Plate motion in the east is nearly orthogonal to the trench and becomes increasingly oblique within the western portion of the arc (Fig. 1A–B; Syracuse and Abers, 2006; Buurman et al., 2014). The change in plate motion direction results in the orthogonal convergence rate being ~65–75 mm/yr east of Adak Island (176°W) and <40 mm/yr west of Adak Island (Kelemen et al., 2003a). A transtensional regime is present in the overriding plate of the central-western arc due to the oblique subduction which resulted in the formation of northwest-southeast-oriented right-lateral strike-slip faults (Scholl, 2007). These strike-slip faults have segmented the central and western Aleutian Arc basement into five crustal blocks which have undergone clockwise rotation and are separated by deep submarine canyons (Fig. 1A).

Based on the orthogonal convergence rate, Kelemen et al., (2003b) calculated that the sediment flux entering the subduction zone increases systematically westward from 67 m^3 of sediment per meter of arc length per year (m^3/m/yr) at Cold Bay (163°W) to ~95 m^3/m/yr at Seguam (172.5°W). West of Seguam, sediment flux decreases along-strike to ~20m^3/m/yr in the Komandorsky region. The composition of subducted sediment also shifts from being predominantly terrigenous in the east to pelagic clay in the west as indicated by elevated Nd/Hf (Yogodzinski et al., 2010).

In addition to sediment flux, the westward decrease in orthogonal convergence rate results in increased conductive cooling of the mantle wedge and increased heating of the subducting plate (Kincaid and Sacks, 1997). This shift in thermal regime may lead to: 1) dehydration reactions in the subducting lithosphere occurring at shallower depths resulting in less H_2O being available to flux the mantle wedge, 2) increased partial melting of subducted material occurring at shallower depths, 3) limited partial melting in the overlying colder mantle, 4) the occurrence of crystal fractionation occurring at higher pressures; potentially even below

the seismic Moho discontinuity due to a cooler upper mantle and lower crust (Kelemen et al., 2003a). As a result, magmatic flux from the mantle would be limited (Kelemen et al., 2003a). This hypothesis is corroborated by the fact that none of the emergent western Aleutian volcanoes besides Tanaga are as large as the 20 largest volcanoes in the central Aleutians (Fournelle et al., 1994).

The thickness of the crust is thought to be uniform (~25–30 km) within the oceanic crustal portion of the arc (Holbrook et al., 1999; Shillington et al., 2004). These studies relied solely on primary (*P*) wave velocities. The relationship between *P* wave velocity and ultramafic–mafic compositions has been noted to be ambiguous (Behn and Kelemen, 2003). An alternate estimate utilized both *P* and *S* wave velocities and suggests that the average crustal thickness is generally uniform at 38.5 ± 2.9 km along the entire arc (Janiszewski et al., 2013). Due to strike slip faulting and arc-parallel lateral extension, volcanism has progressively moved northward since its inception in the middle Eocene (Scholl et al., 1987). Concurrently, the volcanic front migrates northward off of the ridge axis west of Buldir. Attu resides on only 27.5 km of crust (Janiszewski et al., 2013) and the submarine Western Cones and Piip seamount reside on the oceanic lithosphere of the Bering Sea which is inferred to be only ~10 km thick (Yogodzinski et al., 2015).

The geochemical composition of the arc crust is thought to be uniform along-strike of the subduction zone (Kelemen et al., 2003b). Geophysical studies of the arc indicate that the arc consists of three layers. The upper crust layer (~7 km) is inferred to consist of both extrusive igneous rocks of varying composition as well as volcaniclastic sediments (Holbrook et al., 1999). The mid-crustal layer (~7–20 km) is inferred to consist of basaltic to andesitic rocks formed from either intrusions or the remains of the oceanic crust on which the arc was built (Holbrook et al.,

1999; Shillington et al., 2004; Janiszewski et al., 2013). The lower crust (~20–35 km) is inferred to consist of ultramafic–mafic cumulates and/or granulites (Holbrook et al., 1999; Shillington et al., 2004).

Further evidence that corroborates geophysical studies for crustal composition of the Aleutian arc comes from the Talkeetna paleo-island arc section located in south-central Alaska. The island arc accreted to the North American plate in the Early to Middle Jurassic (~200–175 ma; Burns, 1985; DeBari and Coleman, 1989). The relic arc provides a rare, near complete exposure of island arc upper mantle and crust critical for relating deep magmatic processes to extrusive volcanic deposits. The exposure consists of residual mantle peridotite overlain by pyroxenite which is capped by gabbronorite (Fig. 3; Greene et al., 2006). The lower crust consists of layered gabbronorite and is ~10 km thick. The middle crust consists of a combination of diorites, tonalites, and gabbros. The upper crust is comprised of lavas, tuffs, and volcaniclastic debris-flow deposits from the Talkeetna Volcanic Formation which range in composition from basalt to rhyolite.

The uniformity in subduction plate age, obducting plate crustal thickness and composition, coupled with the along-strike shift in subduction orientation, is unique to the Aleutian arc. This makes the arc one of most important localities on the planet to address how a varying subduction regime influences magmatic petrogenesis, differentiation trends, and ultimately the genesis of juvenile continental crust. The distal Aleutians in particular comprises a major portion of the arc, yet from a geochemical and petrological perspective, remains a relatively unexplored locality which may play a key role in unraveling the petrogenesis of Aleutian magmas and their subsequent differentiation trends.

The Distal Aleutians

This project will follow the regional divisions proposed by Kelemen et al. (2003a) wherein the "western Aleutians" are delineated as the portion of the arc west of 174°W. Additionally, longitude will be designated in "°W" to avoid confusion when crossing the International Date Line. Within this framework, the western Aleutians are categorized into three regions: "the Adak area" (174–177°W), the distal Aleutians (177–187°W), and the Komandorsky block (188–195°W). The focus of this project is the distal Aleutians. Specifically, from Gareloi (179°W) to the Western Cones of Yogodzinski et al. (2015) (~188°W; Fig. 4A). The Western Cones are technically in the Komandorsky block but will be included as they provide a way to investigate how the presence of thin oceanic lithosphere modulates magmatic compositions within the region. From east to west the active volcanoes within the distal Aleutians are Gareloi, Semisopochnoi, Little Sitkin, Kiska, Buldir, ~134 submarine volcanic cones within the Ingenstrem Depression, and 5 submarine Western Cones (Fig. 4A). Relative to the central/eastern Aleutians, the dip of the slab is greater in the distal Aleutians (Fig. 1C; e.g. 57° at Gareloi). However, slab dip decreases by 11° from Kiska to Buldir. The inferred depth to the slab increases from 71 km at Gareloi to 106 km at Semisopochnoi (Fig. 1D; Syracuse and Abers, 2006). Further west, slab depth decreases to 78 km at Buldir.

The presence of a tear in the subducting Pacific Plate proximal to the Aleutian-Kamchatka junction may play a significant role in the thermal regime underlying the Komandorsky block and the distal Aleutians (Yogodzinski et al., 2001). In conjunction with a decrease in the orthogonal convergence rate outlined above (Fig. 1B), this tear in the Pacific plate may cause increased heating of the subducting plate by asthenospheric flow (Fig. 4B).

Consequently, these shifts in subducted plate dip, depth, and temperature may have profound impacts in primary magma genesis within the region.

Gareloi

Gareloi volcano (179°W) comprises the majority of Gareloi Island. It is a stratovolcano that is 10 by 8 km and reaches 1,573 m above sea level (Miller et al., 1998). It has been one of the most active volcanoes within the Aleutian volcanic arc (Coombs et al., 2012). Compared to nearby Quaternary stratovolcanoes to the east and west, the volcano resides on an irregularly shaped portion of the arc resulting in it residing north of the summit plateau of the Aleutian Ridge (Fig. 4A; Coombs et al, 2012). There are two summits: North Peak (1,573 m) and South Peak (1,510 m), both are separated by a narrow saddle. North Peak contains a 300 by 350 m crater ~100 m deep. South Peak has a crater with a width of 300 m and is partially collapsed on the southern wall which is attributed to the largest recorded historical eruption that occurred in 1929 (Coombs et al., 2008). Both craters are noted for containing active fumaroles (Miller et al., 1998; Coombs et al., 2008; Fischer et al., 2021).

Volcanic activity on the island is thought to have occurred in two distinct phases separated by a prolonged gap with no eruptions taking place (Coats, 1959). The older volcanic rocks of the island (Pleistocene) consist of a sequence of olivine flow basalts and scoria beds. Coats (1959) suggests that these deposits are the eroded remnants of an older composite cone because an unconformity separates older deposits from more recent ones. Younger deposits are less eroded and are also primarily olivine basalt flows. Coats (1959) notes the presence of a 4.3 km long south-southeast trending fissure which consisted of 13 aligned craters attributed to the 1929 eruption (Fig. 5). The craters ranged in size from 80 to 1,600 m in diameter and produced blocky lava flows and an andesitic tuff deposit extending 2.5 by 5 km southeast of the volcano.

Subsequent field work updated the numbering scheme of Coats (1959) and now includes 16 total craters (Coombs et al., 2012).

The island is entirely composed of volcanic deposits (Pleistocene–Holocene) that include lava flow units and pyroclastic deposits (Coombs et al., 2012). The majority of samples from the island have been designated as high-K tholeiites and further categorized as latites and shoshonites as defined by Le Maitre et al. (2002). Samples from the 1929 eruption are the most differentiated and contain plagioclase, clinopyroxene, minor olivine, and rare hornblende. Latites and trachytes from crater 9 are noted for containing plagioclase, clinopyroxene, opaques, and olivine in decreasing order of abundance with amphibole present in trace amounts. One exception to the high-K tholeiitic trend on the island is reported as unit ASP (Coombs et al., 2012) which consists of andesitic lava flows erupted from South Peak. The samples are calc-alkaline and contain plagioclase, clinopyroxene, orthopyroxene, and oxides. Gareloi volcano remains active with the last confirmed eruption occurring on August 17th, 1989 (Miller et al., 1998).

Kiska

Kiska Volcano (183°W) is a Holocene stratovolcano situated on the northern end of Kiska Island (Fig. 6). At its base, it is 8.5 by 6.4 km in diameter and is 1221 m high at its peak (Miller et al., 1998). The summit contains a slightly elliptical crater approximately 0.4 km in diameter which is breached on the northern side. The Vega Formation occupies the southern side of the island and consists of faulted and deformed submarine volcanic and volcaniclastic units thought to be middle Tertiary in age (Coats et al., 1961). The Kiska Harbor Formation (Late Tertiary to early Pleistocene) unconformably overlies the Vega Formation and is the remnants of a composite stratovolcano inferred to have been located proximal to where the current volcano

resides (Coats et al., 1961). One sample of an andesitic lava flow deposit from the older volcano has a K-Ar age of 5.5+/−0.7 Ma (Marlow et al., 1973). On the northern tip of the island is Sirius Point; a parasitic cinder cone which formed on January 24, 1962 during an explosive eruption (Miller et al., 1998). Deposits from the Holocene cone contain interbedded lava flows and pyroclastic material with the latter containing hornblende (Coats et al., 1961). The lava flows range in thickness from 1 to 30 m and are described as grey, fine-grained porphyritic andesites. The five youngest flows analyzed during the reconnaissance of the island are augite-hypersthene andesites that contain minor olivine. The last recorded eruption occurred on June 1st, 1990 (Miller et al., 1998).

CHAPTER 3

ALEUTIAN MAGMATIC PETROGENESIS AND DIFFERENTATION

Magmatic Petrogenesis

The source of primary island arc magmas is a combination of a subducted slab component and the overlying mantle wedge (Gill, 1981). The subducted slab component may consist of oceanic basalt, overlying sediment, seawater, or likely a combination of all three (Kay, 1980). Most models rely on the mantle wedge solidus being depressed by volatiles from the subducted component (Davidson, 2013). In this scenario a range of primary magma compositions may be generated which in part is dictated by temperature, pressure, and melt fraction (Fig. 7; Kushiro, 2001). The resulting primary melt is enriched in large ion lithophile elements (LILE; e.g., Rb, K, Ba, Sr) and LREE (e.g. La, Ce, Pr, Nd). Conversely, it is relatively depleted in high field strength elements (HFSE; e.g., Nb, Ta, Zr, Ti, Hf) as well as middle and heavy rare earth elements (MREE and HREE; e.g. Dy, Er, Yb, Lu) (Wilson, 1989). This unique geochemical signature distinguishes arc magmas from magmas found in other tectonic settings on Earth, particularly mid-ocean ridge basalt (MORB).

High-Mg Basalt Parent

Primary magmas are rarely found at the surface, but primitive arc magmas which may be parental to most Aleutian arc magmas have been reported. One suggestion is that the most common parental magma within the arc is Mg-rich olivine tholeiitic basalt derived from mantle peridotite that has been metasomatized by material from the subducted plate (Perfit et al., 1980; Kay et al., 1982). The Mg-rich basalt may be derived from a picritic basalt that fractionates

olivine as it ascends through the mantle (Gust and Perfit, 1987). Regardless, high-Mg basalts attain a neutral level of buoyancy at the crust-mantle boundary or lower crust and stall. New pulses of high-Mg basalt from the mantle mix with evolved magmas and assimilation of crustal material may occur; producing high-Al basalt (Conrad and Kay, 1984; Gust and Perfit, 1987). This model parallels the concept of a MASH (Melt, Assimilation, Storage, Homogenization) zone (Hildreth and Moorbath, 1988) or deep crustal hot zone (Annen et al., 2006).

Once Al-rich basalt is produced, the five crustal blocks within the arc may exert primary control on further differentiation (Fig. 8; Kay et al., 1982; Kay and Kay, 1994). Tholeiitic volcanic centers are generally situated on the edge of or between block segments while calc-alkaline centers are generally in the middle of blocks. Tholeiitic end-member magmas develop in a tensional (dike-like) environment deriving their geochemical composition primarily from upper crustal isobaric fractional crystallization. Calc-alkaline magmatic differentiation predominately occurs at deeper crustal levels in a compressional (sill-like) environment which often includes magma mixing (Kay and Kay, 1994). The presence of amphibole and other mineral phases within calc-alkaline rocks that have disequilibrium textures suggests that ascent rate from the lower crust is relatively rapid (Kay and Kay, 1994).

High-Al Basalt Parent

In contrast, Myers et al. (1985) suggests that high-Al basalt is the dominant magmatic parent in the arc. High-Al basalt is inferred to have formed by partial melting of subducted sediment and crust at eclogite facies (Brophy and Marsh, 1986). The parental Al-rich basalt then ascends through the mantle lithosphere with minimal interaction between melt and mantle rock (Brophy, 1986). Once the high-Al basalt reaches the lower crust magmatic conduit maturity dictates whether a magma will follow a tholeiitic or calc-alkaline trend (Myers et al., 1985).

Calc-alkaline magmas are generated in immature, “dirty” magmatic conduits that are relatively cool in temperature and are geochemically influenced by assimilation of wall rock along with fractional crystallization. With time, heat and mass transfer chemically and thermally conditions the conduit and generates a boundary layer that insulates subsequent pulses of magma resulting in minimal contamination of ascending magmas from lithospheric debris (Myers et al., 1985). Consequently tholeiitic magmas are produced later on in a volcano’s life cycle. In this framework, high Mg-basalts are considered to be a by-product of interaction between high-Al basalt and upper mantle material (Myers et al., 1985; Brophy, 1986).

High Mg# Andesite

A subducted component which may rectify the two opposing viewpoints on Aleutian parental magmas is the presence of primitive high Mg# andesite that was first identified on Adak Island (Kay, 1978). In time these rocks were termed “adakites” by some researchers (e.g. Defant and Drummond, 1990). Adakites are noted for LREE (light rare earth element) enrichment (La/Yb >9), high Sr/Y (>50) and relatively depleted HREE and yttrium concentrations (e.g.,Y, 20 ppm, Yb <2 ppm) and were hypothesized to originate from direct partial melting of young, basaltic (MORB) slab with elevated temperatures in amphibolite or eclogite facies (Castillo, 2012). However as Kelemen et al. (2003b) notes, the original definition of “adakite” does not specify an acceptable range of Mg#. Additionally, the term has gone on to be used in a variety of contexts with the original geochemical constraints being modified (Castillo, 2012). Therefore following the criteria suggested by Kelemen et al. (2003b), this study will use the term high Mg# andesite instead of adakite.

Two types of high Mg# andesite have been noted to be present within the Aleutians (Yogodzinski et al., 1995): Adak-type and Piip-type andesite. Both are attributed in part to the

elevated temperature of the subducting slab and cooler mantle wedge caused by the oblique subduction regime present within the western Aleutians (Kelemen et al., 2003a). The Adak-type is noted for having a pronounced slab melt signature as indicated by high Sr, La/Yb, La/Ta, and low Ti/Hf relative to other Aleutian samples (Yogodzinski et al., 1995). The Piip-type is still a high Mg# andesite, but the aforementioned trace element trends are less pronounced. This diluted signature is thought to be due to reaction with mantle peridotite and/or basalt (Yogodzinski et al., 1995).

The presence of submarine volcanism within the Ingenstrem Depression and Western Cones provides further evidence of a parental high Mg# andesite magma within the arc. Through mass-balance modeling Yogodzinski et al. (2015) suggests that ~15–50% of LREE and Hf within Aleutian arc magmas are derived from an eclogite melt component. In the eastern Aleutians, this component is hypothesized to be obfuscated by a hotter mantle wedge that produces a larger melt fraction of basalt as well as increased sediment flux. The implication being that there may be a role for both an eclogite slab melt component (Brophy and Marsh, 1986) and a peridotite partial melt component (Kay et al., 1982), which produces the diversity of arc rock compositions within the Aleutians.

Recent interpretations suggest that forearc subduction erosion may produce high Mg# andesites in the central Aleutians during periods of reduced magmatic activity as the volcanic front migrates northwards (Jicha and Kay, 2018; Kay et al., 2019). Evidence stems from both geochemical constraints (i.e. Jicha and Kay, 2018) and the fact that thermal models of central Aleutian slab are moderate to cool in temperatures relative to other arcs worldwide (Syracuse and Abers, 2006). However, given the lack of sediment input within the western Aleutians as well as elevated slab temperatures due to the unique tectonic regime in the region, the MORB-

eclogite component suggested by Yogodzinski et al. (2017) is still plausible in the western Aleutians (Jicha and Kay, 2018). Based on an evaluation of sediment and fluid transport rates and melting processes George et al. (2003) suggests that partial melts from the subducted slab are relegated mainly to the western Aleutians wherein the Pacific plate is torn (Yogodzinski et al., 2001).

The Tholeiitic and Calc-Alkaline Series

Igneous rocks are classified into distinct categories based on where they reside within the compositional spectrum. One such categorization scheme is that of distinguishing between alkaline and sub-alkaline rocks which was initially proposed by Iddings (1892). A further subdivision of the sub-alkaline series includes rocks that are considered to be tholeiitic or calc-alkaline. Both terms, particularly calc-alkaline has been used for over a century to describe a plethora of geochemical constraints on igneous rocks (Arculus, 2003; Zimmer et al., 2010). Regardless of these inconsistencies in use, the terms are pervasive when describing arc magmas and their associated differentiation trends. Arbitrary techniques for classifying the two series include the AFM (alkali-iron-magnesium) diagram of Irvine and Baragar (1971), the FeO*/MgO vs. SiO_2 discrimination diagram of Miyashiro (1974), and more recently, the tholeiitic index of Zimmer et al. (2010).

This study will classify all samples based on bulk geochemical composition using the TAS (total alkali-silica) diagram of Le Maitre et al. (2002) and the sub-alkaline discrimination diagram of Miyashiro (1974). The reasoning for this is: 1) modal mineralogy of all 478 samples referenced in this study are not available, 2) samples for select volcanoes in the region (e.g. Kiska) remain sparse and do not all conform to the geochemical requirements for classification utilizing the methods in Zimmer et al. (2010). One caveat with regard to evolved rocks from

Gareloi is that they have been characterized as “high-K tholeiites” (Coombs et al., 2012). However, besides the aforementioned calc-alkaline samples (Fig. 2), rocks with >53.5 wt. % SiO_2 are classified as being part of the alkaline magmatic series (Fig. 9; Irvine and Baragar, 1971). Therefore, they would be precluded from being categorized as tholeiites. However, the primary suite of rocks from Gareloi is inferred to be comagmatic and hypothesized to be related primarily through fractional crystallization of a basaltic, tholeiitic melt. Additionally within the arc, tholeiitic andesites have been noted for having elevated K_2O relative to calc-alkaline andesites at the same SiO_2 content (Kay and Kay, 1994). Therefore within this study, the rocks from Gareloi will be referred to as tholeiites but their anomalous geochemical signature will be highlighted throughout the remaining chapters. With this understanding, a brief outline of the characteristics of tholeiitic and calc-alkaline magmatism within the Aleutian subduction zone will be addressed.

Subduction zones are the primary tectonic boundary that contains both tholeiitic and calc-alkaline magmas (Kay and Kay, 1985; Grove et al., 2003). Fundamental to the discrimination of both series is Fe content. The tholeiitic series is defined by Fe enrichment during differentiation, whereas the calc-alkaline series is characterized by Fe depletion (Zimmer et al., 2010). Models have depended on the calc-alkaline and tholeiitic series originating from the same parental magma (Kay et al., 1982, 2019; Brophy et al., 1999). However, other models have proposed that both series originate from independent parental sources (Miller et al., 1992; Cai et al., 2015). Recent interpretations suggest that the two geochemical trends are influenced by the along-strike variance of slope, angle, and rate of subduction along the Aleutian volcanic arc (Kelemen et al., 2003a). Irrespective of the many hypotheses surrounding the origin and evolution of both series, some common characteristics may be outlined.

The tholeiitic series is more prevalent in the central/eastern portion of the arc. Tholeiitic volcanoes are larger and have produced more voluminous eruptions than calc-alkaline volcanoes (Fournelle et al., 1994). Tholeiitic magmas undergo shallow, isobaric fractional crystallization at low pressures and high temperatures (Bacon et al., 2007). At a given SiO_2, tholeiitic rocks have higher FeO, TiO_2, and K_2O and lower MgO, CaO, and Al_2O_3 relative to calc-alkaline rocks. Tholeiitic REE (rare earth element) patterns are generally parallel with La/Yb <4. They typically have larger Eu anomalies and higher overall REE concentrations. Evolved tholeiitic basalts are commonly porphyritic while andesites and dacites are microphyric to aphyric (Kay and Kay, 1994). Common phenocryst and groundmass phases include olivine, clinopyroxene, and plagioclase with titanomagnetite relegated to the groundmass. Oxygen fugacity (fO_2) and H_2O content are typically lower than calc-alkaline magmas (Sisson et al., 2005). fO_2 has been shown to be closer to the quartz-fayalite-magnetite (QFM) buffer than nickel-nickel oxide (Ni-NiO) (Rader and Larsen, 2013). H_2O content is typically <2 wt.% (Zimmer et al., 2010) resulting in amphibole not being a common mineral phase (Larsen, 2016).

The calc-alkaline series is more common in the western portion of the arc. Calc-alkaline magmas have a protracted ascent through the crust and undergo polybaric differentiation at higher pressures and lower temperatures (Singer and Myers, 1990). Consequently, exposed plutonic rocks are predominately calc-alkaline (Cai et al., 2015). MgO content is higher relative to tholeiitic rocks at a given SiO_2 due to a greater abundance of mafic phases within calc-alkaline rocks (Kay and Kay, 1994). Higher CaO and Al_2O_3 is associated with the suppression of plagioclase and the potential accumulation of anorthitic plagioclase during magma mixing. Calc-alkaline REE patterns are generally steeper with La/Yb >6. Eu anomalies are less pronounced and REE concentrations are typically lower. Calc-alkaline rocks are commonly crystal rich (30-

50 vol %) and often andesitic (Larsen et al., 2010). Possible phenocryst phases include, olivine, clinopyroxene, orthopyroxene, amphibole, plagioclase, and magnetite. Both plagioclase and clinopyroxene are commonly complexly zoned and have disequilibrium textures (Kay and Kay, 1985). Relative to tholeiitic magmas, calc-alkaline magmas typically have higher fO_2, such as Augustine and Buldir magmas, which are inferred to be close to the rhenium-rhenium oxide (Re-ReO_2) buffer (Larsen et al., 2010; Waters et al., 2021). H_2O content is typically >2 wt. % (Zimmer et al., 2010). Elevated H_2O content is thought to diminish Fe enrichment by suppressing plagioclase fractionation while enhancing magnetite and amphibole fractionation (Zimmer et al., 2010). In turn, amphibole is commonly a defining mineral phase in calc-alkaline rocks with >54 wt. % SiO_2 (Kay et al., 1982).

CHAPTER 4

METHODS

Sample Descriptions

Rocks from Gareloi and Kiska volcanoes were collected by a research team consisting of Dr. E. Cottrell, Smithsonian Institution; Dr. M. Coombs, USGS; Dr. Pistone, postdoc employed at the Smithsonian Institution; Katherine Sheppard, University of Santa Barbara; and Elizabeth Grant, University of California, Davis during the NSF-sponsored GeoPRISMS 2015 research cruise. A sequence of rocks was collected by Dr. Pistone from Gareloi proximal to the GANO seismic station (Fig. 10). Samples G-01 and G-02 are scoria and sample G-03 consists of two lithic fragments (Fig. 11). Samples G-01, G-02, and G-03 are all inferred to have been erupted between 2003 when the GANO seismic station was installed, and 2015 when the NSF-sponsored GeoPRISMS field mission was conducted. Pistone (UGA) and Lyons (USGS) found one of the solar panels of GANO seismic station damaged, most likely due to the landing of ejected pyroclasts from Gareloi volcano. The collected samples have been interpreted by Dr. Pistone to be from the pyroclastic eruption that damaged the solar panels.

Samples G-01, G-02, and G-03 were constructed as one inch epoxy rounds for scanning electron microscopy (SEM) and electron microprobe analysis (EPMA; Fig. 11). Sample G-05 was collected by Dr. Pistone and had previously been constructed into a thin section for EPMA analysis. The sample came from a Holocene shoshonitic lava flow southeast of south peak (Coombs et al., 2012). Seven Kiska samples collected during the third leg of the GEOPRISMS 2015 research cruise were loaned from the NSF-funded Marine Geological Samples Laboratory

of the Graduate School of Oceanography of the University of Rhode Island. Samples 15KKMP007-01 (lava flow) was collected on the northwest corner of the central vent (Fig. 10). Sample 15KKMP006-01 (spatter) was collected ~20 meters east of the central vent. Samples 15KKMP005-04, 15KKMP005-03, 15KKMP005-02, and 15KKMP005-1A were collected in a stratigraphic sequence from top to bottom respectively from a spatter rampart deposit (Rader et al., 2018) ~45 meters east of the main crater rim of Kiska volcano. Sample 15KKKS001-1 is a hyaloclastite collected on a high ridge south of Kiska harbor on the east side of the lagoon (Fig. 10).

Petrography and Point Counting

Six Kiska samples and four Gareloi samples were sent to Quality Thin Sections (Tuscon, AZ) for thin section preparation. Kiska Sample 15KKMP007-01 was not constructed as a thin section because there was only enough sample collected to be sent for bulk major and trace element analysis. Due to the high porosity of the Gareloi samples, the four thin sections did not capture the mineralogical and textural characteristics necessary for further analysis. Instead 1-inch epoxy rounds were constructed for analysis using EPMA and SEM (Fig. 11). Petrographic analyses of the thin sections were conducted using a Nikon Eclipse LV100N POL petrographic microscope. Observations included textural analysis, mineral phase recognition, and whether alteration was present and would affect geochemical analyses. Modal abundances of major mineral phases were calculated using point counting of each thin section by constructing a mosaic of photomicrographs encompassing the entirety of each sample (Fig. 13; Table 1). Vesicles were included in point counting analysis with values reported prior to normalization. Point counting was conducted by use of a randomized grid with 1000 points for each thin section using the JMicroVision software package.

SEM

Textural and chemical analysis of the three Gareloi 1-inch epoxy rounds as well as the six Kiska thin sections were conducted using scanning electron microscopy (SEM) at The University of Georgia (UGA). A Thermo Fisher Scientific (FEI) Teneo field emission scanning electron microscope (FESEM) was used to acquire backscattered electron (BSE) images aimed to capture the textural characteristics of samples as well as a reference for mineral transects. Energy dispersive X-ray spectroscopy (EDS) was used to semi-quantitatively analyze glass, microlites, microphenocrysts, and phenocryst compositions. Multi-point transects of mineral phases were conducted to determine zoning patterns and constrain crystallization conditions. A 10 kV acceleration voltage and 0.8 nA beam current was used for all Kiska analyses. A 10 kV acceleration voltage and beam current of 1.6 and 6.4 nA were used for all Gareloi samples.

EPMA

Electron probe micro-analyzer (EPMA) analysis was conducted at the University of Geneva using a JEOL JSM7001F Scanning Electron Microscope for Kiska sample 15KKMP006-01. Quantitative analyses were conducted using internal standards 210804-fsp, 210804-her-ilm, and 210804-ol-px from the University of Geneva. An accelerating voltage of 15 kV was used for all analyses. A beam current of 1.5 nA was used for plagioclase analyses and a 2 nA beam current was used for orthopyroxene, clinopyroxene, and oxides. Gareloi samples G-01, G-02, G-03, G-05 and Kiska samples 15KKMP005-02 and 15KKMP006-01 were analyzed at the University of Lausanne using a JEOL JXA-8530F HyperProbe. An accelerating voltage of 15 kV and beam current of 5 nA were used for all analyses. A 10 μm beam spot diameter was used for glass, 5 μm for plagioclase, and a 1 μm was used for clinopyroxene, orthopyroxene, olivine, and oxides. In both EPMA analytical sessions, the counting time on the peak and

background positions was 30 and 15 s for Al, Ti, Ca, Mg, and Mn and 10 and 5 s for Si, Fe, Na, K, and P, respectively. Natural and synthetic standards were used and data were ZAF-corrected (Armstrong, 1988), including glass standards of hydrous basalt (5.7 wt.% H_2O; Müntener et al., 2001) and dacite composition (4.2 wt.% H_2O; Pistone et al., 2016). Representative mineral compositions from each sample analyzed are provided in Tables 2 and 3.

Melt-mineral Equilibria, Thermobarometry, and Hygrometry

All melt-mineral equilibria, geobarometry, geothermometry, and hygrometry calculations were conducted using the iterative algorithm implemented in the Python3 tool Thermobar (v.0.18, Wieser et al., 2021). Melt-mineral equilibria testing was conducted on both Gareloi and Kiska samples. All Gareloi data are from EPMA analysis. The bulk of Kiska data are from EPMA data; however glass compositions were not captured for Kiska samples using EPMA due to extensive crystallization of the residual glass that prevented the use of a defocused beam (10 mm diameter). Therefore, an average SEM glass composition from thirty-one point analyses from samples 15KKMP005-1A, 15KKMP005-02, 15KKMP005-03, 15KKMP005-04, 15KKMP006-01 was used (Table 5). Additionally, one phenocryst of olivine was captured exclusively with SEM and therefore was included. Two average glass compositions were derived from Gareloi samples (Table 5). An average composition from eighteen point analyses of G-01 glass was used to test for equilibrium with phenocrysts from G-01, G-02, G-03, and G-05. An average composition derived from sixty-seven point analyses of G-05 glass was also tested for G-05 only.

Olivine-liquid equilibrium testing was conducting using the Fe-Mg exchange coefficient [$K_D(Fe\text{-}Mg)^{ol\text{-}liq} = [(X_{Fe}^{ol}X_{Mg}^{liq})/(X_{Mg}^{ol}X_{Fe}^{liq})]$] of 0.30 ± 0.03 after Roeder and Emslie (1970). A $K_D(Fe\text{-}Mg)^{cpx\text{-}liq}$ of 0.28±0.08 was used for clinopyroxenes and a K_D $(Fe\text{-}Mg)^{opx\text{-}liq}$ of 0.29±0.07

was used for orthopyroxenes after Putirka (2008). Plagioclase-liquid equilibrium was tested using an An-Ab exchange coefficient [$K_D(An\text{-}Ab)^{pl\text{-}liq} = [(X_{Ab}^{pl} X_{AlO_{1.5}}^{liq} X_{CaO}^{liq})/(X_{An}^{pl} X_{NaO_{0.5}}^{liq} X_{SiO_2}^{liq})]$] of 0.1±0.05 for temperatures less than 1050 °C and $K_D(Ab\text{-}An)^{pl\text{-}liq}$ of 0.28±0.11 for temperatures greater than 1050 °C after Putirka (2008).

Clinopyroxene-liquid thermobaromatery of Gareloi and Kiska samples was conducted by iterating equation 30 for pressure and equation 33 for temperature from the model of Putirka (2008). Orthopyroxene-liquid thermobarometry of Kiska samples was conducted by iterating equation 29b from the model of Putirka (2008) for pressure and the geothermometer of Beattie (1993). Olivine-liquid thermometry of Gareloi and Kiska samples was conducted using equation 22 of Putirka (2008), which requires an estimated value for pressure. Based on the best fit MELTS modeling of upper crustal fractional crystallization, 1 kbar was used for both Gareloi and Kiska samples.

Plagioclase-liquid hygrometry was conducted for both Gareloi and Kiska samples using the hygrometer of Waters and Lange (2015), which requires a preliminary estimation of pressure and temperature. In the case of both Gareloi and Kiska, MELTS modeling suggested a pressure of 1 kbar for a best fit model of upper crustal fractional crystallization. A temperature of 980 °C was used for Gareloi samples based upon matching between MELTS and sample average An mol % content (An 68). A temperature of 964 °C was used for Kiska samples based upon matching between MELTS and sample average An mol % content (An 64).

Bulk Major Element and Trace Element Analysis

Seven Kiska samples and one Gareloi sample (G-04) were cleaned using a DI-water sonication bath and dried prior to being sent for bulk major and trace element chemical analysis at the Washington State University Geoanalytical Laboratory (Fig. 12; Table 4). Gareloi sample

G-04 is an artificial amalgamation of fall-out pyroclasts collected at Gano Seismic Station (Fig. 10; Fig. 12H). Artificial mixing was conducted in order to have the requisite 3.5 grams of sample for XRF and ICP-MS analysis. Bulk major element chemistry was conducted using a ThermoARL Advant'XP+ sequential X-ray fluorescence spectrometer. Analytical totals and loss on ignition (LOI) are reported in Table 4. Bulk trace element analysis was conducted using an Agilent 7700 inductively coupled plasma mass spectrometer. Sample preparation, analytical procedure, precision, and accuracy are listed at https://environment.wsu.edu/facilities/geoanalytical-lab/technical-notes/. Trace element totals are reported in Table 4.

MELTS Modeling

Fractional crystallization modeling was applied using Rhyolite-MELTS (v. 1.0.2; Gualda et al., 2012; Ghiorso and Gualda, 2015) to determine whether: 1) bulk rock samples from Gareloi and Kiska can approximate liquid compositions, 2) differentiation of the magmas feeding both Gareloi and Kiska can be explained primarily by fractional crystallization. Modeling was relegated exclusively to the upper crust because phase equilibria involving hornblende and biotite are not modeled well by the MELTS package (e.g. Nandedkar et al., 2014). Parental magmatic starting compositions were selected based upon Mg#, rock type (i.e. not a xenolith or country rock), and overall fit with samples from each respective volcano when plotted on Harker diagrams.

Principal Component Analysis

Principal component analysis (PCA) based on a correlation matrix was used to evaluate the major element compositional variation seen for each active volcano within the distal Aleutians (Le Maitre, 1982). This approach reduced the dimensionality of the data to two

principal components allowing for a more efficient analysis than using traditional Harker diagrams. Two outlier samples were culled from the data. Sample 03GRBB22 from Gareloi is a gabbroic lithic bomb implying that it is not directly related to the same magmatic parent as the other samples. Sample Snyder_1959_1 from Little Sitkin is described as a "holocrystalline basalt with 15 mm diameter augite crystals" (Snyder, 1959). The sample has anomalously high MgO (11.02 wt. %) for a given SiO_2 relative to the rest of the suite from the volcano, that suggests it is likely a cumulate rock. Therefore, neither rock should be used to infer the magmatic composition from which it formed.

Given the lognormal distribution of major elements, a base-10 log transformation was conducted to account for skewness. A scree plot of eigenvalues was used to visualize the percentage of explained variation for each principal component. All principal components whose explained variation accounted for less than one principal component were then discarded. A table of loadings was constructed in order to determine the extent each variable contributed to a specified principal component. Loadings in bold emphasize any variable which contributes more than one variable's worth of information and indicates a strong positive or negative correlation with the principal component. A distance biplot with scores color coded by volcano and loadings represented by vectors was used to interpret what each principal component represents. Further corroborating these interpretations, two bivariate plots designating the shift from basalt to rhyolite and from tholeiitic to calc-alkaline rocks were constructed.

CHAPTER 5

RESULTS

Petrography

All Kiska samples share similar modal mineralogy and textures besides 15KKKS001-1, which will be addressed separately below. Kiska samples are porphyritic with phenocrysts having a seriate texture. Vesicularity ranges from 15.5 vol % in sample 15KKMP500-52 to 46 vol % in sample 15KKMP005-04 (Table 1). The mineral phases present in descending order of abundance are plagioclase, orthopyroxene, clinopyroxene, and oxides with the exception of 15KKMP006-01, which contains more clinopyroxene than orthopyroxene (Table 1). Sample 15KKMP006-01 has a single olivine with a prominent reaction rim of orthopyroxene, which was observable exclusively during SEM analysis. All four mineral phases appear as cumulophyric clots and as isolated phenocrysts (Fig. 14A–D). Clot populations include clinopyroxene + oxides ± orthopyroxene ± plagioclase. Plagioclase is the preeminent phenocryst phase present and occurs as phenocrysts (>200 μm), microphenocrysts (50–200 μm), and microlites (<50 μm). Phenocrysts are euhedral, inequigranular, and are up to ~3400 μm in size (Fig. 14B). Pervasive disequilibrium textures including embayments, resorption, and sieved phenocryst cores are present. Oscillatory zoning is visible in approximately half of the larger phenocrysts. Inclusions of oxides and clinopyroxene are present both within cores and grain boundaries of select phenocrysts (Fig. 14A). Microlites are pilotaxitic and commonly have a swallow-tailed texture.

Both clinopyroxene and orthopyroxene are present as phenocrysts, microphenocrysts, and microlites. However, microlites are cryptocrystalline and required SEM analyses for

confirmation. Phenocrysts are subhedral-euhedral and inequigranular (Fig. 14C). They span ~200–3500 μm in length. Simple twinning is common. Chemical zoning is indicated by interference color variation and occurs both on rims and as sector zoning within phenocryst cores (Fig. 14A). Rims are frequently embayed. Inclusions of oxides both within phenocryst cores and rims are pervasive. Oxides are present as phenocrysts, microphenocrysts, and microlites. They occur both as inclusions (core and rims), as lone phenocrysts, and as microlites within the groundmass (Fig. 14A). The groundmass of Kiska samples ranges in modal abundance from 27 to 53 vol %. It is tanned and microcrystalline with only plagioclase and oxide microlites being discernible through petrographic observations.

Sample 15KKKS0-01 is a hyaloclastite collected on a high ridge south of Kiska harbor on the east side of the lagoon (Fig. 10). The minerals present in order of decreasing abundance are plagioclase, clinopyroxene, and oxides (Table 1). No vesicles are present within the sample. Palagonite alteration is featured prominently overprinting the groundmass, phenocrysts, and filling sieved pockets of plagioclase phenocrysts (Fig. 14E). Plagioclase occurs as sub-trachytic phenocrysts, microphenocrysts, and microlites. Phenocrysts are euhedral and up to ~1750 μm in length (Fig. 14F). Disequilibrium textures including resorption, embayments, and sieved cores occur on nearly all grains. Phenocrysts are often glomerocrystic, but isolated phenocrysts are also present. Irregular sector zoning and concentric oscillatory zoning are common. Clinopyroxene occurs predominantly as microphenocrysts and microlites with the exception being one cumulophyric clot of clinopyroxene + oxides (Fig. 14E). Phenocrysts are anhedral and up to ~320 μm in length, with select crystals having zoned rims. Oxides occur predominantly as microphenocrysts and microlites. The majority of oxides are microlites present within the groundmass. The groundmass consists of plagioclase, palagonite, clinopyroxene, and oxides.

Sample G-05 is porphyritic and seriate in texture. The sample contains 4 vol % vesicles (Table 1). The minerals present in order of decreasing abundance are plagioclase, clinopyroxene, olivine, and oxides. All four mineral phases appear as cumulophyric clots and as isolated phenocrysts, microphenocrysts, or microlites (Fig. 14G). Clot populations include olivine + oxides ± plagioclase ± clinopyroxene. Plagioclase is the dominant mineral phase and occurs as phenocrysts, microphenocryst, and microlites (Fig. 14H). Phenocrysts are up to ~3440 μm in length. They are euhedral, but have disequilibrium textures including resorption, heavily sieved cores, and embayed rims. Both clinopyroxene and olivine appear as inclusions within select phenocrysts. Oscillatory and sector zoning are present on select phenocrysts and microphenocrysts. Clinopyroxenes are euhedral and up to 2100 μm in length. Nearly all clinopyroxenes occur within cumulophyric clots of clinopyroxene + oxides ± olivine ± plagioclase (Fig. 14G). Inclusions of oxides are present within nearly all phenocrysts and microphenocrysts. Plagioclase and olivine inclusions are present in select larger phenocrysts. Twinning is common. Olivine phenocrysts are subhedral–euhedral and up to ~500 μm in length. The majority occur within cumulophyric clots, however isolated phenocrysts and microphenocrysts are present.

Minerals

Representative pyroxene compositions from both Kiska and Gareloi samples are listed in Table 2. All analyses are plotted on the Wo-En-Fs (wollastonite-enstatite-ferrosilite) pyroxene quadrilateral (Fig. 15A). Clinopyroxene from Kiska is further classified as augite. Augite from Kiska with all Fe reported as FeO ranges from ~Wo 40 En 44 Fs 16 to ~Wo 44 En 42 Fs 14. Kiska orthopyroxene is predominantly enstatite and ranges from ~Wo 0.02 En 0.59 Fs 0.39 to ~Wo 0.06 En 0.7 Fs 0.25 (Fig. 15A). However, two of thirty-six orthopyroxene compositions are

classified as pigeonite (Wo 6 En 67 Fs 27 and Wo 11 En 49 Fs 40). Gareloi samples lack orthopyroxene but have both augite and diopside (Fig. 15A). Seventy-one clinopyroxene compositions are augite whereas fifty-three are diopside. Augite from Gareloi ranges from ~Wo 31 En 49 Fs 20 to ~Wo 44 En 43 Fs 13. Gareloi diopside ranges from ~Wo 45 En 43 Fs 13 to ~Wo 46 En 41 Fs 13. Clinopyroxenes from both Gareloi and Kiska samples are normally zoned (Fig. 17 A–B, G). Mg# in Gareloi clinopyroxenes range from Mg# 67-77. Mg# in Kiska clinopyroxenes range from Mg # 71–77. Orthopyroxene from Kiska commonly has reversed zoning (Fig. 18B) and Mg# ranges from 67–74 with phenocryst cores being out of equilibrium with average glass compositions (Fig. 21 C–D).

Representative olivine compositions from both Kiska and Gareloi samples are listed in Table 2. A singular phenocryst of olivine is present within Kiska sample 15KKMP006-01 with a reaction rim of orthopyroxene (Fig. 18A). Forsterite (Fo) content ranges from 70 to 78 mol % (Fig. 15B). In Gareloi samples, olivine spans a broad compositional range (60–76 Fo mol %; Fig. 15B). Relative to Gareloi olivine, the core of the Kiska phenocryst in sample 15KKMP006-01 has elevated Fo content (76–78 mol %; Fig. 15B).

Representative plagioclase compositions from both Kiska and Gareloi samples are listed in Table 2. Additionally, anorthite (An) contents of plagioclase phenocrysts from both Gareloi and Kiska samples are plotted in the Or-Ab-An (orthoclase-albite-anorthite) ternary diagram seen in Fig. 15C. Kiska plagioclase is further classified as labradorite and bytownite (53–87 mol % An). Whereas Gareloi plagioclase phenocrysts are andesine, labradorite, and bytownite (48–82 mol % An). Gareloi feldspar is more potassic than Kiska feldspar with Gareloi Or ranging from 1–5 mol % and Kiska Or ranging from 0–2 mol % (Fig. 15C).

Both Gareloi and Kiska plagioclase phenocrysts are variably zoned. A distinguishing feature of select plagioclases from both volcanoes is the common occurrence of oscillating An content before reaching a homogenous rim composition. For instance, a representative Kiska phenocryst oscillates from 57–75 mol % An before reaching a rim composition of 60 mol % An. (Fig. 16A). A representative Gareloi phenocryst oscillates from 71–81 mol % An before reaching a homogenous rim composition of 59 mol % An (Fig. 16B). Sector zoning also occurs in select Gareloi plagioclase phenocrysts often with over 20 mol % An variation (Fig. 17C). Normal zoning is found predominately in Gareloi microlites with cores having ~56 mol % An and rims having ~42 mol % An (Fig. 17D). Kiska plagioclase phenocrysts also contain variable zonation patterns wherein An may increase from core to rim (e.g. 58–76 mol % An; Fig. 17E–F) or decrease from core to rim (e.g. 36–60 mol % An; Fig. 17H). Representative oxides from both Gareloi and Kiska are listed in Table 2. Oxides are further designated as titanomagnetite for both Gareloi and Kiska.

Melt-Mineral Equilibria

Due to extensive crystallization of the residual glass in both Gareloi and Kiska samples, the use of a defocused beam (10 mm diameter) during EPMA analysis was limited. 18 glass compositions from G-01 were captured and averaged (Table 5) to test for equilibrium with phenocrysts from G-01, G-02, G-03, and G-05. An average composition derived from sixty seven point analyses of G-05 glass (table 5) was also tested for G-05 only. No glass compositions were able to be captured from Kiska samples using EPMA. Therefore an average SEM glass composition from thirty-one point analyses from samples 15KKMP005-1A, 15KKMP005-02, 15KKMP005-03, 15KKMP005-04, 15KKMP006-01 was used to test for equilibrium between mineral and melt pairs for Kiska samples (Table 5).

Olivine-liquid equilibrium testing was conducted using the Fe-Mg exchange coefficient of 0.30 ± 0.03 after (Roeder and Emslie, 1970). G-01, G-02, and G-03 were collected from the same pyroclastic deposit proximal to GANO seismic station (Fig. 10). All olivine compositions analyzed from G-01 are in equilibrium with G-01 glass with Fo content ranging from 70 to72 mol % (Fig. 19A). Five analyses from G-02 have Fo content too high glass (74-80 mol %) to be in equilibrium with G-01 while three analyses are in equilibrium (68-71 Fo mol %; Fig. 19B). All six G-03 olivine compositions are out of equilibrium with G01 glass with Fo content ranging from 60 to 63 mol % (Fig. 19C). G-05 olivine compositions are not in equilibrium with G-05 glass (Fig. 19D), but three samples are in equilibrium with G-01 glass (69–70 Fo mol %; Fig. 19E). All Kiska olivine compositions are from the phenocryst seen in Fig. 18A. Olivine compositions from the core of the phenocryst are not in equilibrium with Kiska glass while the rim of the olivine phenocryst is (70 Fo mol %; Fig. 19F). Geothermometry indicates that this lone equilibrium Kiska composition is inferred to have formed at 933 ℃ (Fig. 19G). In contrast, Gareloi olivines are inferred to have formed between 1077 and 1088 ℃ (Fig. 19G).

Clinopyroxene-liquid and orthopyroxene-liquid equilibrium testing was conducted using a Fe-Mg exchange coefficient of 0.28±0.08 and 0.29±0.07, respectively (Putirka, 2008). Gareloi clinopyroxenes are generally in equilibrium with G-01 glass for samples G-01, G-02, and G-03 (Fig. 20A-C). One exception is a clinopyroxene composition with a Mg# of 60 (Fig. 20C). Clinopyroxene compositions from G-05 are in equilibrium with G-05 glass (Fig. 20D), but not G-01 glass (Fig. 20E). Two clinopyroxene compositions from sample 15KKMP006-01 have too high of a Mg# (77–78, Fig. 20B). While an orthopyroxene composition from both 15KKMP005-02 and 15KKMP006-01 have too low of a Mg# (60 and 55 respectively, Fig. 20C–D). Clinopyroxenes and orthopyroxenes from Kiska are generally in equilibrium with Kiska glass

(Fig. 21A–D). Sample 15KKMP005-02 has one orthopyroxene composition with too low of a Mg# (67) relative to glass (Fig. 21C). While 15KKMP006-01 has three clinopyroxene compositions with too high of a Mg# (73–76) and one orthopyroxene with a Mg# (~53) too low to be in equilibrium with glass (Fig. 21B, D).

Estimated Gareloi clinopyroxene temperatures range from 1045 to 1122 ℃ with an average temperature of 1065 ℃ (Fig. 22A). Estimated pressures range from 0.3 to 8.8 kbar with a median pressure of 1.8 kbar (Fig. 22B). Both temperature and pressure decrease with increasing Mg# (Fig. 23). Estimated Kiska clinopyroxene temperatures range from 968 to 982 ℃ with an average temperature of 975 ℃ (Fig. 22A). Estimated pressures range from 0.3 to 2 kbar with an average of 1.1 kbar (Fig. 22B). In contrast to Gareloi clinopyroxenes, both temperature and pressure remain relatively constant with decreasing Mg# in the Kiska samples. Estimated Kiska orthopyroxenes temperatures range from 1061 to 1107 ℃ with an average temperature of 1083 ℃ (Fig. 23A). Estimated pressures range from 0.84 to 7.5 kbar with an average of 4.0 kbar (Fig. 23B). Two distinct groups of orthopyroxenes are present. Group 1 is relegated to a temperature range of 1087 to 1107 ℃ and a pressure range of 4.6 to 7.6 kbar. These samples have a Mg# >70. Group 2 is relegated to a temperature range of 1061 to 1082 ℃ and a pressure range of 0.84 to 3.9 kbar. These samples have a Mg# <70. One outlier sample seen in both Fig. 22A and Fig. 22B has an anomalously high Mg# of ~73 yet an estimated temperature of 1064 ℃ and pressure of 1.2 kbar.

Plagioclase-liquid equilibrium was tested using an An-Ab exchange coefficient of 0.1±0.05 for temperatures less than 1050 ℃ and 0.28±0.11 for temperatures greater than 1050 ℃ after (Putirka, 2008). Based on plagioclase-liquid hygrometry, water concentrations are elevated in Kiska magmas relative to Gareloi magmas. Water concentrations in Kiska magmas

range from 2.5–3.1 wt. %, whereas water concentrations in Gareloi magmas range from 2.2–2.7 wt. % (Fig. 24). Average water content is 2.8 wt. % for Kiska samples and 2.5 wt. % for Gareloi samples (Fig. 24).

MELTS Fractional Crystallization Models

Gareloi sample 03GRBB41 was chosen as a starting composition for modeling of fractional crystallization. It is described as crystal rich basalt containing plagioclase, clinopyroxene, and olivine (Coombs et al., 2012). Gareloi models spanned from 1 to 3 kbar, QFM–QFM+3, and 0.5–3 wt. % H_2O. Use of water content above 3.5 wt. % caused modeling to fail. Ultimately, the best fit model was at 1 kbar, QFM+2, and 2 wt. % H_2O. The liquidus was crossed at 1128 ℃ when clinopyroxene began to fractionate followed by subsequent fractionation of spinel (1107 °C), plagioclase (1080 °C), olivine (1068 °C), and apatite (918 °C). A common characteristic of all models is that at ≥55 wt.% SiO_2, MELTS generated depleted trends relative to samples for MgO and FeO_t (Fig. 25A–B). This is further corroborated by the lack of correlation between MELTS Mg# and Gareloi sample Mg# (Fig. 25C).

Samples from Gareloi are anomalous with regards to Al_2O_3 wherein basalt and basaltic-andesites both have a wide range of Al_2O_3 content (~17.3–20.6 wt. %) with more evolved samples having a more restricted average of ~18 wt. % (Fig. 26A). This is reflected in the MELTS model wherein plagioclase is initially suppressed (rapidly increasing Al_2O_3) and eventually inflects, as opposed to plagioclase immediately fractionating. Furthermore, the MELTS liquid line of descent (LLD) has CaO and CaO/Al_2O_3 depleting too rapidly to conform with sample compositions, but then corrects at ~55 wt. % SiO_2 (Fig. 25D; Fig. 26B). Na_2O generally conforms to bulk sample compositions, but at >55 wt. % SiO_2, Na_2O concentrations from the MELTS LLD are ~0.1–0.2 wt. % higher than bulk samples (Fig. 26C). The MELTS

LLD has K_2O enrichment with increasing SiO_2 and resides within the high-K field of Gill (1981) just like bulk sample compositions. However, K_2O is depleted relative to sample compositions (Fig. 26D). Models calculated with lower fO_2 (QFM) conformed better to sample compositions with regards to K_2O and Na_2O. However, this was at the expense of skewing all other major element trends. Average glass compositions from G-01 and G-05 are depleted in CaO, Al_2O_3, and Na_2O relative to bulk rock samples and enriched in FeO_t and K_2O. Glass composition conform better with MgO and CaO/Al_2O_3 bulk rock compositions.

MELTS modeling of fractional crystallization of Kiska magmas was initially simulated using more primitive starting sample compositions; however, irrespective of intensive parameters, these models failed to generate coherent trends that align with bulk composition sample data. Sample 15KKMP007-01, a basaltic-andesite (Table 4) was selected because shallow level fractionation of at least clinopyroxene is evident from geobarometry (Fig. 22B). Therefore, the intent was to assess if a two-pyroxene andesite (also present as the anomalous calc-alkaline samples from Gareloi) approximates a liquid and may evolve towards average glass compositions in the shallow crust prior to eruption.

Kiska models spanned from 1 to 4 kbar, QFM to QFM+3, and 0.5 to 3 wt. %. Use of water content above 3.5 wt. % H_2O caused modeling to fail. Ultimately the best fit model was determined to be at 1 kbar, QFM+2, and 3 wt. % H_2O. Spinel was the liquidus phase at 1081 °C followed by orthopyroxene (1063 °C), clinopyroxene (1060 °C), feldspar (1021 °C), and olivine (865 °C). Both MgO and FeO_t have an initial negative correlation with SiO_2 due to the fractionation of spinel, orthopyroxene, and clinopyroxene until plagioclase fractionates at ~58 wt. % SiO_2 (Fig. 25A–B). This drives the MELTS LLD through two pyroxene andesite from Gareloi as well as samples from Semisopochnoi and Little Sitkin. MgO nearly intersects average

Kiska glass while FeO_t from the MELTS LLD is ~4 wt. % as opposed to glass which is ~3 wt. % at ~70 wt. % SiO_2. Mg# fails to reach the average glass Mg# from Kiska samples (Fig. 25C). However, the LLD does maintain a higher Mg# to Gareloi's LLD and nearly intersects one of the calc-alkaline rocks from Gareloi.

CaO and CaO/Al_2O_3 follows a transitional LLD between tholeiitic and calc-alkaline samples from the region before nearly intersecting Kiska glass (Fig. 25D; Fig. 26B) In a similar fashion to Gareloi MELTS modeling, Al_2O_3 is anomalous in that it peaks at ~19 wt. % at ~60 wt. %. SiO_2. Whereas bulk sample compositions do not exceed 18 wt. % Al_2O_3 at ~60 wt. % SiO_2. Plagioclase fractionates at ~59 wt. % SiO_2 and Kiska's LLD bounds evolved distal Aleutian samples with the highest Al_2O_3 concentrations within the region (16.5–18.5 wt. %) before failing to reach Kiska glass (Fig. 26A). At ~70 wt. % SiO_2, the MELTS LLD is too enriched in Na_2O (4.3 wt. %) relative to Kiska glass (4.0 wt. %; Fig. 26C). However, the curvilinear shape of the line does follow a similar trend to samples with lower Na_2O concentrations from Little Sitkin and Ingenstrem Depression. With regards to K_2O, Kiska's LLD follows a medium-K trend with a distinct lack of samples for the region before nearly intersecting Kiska glass (Fig. 26D)

Total Alkali-Silica

Rocks from the distal Aleutians encompass the entire compositional spectrum within the arc and their alkalic components (Na_2O+K_2O) decrease systematically westward (Fig. 27). Rocks from Gareloi and Semisopochnoi have elevated concentrations of Na_2O+K_2O compared to rocks from the rest of the distal Aleutians. Gareloi rocks are more enriched in K_2O relative to Na_2O compared to Semisopochnoi samples, which are more enriched in Na_2O relative to K_2O. Two trends are present for Gareloi samples. The predominant trend contains the most alkali enriched rocks within the arc based on the dataset of Kelemen et al. (2003a). Of the seventy-four

samples from the Gareloi rock dataset, one sample is a potassic trachybasalt, four are mugearites, forty are shoshonites and fourteen are latites (Fig. 27). The second trend consists of less alkalic rocks which consists of an array of four samples that straddle the dividing line between basaltic-andesite and basaltic trachyandesite with more evolved samples plotting in the andesite field (Fig. 27). These seven andesitic samples are the calc-alkaline rocks from Gareloi seen in Fig. 2. From a compositional standpoint, they are closer to rocks from other distal Aleutian calc-alkaline volcanic centers. Tholeiitic Gareloi samples range in K_2O concentrations from 1.56 to 3.81 wt. % and Na_2O ranges from 3.36 to 5.47 wt. % while calc-alkaline samples have K_2O ranging from 1.37 to 1.40 wt. % and Na_2O ranging from 4.31 to 4.44 wt. %.

Alkali enrichment is less pronounced for Semisopochnoi samples relative to Gareloi. However, they are compositionally distinct for the area and have higher alkali concentrations than other volcanic centers within the region. Semisopochnoi samples range in K_2O concentrations from 0.54 to 3.55 wt. % and Na_2O ranges from 2.75 to 5.18 wt. %. Of the eighty-eight available samples, three are classified as mugearites, three are latites, seventeen are benmoreites, and eighteen are trachytes. Rocks from the remaining volcanic centers haver lower alkali concentrations and span the compositional spectrum from basalt to dacite. Western Cone samples and two samples from Little Sitkin are further categorized as rhyodacites (67–70 wt. % SiO_2; Fig. 27).

Principal component analysis

Principal component analysis (PCA) was undertaken in order to reduce the dimensionality of the bulk major element dataset queried from the Alaskan Volcano Observatory for the distal Aleutians. In turn, PCA yielded two primary principal components which explain the majority of variation in the data. PC1 accounts for 58 % of the explained variation in the

dataset while PC2 accounts for 28 % (Fig. 28A). In total, PC1 and PC2 account for 85 % of the explained variation in the dataset. With the exception of P_2O_5, all major elements have clear positive or negative loadings for PC1 indicating their involvement in PC1 (Fig. 28B). SiO_2 and Na_2O have strong positive correlations with PC1. Conversely, MgO, FeO_t, CaO have strong negative correlations with PC1. With the exception of SiO_2, all major elements have clear positive or negative loadings on PC2 indicating their involvement in PC2. K_2O, P_2O_5, TiO_2, and Na_2O have strong positive correlations for PC2 while MgO has a strong negative correlation (Fig. 28B).

When scores are sorted by volcano, Gareloi and Semisopochnoi samples are positively correlated with both PCA 1 and PCA 2 (Fig. 29A). The exception being six samples from Gareloi which are classified as calc-alkaline (Fig. 2). Little Sitkin samples generally parallel PCA 1. Limited samples are available for Kiska, but the majority of samples parallel PCA 1. The exception being two basaltic samples in the lower left of the plot and the most evolved sample of the suite plotting closer to Semisopochnoi samples. Buldir samples are scattered within the lower half of the plot, with intermediate compositions having the greatest heterogeneity. Ingenstrem Depression samples cluster into two predominant fields with a gap of limited intermediate samples in between which show heterogeneity relative to the rest of the suite. The Western Cones have a restricted SiO_2 composition (68.99–70.12 wt. % SiO_2) and aggregate on the positive end of PCA 1.

When samples are sorted by SiO_2 wt. %, a positive correlation is seen between increasing SiO_2 wt.% content and PCA 1 (Fig. 29A). Basalts (<53 wt. % SiO_2) plot towards the left and rhyolites (>70 wt. % SiO_2) plot to the right. When samples are sorted as being either tholeiitic or

calc-alkaline, a correlation is seen between magmatic series and PCA 2 (Fig. 29B). This trend is particularly evident for samples with intermediate to high SiO_2 wt. % (i.e. andesite–rhyolite).

Rare Earth Elements

At 53 SiO_2 wt. %, all volcanic centers besides Western Cones aggregate into a cluster from ~1.7–2.2 Dy/Yb (Fig. 30A). However, with increasing SiO_2, two divergent paths are apparent. The volcanic centers that reside on the arc ridge (i.e. Gareloi–Buldir) have a negative correlation between Dy/Yb and SiO_2, whereas a positive correlation is present between Dy/Yb and SiO_2 for Ingenstrem Depression samples. Western Cones data are again anomalous and cover a broad range of Dy/Yb (~2.3–3.0). However, they do fit in a semi-coherent trend with higher SiO_2 Ingenstrem Depression samples. Dy/Dy* increases with increasing Dy/Yb for all volcanic centers besides the Western Cones (Fig. 30B). LREE depleted samples have higher Dy/Dy* at a lower Dy/Yb compared to LREE enriched samples. At Dy/Yb >2.2, select Gareloi samples as well as Ingenstrem Depression samples level off in Dy/Dy*, which distinguishes them from all other volcanic centers withing the distal Aleutians.

The heterogeneity of along strike relative concentrations and shapes of REEs is apparent for Gareloi, Kiska, and the Western Cones (Fig. 31A–C). Gareloi is the most LREE (La–Nd) enriched suite relative to chondrites with a steep downward trend from LREE–MREE (Sm–Ho) and a slight curve up shape from MREE–HREE (Er–Lu) (Fig. 31A). Relative concentrations of the seven Gareloi calc-alkaline samples are depleted compared to tholeiitic samples but have similar overall shapes. Most tholeiites have a negative Eu anomaly with the steepest negative Eu anomalies occurring in the most relatively enriched samples. With decreasing REE concentrations the relative steepness of the negative Eu anomaly decreases with one tholeiitic sample having a positive Eu anomaly. Calc-alkaline samples distinctly lack an Eu anomaly.

Kiska samples have an overall less fractionated REE pattern and are relatively depleted in REE compared to most Gareloi samples (Fig. 31B). There is an overall downward shape from LREE–MREE and a slight concave up shape from MREE–HREE. LREE relative concentrations are variable with select samples having distinct negative Ce and Nd anomalies. A negative Eu anomaly is present for all samples but is not as steep as Gareloi samples. Western Cones samples have comparable LREE relative enrichment to Kiska samples (Fig. 31B–C). However, Western Cones samples have highly fractionated REE patterns with HREE being heavily depleted.

La/Yb increases drastically for Ingenstrem Depression and Western Cones samples with increasing SiO_2 (Figs. 32–33A). La/Yb of basalts and basaltic-andesites range from 3.8 to 9.8. For andesite and more silica-rich compositions, La/Yb spans a range of 4.6 to 33 with the majority of Western Cones samples being the most fractionated within the distal Aleutians. While samples are sparse, Buldir lavas tend to consistently parallel a subset of Ingenstrem Depression sample compositions (Fig. 32B). Buldir basaltic-andesites have similar La/Yb concentrations (~5) to adjacent volcanic centers. However, one Buldir andesite has a La/Yb value of 7.5 and a dacite has a value of 9. Gareloi samples have elevated La/Yb (~6–9) relative to other distal Aleutian volcanoes which reside on the arc ridge (Fig. 4A). Initially La/Yb increases rapidly with increasing SiO_2, with basaltic-andesites characterized by La/Yb of up to 9.1. However at ≥55 SiO_2 wt. %, La/Yb levels off at ~8 (Fig. 33B). Semisopochnoi, Little Sitkin, and Kiska samples have overall lower La/Yb than Gareloi (~4 La/Yb) and generally flat trends with increasing SiO_2 (Fig. 33B).

Basalt REE patterns of Gareloi and Semisopochnoi are generally uniform in shape with Gareloi being slightly more fractionated (Fig. 32A). Both have a limited, but detectable negative Eu anomaly. Little Sitkin has an overall flatter shape with less overall LREE concentrations. No

basalt samples from Kiska are currently available. Buldir basalt is similar Little Sitkin that REE are sub-parallel and generally flat with a slight downward trend from LREE to MREE and a slight concave up shape from MREE–HREE. However Buldir HREE has similar relative abundance of HREE to that of Ingenstrem Depression. Ingenstrem Depression basalt is the most fractionated within the region as indicated by LREE/HREE. Similar to Buldir and Little Sitkin, Ingenstrem Depression basalt lacks an Eu anomaly.

All andesites are more fractionated than basalts and have a greater relative concentration of LREE with the exception of Ingenstrem Depression (Fig. 32B). A negative Eu anomaly is present from Gareloi–Kiska, but it generally decreases in steepness westward. Buldir and Ingenstrem Depression andesites lack an Eu anomaly. Buldir andesite parallels Ingenstrem Depression andesite at lower overall REE concentrations. Trace element data for Kiska is only available for andesites. Kiska andesite tends to parallel Little Sitkin andesite. However, Kiska andesite has a more prominent concave up shape from MREE–HREE. Dacitic samples from the region are limited (Fig. 32C). However, distinct REE patterns and concentrations are present. Dacites have the most fractionated REE patterns. Semisopochnoi is the only dacite with a pronounced negative Eu anomaly. Little Sitkin has overall depleted REE concentrations relative to Semisopochnoi. Ingenstrem Depression and Western Cones dacites are markedly more fractionated than Semisopochnoi and Little Sitkin dacites.

Mg#

In contrast to Na_2O+K_2O (Fig. 27), Mg# systematically increases westward at a given SiO_2 (Fig. 33D). Basalts (SiO_2 <53 wt.%) from Gareloi and Semisopochnoi have a Mg# of ~41–53 while Buldir and Ingenstrem Depression samples range from a Mg# ~63–70. Gareloi basalts–basaltic-andesites are noted for their relative rapid depletion in Mg# compared to other volcanic

centers. The extent of relative depletion in Mg# with increasing differentiation decreases nearly systematically along strike of the arc from east to west. At SiO_2 of 60 wt. %, Gareloi samples have a Mg# of ~33 while Ingenstrem Depression samples have a Mg# of ~61. Gareloi, Semisopochnoi, Little Sitkin, and Kiska grade from a strong negative correlation between Mg# and SiO_2 to a neutral correlation (i.e. Kiska samples have a flat trend). The exception being samples from Little Sitkin with >65 wt. % SiO_2 that have negative correlation with Mg# as well as three Kiska outlier samples at ~58 wt. % SiO2 with variable Mg# (~40–50). Additionally, one Kiska basaltic sample has a Mg# of ~68. An inflection is present in Buldir and Ingenstrem Depression samples wherein a negative correlation is present until ~60 wt. % SiO_2 and then shifts to a positive correlation. Western Cones samples appear as an end-member composition of Ingenstrem Depression samples based off of the presence of a coherent curvilinear trend connecting the two volcanic provinces. Western Cones samples are rhyodacites yet have the highest values for Mg# within the entirety of the distal Aleutians.

Source Components

Sr/Y is highly variable within the distal Aleutians (Fig. 34A). In general, Sr/Y increases with Mg#. However, this is not the case for Ingenstrem Depression samples with Mg# >62. Gareloi–Buldir samples range in Sr/Y from 5.4–48 while Western Cones samples have Sr/Y up to 296. Th/La decreases systematically westward within the distal Aleutians (Fig. 34B). This trend is coincident with an increase in Mg#. Gareloi samples have up to 0.7 Th/La while Ingenstrem samples are as low as 0.4 Th/La. A compositional gap at Mg# of ~45–60 and Th/La ~0.1–0.3 is present between samples from Gareloi–Kiska and Buldir–Western Cones.

Both Gareloi and Semisopochnoi have an initial positive correlation between Ba and Sr. However for Gareloi samples, at ~800 Ba ppm an inflection is reached, and Sr decreases with

increasing Ba (Fig. 34C). This inflection is correlated with a shift in magmatic composition from basalt–dacite. A similar inflection is seen at ~600 Ba ppm for Semisopochnoi samples. Little Sitkin, Kiska, and Buldir have a much more restricted range of Ba and Sr content (~200–420 ppm and ~100–500 ppm, respectively). Little Sitkin and Kiska samples have an apparent negative correlation between Ba and Sr while Buldir samples have a neutral correlation. However, sample data from all three volcanic centers is limited. Barring one outlier sample, Ingenstrem Depression and Western Cones samples have a restricted Ba range (70–650 ppm) and the highest Sr within the distal Aleutians (380–1850 ppm).

Gareloi samples have a nearly flat trend with respect to U/Th while ranging in Th content from 2.2 to 10.7 ppm (Fig. 34D). Semisopochnoi samples are consistent with the elevated Th content (~2–6 Th ppm) observed for Gareloi samples. However, samples with lower Th content have variable U/Th, which parallels trends from other westward volcanoes. Notably, all Semisopochnoi samples with Th <2 ppm are basalts and basaltic-andesites. Buldir and Western Cones samples are relegated to U/Th values of ~0.30–0.55. In contrast, Kiska samples have elevated U/Th of ~0.6 and parallel the vertical trend of Ingenstrem Depression samples.

CHAPTER 6

DISCUSSION

Petrography

The mineralogy of both Gareloi and Kiska rocks conform to their respective tholeiitic and calc-alkaline differentiation trends. Rocks from both islands contain clinopyroxene and have plagioclase as the most abundant phase; a common feature in Aleutian arc rocks irrespective of magmatic series (Table 1; Kay and Kay, 1985). Phenocryst-rich basalts are common in both series, but tholeiitic andesites and dacites have a tendency of being less porphyritic (Kay et al., 1982). This may in part explain Gareloi sample G-05 being less crystal-rich compared to Kiska samples (Table 1). Within the Aleutians, orthopyroxene is predominately relegated to calc-alkaline rocks (Kay and Kay, 1985). Kiska rocks contain orthopyroxene, whereas Gareloi rocks do not. Orthopyroxene has been noted for being present as a rim on olivine phenocrysts in calc-alkaline basaltic-andesites (Kay and Kay, 1985). In the case of Kiska, this mantling of olivine phenocrysts with orthopyroxene is present (Fig. 18A). This further supports that from a mineralogical perspective, Kiska is a calc-alkaline volcanic center. Olivine is found in both tholeiitic and calc-alkaline basalts, but is found predominantly in calc-alkaline andesites (Kay and Kay, 1985). Sample G-04 is a basaltic-andesite and was collected from the same location as G-01, G-02, and G-03, all of which have minor amounts of olivine (Fig. 19A-C; Table 2). Additionally, samples from the same lava flow as G-05 are basaltic andesites and contain olivine (Coombs et al., 2012). Therefore, the presence of minor olivine in Gareloi basaltic-andesites fits within the mineralogical framework of the tholeiitic series.

Mineral Characteristics

Minerals from both tholeiitic and calc-alkaline rocks within the Aleutians commonly have disequilibrium textures including embayed rims and sieved plagioclase cores (e.g. Nye et al., 2018; Larsen et al., 2020). Kay and Kay (1985) suggest that these disequilibrium textures are more prominent in calc-alkaline rocks and stem from magma mixing of basalts with dacites. Additionally, mechanisms outside of magma mixing such as rapid magmatic decompression have been shown to produce sieved textures in plagioclase cores (Nelson and Montana, 1992) as well as sector zoning in clinopyroxene (Brophy et al., 1999). Mineral disequilibrium may also be induced by convective self-mixing within magma chambers (Couch et al., 2001). Given the complexity of arc magmas, it is plausible for all of the aforementioned processes to be involved at a single volcanic center.

Kiska samples commonly have reversed zoning in orthopyroxenes (Fig. 18B). Crabtree and Lange (2011) analyzed seven nearly aphyric andesites and dacites from peripheral vents in the Mexican Volcanic Arc which contain orthopyroxene and commonly have reversed zoning. Through a combination of Fe-Ti oxide thermometry and plagioclase-liquid hygrometry, they were able to determine that pre-eruptive andesites and dacites had water concentrations of 2.8–6.4 and 4.1–8.0 wt. %, respectively. Therefore, magmas had to be volatile-saturated at depths >9 km and >12 km, respectively. Given the broad compositional range found in plagioclase and orthopyroxene, it is inferred that degassing induced crystallization had to have occurred during magmatic ascent. Elevated water content has been shown to increase Fe/Mg K_D values for orthopyroxene (Grove et al., 2003). Combined with phase equilibrium experiments from the literature as well as JANAF thermochemical tables, Crabtree and Lange (2011) suggests that reverse zoning in orthopyroxene from their samples is caused by initial crystallization at greater

depths with higher water concentrations followed by rapid ascent crystallization at shallower depths with lower water concentrations.

Based on geobarometry as well as hygrometry of Kiska samples (see Thermobarometry and Hygrometry in Chapter 5), orthopyroxenes likely fractionated out of the melt in at least two magmatic reservoirs with elevated water content characteristic of calc-alkaline magmas. In conjunction with the presence of sieved plagioclase cores with cohesive rims (Fig. 14F), as well as reverse zoning in orthopyroxene (Fig. 18B), polybaric differentiation of Kiska magmas may have occurred in two stages with the magmas undergoing rapid devolatilization ascent as an intermediary step.

A notable feature of samples from both Gareloi and Kiska volcanoes is the presence of different mineral phases occurring in clusters known as cumulophyric clots (Fig. 14C). In the case of Mount St. Helens, clots have been considered to be cumulates that are not fully representative of all mineral phases fractionating at depth (Scarfe and Fujii, 1987). In conjunction with the presence of variable zonation patterns in plagioclase (Fig. 17 C–F, H), and reverse zoning in orthopyroxene (Fig. 18B), the mineralogy and textural characteristics of Gareloi and Kiska rocks suggests that not all minerals present in the samples analyzed for this study are necessarily phenocrysts but are instead antecrysts.

An antecryst has been defined as “crystals picked up by a magma (rather than crystallizing directly from it), but unlike xenocrysts, antecrysts crystallized largely from progenitors of this magma (e.g. recycled cumulate)” (Jerram and Davidson, 2007). Processes that lead to the presence of antecrysts include magma mixing, magma recharge, and disruption and remixing of cumulates or solidification fronts in the same magma chamber or a deeper storage chamber (Vernon, 2018). A precedent for antecrysts has been noted in the Trans-Mexican

Volcanic Belt wherein initially aphyric melts adiabatically ascended through the crust and picked up plagioclase as crystalline cargo (Zellmer et al., 2016). Additionally, at Crater Lake at least 80% of plagioclase crystals present in rhyodacites and tephra are inferred to be antecrystic (Bacon and Lowenstern, 2005). Within the Aleutians, basalts from Westdahl are noted for having plagioclase crystals with spongy zones that suggest disequilibrium (Nye et al., 2018). Relative to aphyric basalts from the same volcano, the porphyritic basalts have a higher Ca# (Ca[(Ca+Na)]) suggesting that anorthitic plagioclase may be antecrystic. This phenomenon of sieved plagioclase cores is seen in both Gareloi and Kiska samples (Fig. 14F–G). Additionally, anorthite content oscillates from core to rim in Kiska sample 15KKMP005-03 (57–75 mol % An) and Gareloi sample G-05 (70–81 mol % An) before reaching a uniform rim composition (~60 mol % An; Fig. 16A–B). Within Gareloi and Kiska samples microlites are normally zoned (Fig. 17D). Chemical heterogeneity in minerals as well as pervasive disequilibrium textures point towards open system behavior in both Gareloi and Kiska.

A distinction between phenocryst and antecryst is important because if accumulation of antecrysts has occurred, a rock is not truly a representation of a liquid composition (Davidson et al., 2005). Therefore, caution must be taken in any interpretation related to magmatic petrogenesis or subsequent differentiation within arc settings. While numerous mineral compositions from both Gareloi and Kiska are in equilibrium with resident glass, there are notable exceptions (Figs. 19–21). The majority of olivine compositions from both Gareloi and Kiska are not in equilibrium with resident glass (Fig. 19). In the Aleutians, this has been referred to as the "olivine problem" wherein phenocrysts are commonly more Fe-rich that what is predicted by olivine-liquid K_D's between 0.29 and 0.33 (Brophy, 1986). Therefore, the disequilibrium between olivine and glass may not necessarily indicate olivine being antecrystic

in rocks from both Gareloi and Kiska. However, direct evidence of antecrysts from Gareloi is provided by sample G-05 from a shoshonitic Holocene lava flow. Clinopyroxenes from G-05 are not in equilibrium with G-05 glass (Fig. 20D). Instead, they are in equilibrium with glass from G-01 (Fig. 20E); which is from a pyroclastic eruption inferred to have occurred between 2003 and 2015. This provides direct evidence that accumulation of mineral phases has occurred at Gareloi. Additionally, only 50% of Kiska pyroxene compositions were in equilibrium with glass, which suggests Kiska rocks may not be representative of a liquid composition.

Thermobarometry and Hygrometry

Based on thermobarometry, Gareloi and Kiska magmas undergo differentiation at temperatures and pressures that align with the characteristics of tholeiitic and calc-alkaline magmas. The elevated crystallization temperatures in both olivine and clinopyroxene compositions from Gareloi compared to Kiska agree with the assumption that tholeiitic magmas differentiate at higher temperatures relative to calc-alkaline magmas (Fig. 19G; Fig. 22A; Kay et al., 1982). Orthopyroxene likely fractionated out of the melt in at least two magmatic reservoirs (Fig. 23B). The deeper reservoir is inferred to be located at a depth of ~15–25 km (4.6–7.5 kbar). The shallow crustal reservoir is inferred to be located at a depth of ~2.5–13 km (0.8–3.9 kbar). A distinct gap from ~4–7 km depth (1.2–2.2 kbar) may represent a third shallow reservoir that is tapped during eruptions (Fig. 23B). The presence of a sub-volcanic reservoir is further corroborated by clinopyroxene inferred to have fractionated at a depth of ~1–6 km (0.3–2.0 kbar; Fig. 22B). Therefore, Kiska magmas undergo polybaric differentiation which is a defining characteristic of calc-alkaline magmatism (Singer and Myers, 1990). Geobarometry of Gareloi clinopyroxene indicates that differentiation occurs at predominately shallow crustal depths

ranging from ~1 to 13 km (0.3–3.8 kbar; Fig. 22B). Unlike Kiska, the presence of distinct magmatic reservoirs is not indicated by clinopyroxene geobarometry at Gareloi (Fig. 22B).

Elevated water content is a defining characteristic of calc-alkaline magmas (Zimmer et al., 2010). This can be seen for Kiska magmas relative to Gareloi magmas (Fig. 24). Water concentrations in Kiska magmas range from 2.5 to 3.1 wt. % H_2O while water concentrations in Gareloi magmas range from 2.2 to 2.7 wt. % H_2O. Tholeiitic volcanic centers generally have water content <2 wt. %. The elevated water concentrations for Gareloi may be due to Gareloi falling within the transitional tholeiite categorization scheme of Kay and Kay (1994). Therefore, elevated water concentrations relative to highly tholeiitic Aleutian volcanic centers (e.g. Shishaldin; Zimmer et al., (2010) would be expected for Gareloi (Fig. 2). The elevated water concentrations of Gareloi may also explain why magmatic differentiation spans a depth of ~12 km within the shallow crust. Exsolution of ascending hydrous magmas can increase viscosity by several orders of magnitude (Wilson, 1989). This may cause Gareloi magmas to stall and differentiate at a broad, but continuous range of shallow crustal depths prior to eruption.

Calculated water content derived from plagioclase-liquid hygrometry requires an assumption of temperature (Waters and Lange, 2015). Fluctuations in temperature have a significant impact on calculated water content. The assumed temperature of plagioclase fractionation was based on mean anorthite content from EPMA data matched to the temperature at which plagioclase of the same anorthite content fractionated within the MELTS model. For Gareloi, the MELTS model had a starting water concentration of only 2.0 wt. % H_2O (Fig. 25; Fig. 26). This would allow for plagioclase to fractionate earlier in the MELTS model as elevated water content suppresses plagioclase fractionation at shallow crustal depths (Grove and Baker, 1984). Regardless, the same matching method between EPMA data and the MELTS model for a

temperature input into the plagioclase-liquid hygrometer was used for Kiska and attests to an increase in preeruptive water content from transitional tholeiitic Gareloi to transitional calc-alkaline Kiska (Fig. 2; Fig. 24).

MELTS Fractional Crystallization Models

Cogenetic arc rocks are commonly capable of forming coherent trends on bivariate plots. However, a true liquid line of descent is best approximated in aphyric or phenocryst-poor rocks (Cox et al., 1979). In the case of porphyritic rocks such as those in arc settings, the coherent trends instead likely represent random time sequenced eruptions from similarly sourced batches of magma (Wilson, 1989). In effect, what is actually being interpreted are multiple overlapping smaller liquid lines of descent (Cox et al., 1979).

An example of a lack of correlation between extent of differentiation and time is seen for Ruapehu Volcano in New Zealand. Samples from eruptions spanning from 1945–1996 were shown to be heterogenous in geochemistry and associated mineralogy with respect to time (Price et al., 2012). It is suggested that the heterogeneity present in samples vs. time is caused by open system behavior of the magmatic plumbing system. Wherein the plumbing system underlying the volcano is replenished periodically and mixing occurs between stagnant magma and fresh magma injected from below.

The implication being that bulk arc rock compositions are not always representative of liquid compositions and are instead a combination of liquid + phenocrysts + accumulated crystalline cargo (Davidson et al., 2005). This is an important point to make when using arc bulk rock chemistry as a "parent" to simulate fractional crystallization within MELTS. The bulk rock composition is assumed to represent a liquid, but in reality, this may not be the case. Consequently, starting intensive parameters such as pressure, temperature, fO_2, and H_2O may be

offset due to this assumption. This in part may explain why the best fit Gareloi fractional crystallization model has low pressure relative to geobarometric constraints (i.e. 1 kbar vs. ~2.5 kbar) along with elevated fO_2 compared to typical arc tholeiites (i.e. QFM+2 vs. QFM). The chemical differences between Aleutian calc-alkaline and tholeiitic rocks are subtle (McCulloch and Perfit, 1981) and volcanic centers such as Gareloi may not conform to idealized conditions of the tholeiitic series.

Given the overall fit to bulk rock samples, the Gareloi MELTS model suggests that fractional crystallization is likely a dominant mechanism driving differentiation from basalt to dacite within the shallow crust (Figs. 25–26). Using least squares mass balance calculations, Delong et al. (1985) inferred shallow fractionation of plagioclase + clinopyroxene + olivine + magnetite ± apatite at Semisopochnoi. This fractionating assemblage is identical to that produced in the MELTS model for Gareloi. Further corroboration is given by the fact that shallow, isobaric fractional crystallization of tholeiitic magmas is a common phenomenon in extensional regions of the Aleutian arc (Singer and Myers, 1990). Gareloi is situated northwest of the Delarof Island block in an inferred extensional environment (Fig. 1A; Geist et al., 1988).

There are some disparities between the MELTS model and sample data. MgO, FeO_t, and Mg# are all too relatively depleted starting at ~55–58 wt. % SiO_2 compared to Gareloi samples (Fig. 25A-C). Given that clinopyroxenes from Gareloi sample G-05 are in equilibrium with Gareloi sample G-01 glass, this could reflect accumulation of clinopyroxene. Additionally, it is impossible to generate a coherent LLD for Al_2O_3 because Al_2O_3 is too relatively enriched (>20 wt. %) in select basaltic-andesites (Fig. 26A). This may reflect the accumulation of plagioclase which is a common characteristic associated with high-Al basalts (Crawford et al., 1987). However, with the exception of the anomalous calc-alkaline samples, minimal plagioclase

accumulation is suggested by Eu/Eu* for Gareloi samples (Fig. 33C). A negative slope for Eu/Eu* as well as the depletion of Ba relative to Sr (Fig. 34C) with increasing differentiation clearly indicates plagioclase has fractionated in magmas prior to eruption at Gareloi.

In a similar scenario to Ruapehu, rejuvenation of the shallow magma chamber by the injection of fresh magma may have occurred at Gareloi. This could explain what was described at nearby Semisopochnoi in Delong et al (1985) wherein mixing of high-Al basalt with dacite is suggested to have occurred. The fractionation of solid solution minerals should form coherent curvilinear trends on bivariate plots (Cox et al., 1979). This is seen in the most primitive samples from Gareloi and the MELTS model generally captures these trends. However, there is a "Daly Gap" (Daly, 1925) between basaltic-andesites and dacites that form a linear array suggestive of mixing (i.e. Fig. 25D). Glass compositions do not conform to bulk element sample trends or the MELTS LLD. If rocks from Gareloi were a true representation of the liquid, glass compositions should conform with bulk sample trends.

Based on thermobarometry of minerals within Kiska samples, magmas undergo polybaric differentiation in at least two crustal levels underlying the volcano (0.8–3.9 kbar and 4.6–7.5 kbar; Fig. 23B). Reverse zoning in orthopyroxene suggests that magma transport may be relatively rapid between these reservoirs (Fig. 18B). Given that MELTS was never designed to simulate fractional crystallization of hydrous, calc-alkaline magmas (Nandedkar et al., 2014), fractional crystallization modeling was attempted only in the upper crustal magma chamber to determine if basaltic-andesites from Kiska represent liquid compositions. If this was the case, the MELTS liquid line of descent should span from basaltic-andesite samples to Kiska glass (Table 5). In general there is an overall good fit for MgO, CaO, CaO/Al_2O_3, and K_2O (Fig. 25A, D; Fig. 26B, D). However, FeO_t is too enriched (~4 wt. %) relative to glass (~3 wt. %) which also causes

Mg# to be ~19 as opposed to ~34 at 69 wt. % SiO_2 (Fig. 25B). This may be an effect of fO_2 (QFM+2) being too low in the MELTS model which preferentially fractionates silicate minerals instead of non-silicate minerals such as magnetite. Given the paucity of samples from Kiska, it is unknown whether more evolved rocks are present on the island. If they are, the MELTS LLD suggests further differentiation from basaltic andesite could occur by fractional crystallization in a shallow crustal magma reservoir. This may be the case for Little Sitkin, as the Kiska MELTS LLD does tend to follow a similar trend.

Alkalic Volcanic Centers

The alkalic nature of tholeiitic Gareloi and Semisopochnoi magmas is a confounding geochemical feature that distinguishes them from nearly all other volcanoes residing on or proximal to the Aleutian ridge (Fig. 27). Gareloi magmas reside within the high-K field of Gill (1981) (Fig. 26D) yet fall within the tholeiitic field of Miyashiro (1974) (Fig 2). The only other volcanic centers in the Aleutians that erupt lavas with comparable alkalinity are Bogoslof (~168°W) and Amak (~163°W). Interestingly, samples from both volcanoes are also designated as being tholeiitic (Morris and Hart, 1983; Loewen et al., 2019).

K_2O has been noted for varying more than other major elements within andesites from different tectonic settings. K, Rb, La, Th and U contents and La/Yb and Rb/Sr ratios always increase relative to silica away from the plate boundary (Gill, 1981). Such variations are suggested to be in part due to different mantle sources and different extents of partial melting. Bogsolof resides 235 km north of the trench while Amak resides 275 km north (Fig. 1D). Meanwhile Gareloi resides 170 km north and Semisopochnoi resides 185 km north. The depth to the top of the subducting slab increases relative to the distance from the volcanic front. Bogoslof has a depth to slab of 132 km (Fig. 1C). No depth to slab value is available for Adak. Loewen et

al. (2019) suggests that Bogsolof magmas derive their alkalic signature from a mantle source that has elevated residual garnet and lower degrees of partial melting relative to volcanoes closer to the trench in the area (e.g. Makushin). Morris and Hart (1983) suggest a similar scenario for Amak and note that Amak lavas have elevated concentrations of Sr and Ba relative to nearby Cold Bay lavas. The inferred distance to the slab at Gareloi is 71 km, whereas adjacent Semisopochnoi is 106 km (Fig 1C). This disparity in inferred depth to the slab is likely in part attributable to the position of Gareloi and Semisopochnoi being located north of the Delarof crustal block and the Rat Island block respectively (Fig. 1A). While notable, this stark shift in depth to slab has not been correlated with alkalic volcanism occurring within the Aleutians. Given that La/Yb in Gareloi basalt and basaltic-andesites ranges from ~6 to 9 (Fig. 33B) and have elevated Sr and Ba for the area (Fig. 34C), this anomalous geochemical signature is likely attributable to extents of partial melting and/or source composition.

Principal Component Analysis

PC1 is interpreted as representing the differentiation of mafic magmas to more evolved compositions. This is corroborated by the linear shift in score location when sorted by SiO_2 concentration (Fig. 29A). Additionally, on the distance bi-plot (Fig. 28B), loading vectors for PC1 depict a strong positive correlation with SiO_2 and a strong negative correlation with MgO, CaO, and FeO with all three of the latter being associated with mafic rocks (Cox et al., 1979). Ingenstrem Depression samples have been noted for being primarily basalts and dacites with basaltic-andesites and andesites being sparse and having more geochemical variability especially with regards to K_2O (Yogodzinski et al., 2015). This lack of intermediate Ingenstrem Depression samples and their geochemical variability was detected by PCA (Fig. 28B). In addition, samples

from the Western Cones which have anomalously high SiO_2 (69–70 wt. %) all aggregate in a tight cluster towards the bottom right of the plot.

PC2 is interpreted as representing the discrimination between the tholeiitic and calc-alkaline series (Fig. 29B). Tholeiitic centers have a protracted increase in SiO_2 relative to FeO (Kay et al., 1982). This is reflected in the steep initial upward trend for Gareloi and Semisopochnoi indicating the role of Fe-enrichment in both tholeiitic magmatic suites (Fig. 28B). In contrast, calc-alkaline magmas are characterized by SiO_2 enrichment relative to FeO (Kay et al., 1982). This trend is exemplified by Ingenstrem Depression and Western Cones samples which are highly calc-alkaline (Fig. 2) and plot at lower values for PC2 (Fig. 29B).

Harker diagrams have been used to compare elemental abundances of samples from tholeiitic and calc-alkaline Aleutian volcanoes with particular emphasis on intermediate to high SiO_2 content (Kay et al., 1982). Tholeiitic samples were noted for being enriched in FeO, K_2O, TiO_2, and Na_2O at a given SiO_2 content relative to calc-alkaline volcanoes. While CaO and MgO values were noted for being higher at calc-alkaline volcanoes for a given SiO_2. This trend is corroborated by PCA and further illustrates the along-strike transition in magmatic series within the distal Aleutians.

The only anomaly with regards to the PCA and the findings of Kay et al. (1982) is Al_2O_3 content. Kay et al. (1982) suggests calc-alkaline centers are associated with higher Al_2O_3 content at intermediate to high levels of SiO_2. PCA denotes an association with Al_2O_3 and tholeiitic centers (Fig. 28A). One explanation for this is that Al_2O_3 is typically associated with the role of plagioclase either as a fractionating or accumulated phase within island arc rocks. Calc-alkaline rocks from island arcs are commonly highly porphyritic relative to tholeiitic rocks and particularly rich in plagioclase phenocrysts (Wilson, 1989). Therefore, the expectation would be

an association with Al_2O_3 and calc-alkaline rocks. However, Yogodzinski et al. (2015) noted that the most petrographically anomalous feature of their highly calc-alkaline andesitic samples was a distinct lack of plagioclase. This suggests that the lack of a positive correlation between calc-alkaline samples and Al_2O_3 at 53–67 wt. % SiO_2 may simply be a feature of the anomalous nature of the primitive andesites found within the westernmost portion of the distal Aleutians.

The reason Kay et al. (1982) and others commonly place emphasis on intermediate to high SiO_2 compositions (>54 wt. % SiO_2) when comparing the two series is that they are not readily distinguishable from each other at lower SiO_2 content. This phenomenon is commonly attributed to the hypothesis that both series are derived from the same parental magma (e.g. Kay et al., 1982, 2019). However, others have suggested that both series are derived from unique parental magmas (Cai et al., 2015). An overlap in magmatic series at <54 wt. % SiO_2 is apparent from PCA (Fig. 29B) suggesting that distal Aleutian magmas may in large part be derived from a common parental magma. The exception being volcanoes west of Kiska which do not have the same overlap (Fig. 28B; Fig. 29B).

A final notable feature with regards to PC2 is that P_2O_5 has a significantly greater loading (0.53) than FeO (0.21) (Fig. 28A). The influence of P_2O_5 is not typically interpreted to be a defining characteristic of discriminating between the calc-alkaline and tholeiitic series. However, it clearly plays a major role in delineating between the two magmatic series present within the distal Aleutians. Both Gareloi and Semisopochnoi magmas have been hypothesized to have undergone extensive fractional crystallization in the upper crust prior to eruption (Coombs et al., 2012, 2018). Whereas both the Ingenstrem Depression and the Western Cones have been hypothesized to have undergone "minimal fractional crystallization within the crust" (Yogodzinski et al., 2015). This lack of fractional crystallization for the westernmost portion of

the distal Aleutians implies the geochemical signature for magmas of this region is mainly a byproduct of sub-crustal processes including partial melting of the mantle. Partial melting of the mantle generates low concentrations of P_2O_5 (<0.2 wt. %; Lee and Bachmann, 2014). The relative abundance of P_2O_5 within magmas undergoing fractional crystallization increases from mafic through intermediate magmatic compositions until the fractionation of apatite occurs (Lee and Bachmann, 2014). The implication being that the positive correlation between a strong P_2O_5 loading for tholeiitic intermediate magmas and negative correlation for highly calc-alkaline magmas within the distal Aleutians serves as a proxy for the occurrence of fractional crystallization (e.g. Gareloi) or lack thereof (e.g. Western Cones).

Rare Earth Element Trends

REE patterns of basaltic to andesitic liquids are not significantly affected by gabbroic assemblages (plagioclase + pyroxene ± olivine; Rollinson and Pease, 2021). Therefore, the role garnet and amphibole may play as a residual source component or fractionating phase in arc magmas may be determined by analysis of REE ratios. La/Yb increases during both garnet and amphibole fractionation. Meanwhile, garnet will increase Dy/Yb and amphibole will decrease Dy/Yb. Like amphibole, clinopyroxene also decreases Dy/Yb however, K_D REE clinopyroxene << K_D REE amphibole (Davidson et al., 2007). Dy/Dy* vs. Dy/Yb can further measure the concavity of a REE pattern with a concave up shape suggesting amphibole control and concave down shape suggesting garnet control (Davidson et al., 2013). Given that garnet is stable at 16 kbar while amphibole is stable at 8 kbar for basaltic compositions (Rapp and Watson, 1995), both Dy/Yb vs SiO_2 wt.% and Dy/Dy* vs. Dy/Yb are inferred to delineate between a garnet residual source component and lower–middle crustal fractionation/accumulation of amphibole for arc magmas (Davidson et al., 2007, 2013).

Decreases in both Dy/Yb and Dy/Dy* suggest that amphibole fractionation has occurred in all distal Aleutian volcanoes besides the Western Cones (Fig. 30A–B). While none of the samples analyzed in this study were found to contain amphibole, Gareloi samples from a Pleistocene lava flow as well as samples from the 1929 eruption both contain minor amounts of amphibole (Coombs et al., 2012). Amphibole is also reported in samples from Kiska (Coats, 1959) as well as Buldir (Waters et al., 2021). Amphibole is present in basaltic-andesites – rhyodacites from Ingenstrem Depression and the Western Cones (Yogodzinski et al., 2015). However, the influence of residual garnet obscures amphibole fractionation in Western Cones samples (Fig. 30A–B).

Further evidence for lower–middle crustal amphibole fractionation in the western Aleutians is present from adjacent volcanoes. Based upon high La/Yb, low HREE, and concave REE patterns, Kanaga tephra are thought to have undergone fractionation of amphibole at depths >7 km (Romick et al., 1992). Hidden Bay and Kagalaska plutons on Adak Island are thought to have originated from basalt that fractionated olivine and clinopyroxene in the lower crust to form high-Al basalt (Jicha and Kay, 2018). In the mid–crust, assimilation and crystallization is inferred to have left behind gabbro and coarse-grained diorite cumulates of pargasitic amphibole at depths >12 km (Jicha and Kay, 2018). Both Hidden Bay and Kagalaska plutons in the region are similar geochemically to surrounding volcanic rocks (Kay et al., 1990). Additionally they are thought to represent the final stages of a magmatic cycle within the arc prior to magmatism migrating north or becoming entirely dormant (Kay et al., 1990). Therefore, it is plausible that even when not visible in extrusive rocks, amphibole may be a cryptic fractionating phase that dictates differentiation trends. A corollary for this scenario is seen at The Quill and Mt Pelée in the Lesser Antilles wherein amphibole is sparse (<5%) in volcanic rocks yet is a preeminent

phase in cumulate plutonic blocks from both volcanoes (Arculus and Wills, 1980). Amphibole is inferred to exert primary control on differentiation trends at both volcanoes even though it is not present as a phenocryst phase in volcanic rocks (Davidson and Wilson, 2011).

With increasing differentiation the expectation is for the shapes of REEs from a suite of rocks to roughly parallel each other but have overall higher relative concentrations. This would imply that the samples are comagmatic and could be related through crystal fractionation. However, parallel trends could also represent magma mixing of end members resulting in similar slopes. Within the distal Aleutians, as rocks become more evolved, REE concentrations do increase (Fig. 32A–C). In contrast to major elements, REE concentrations do not show the same systematic shift along-strike for the region. The overall trend of basalt REE from Gareloi–Kiska is generally uniform. However relative concentrations are variable and suggest differences in source composition. This may be due to the amount of eclogite melt, sediment, or fluid from the subducting slab (Fig. 34) and the extent of interactions of these components with mantle peridotite. Both Buldir and Ingenstrem Depression basalts have different LREE concentrations, however; HREE are depleted relative to LREE for samples from both locations indicating an increasing residual garnet component influencing primitive rock compositions in the western distal Aleutians (Fig. 32A). Western Cones dacites are end member compositions with an increased garnet signature as seen by elevated La/Yb (~10–27; Fig. 31C; Fig. 33A). This shift in REE pattern uniformity west of Kiska suggests a major transition in source components as the volcanic front migrates off of the arc ridge (Fig. 4A; Fig. 31; Fig. 32).

Fractionation of plagioclase becomes evident for Gareloi–Kiska at andesitic compositions given the presence of negative Eu anomalies (Fig. 32B). Since Eu^{2+} prefers substitution for Ca in plagioclase in reducing conditions (Winter, 2001), the magnitude of the Eu anomaly for western

volcanic centers such as Kiska may not fully represent the extent of plagioclase fractionation. For instance, Kiska samples are more plagioclase-rich than Gareloi samples (Table 1), but this may not be readily apparent from REE trends (Fig. 31; Fig. 32). Ingenstrem Depression and Western Cones samples with SiO_2 >60 wt. % have positive Eu anomalies and do contain plagioclase phenocrysts (Yogodzinski et al., 2015) suggesting that accumulation of plagioclase has occurred.

Within the Aleutians, samples with steep REE patterns (La/Yb >6) have generally lower FeO/MgO and are associated with the calc-alkaline series (Kay and Kay, 1994). While less steep La/Yb (La/Yb <3) is associated with higher FeO/MgO and is associated with the tholeiitic series. Variations in intermediate La/Yb (3–5) are suggested to be in part influenced by source characteristics as well as fractionating mineralogy (Kay and Kay, 1994). In the case of Gareloi, FeO/MgO is high (tholeiitic; Fig. 2), yet La/Yb is up to ~9 for basaltic andesites (Fig. 33B), which directly contrasts with the expectation of a tholeiitic center. Instead of having similar La/Yb to adjacent Semisopochnoi, Gareloi samples more closely parallel samples from calc-alkaline Ingenstrem Depression cones (Fig. 33A–B). Additionally, La/Yb steeply increases for basaltic-andesites yet levels off at ~8 La/Yb for andesites and dacites. Given that La is more incompatible than Yb, the expectation would be that La/Yb would have a positive slope with increasing differentiation. This tapering off of La/Yb provides further evidence that mixing, or assimilation has occurred in Gareloi magmas. Volcanoes such as Little Sitkin and Kiska are designated as calc-alkaline based on FeO/MgO yet La/Yb is ~4, which places them nearly into the tholeiitic categorization scheme of Kay and Kay (1994).

This decoupling of trace and major element trends in the distal Aleutians may be explained by island arc basalt REE patterns being correlated with the relative amount of LILE

(e.g. Sr, K, Ba) present within the suite (Wilson, 1989). Consequently, even though Gareloi is categorized as tholeiitic, its anomalously alkalic geochemical signature (Fig. 9) and elevated Sr and Ba (Fig. 34C), supersedes magmatic series when analyzing REE patterns. The relative enrichment in LREE, Sr, Ba, K, and Pb are commonly thought to be derived from the source, either from the subducting slab or from peridotite in the mantle (Wilson, 1989). A similar trend at Semisopochnoi and Bogosolof is present and it has been suggested that metasomatic enrichment of the mantle due to dehydration of the subducted slab may account for this distinct geochemical signature (McCulloch and Perfit, 1981; Delong et al., 1985).

High-Al Basalt Parental Magma

Based on bulk rock and mineral chemistry analysis combined with geothermometry, middle–upper crustal processes within the distal Aleutians have been explored. A precedent for Kiska magmas undergoing polybaric differentiation has been established based on geobarometric constraints. Thermobarometry and MELTS modeling have indicated that basaltic-andesites differentiate to dacites within the upper crust underneath Gareloi. A fundamental question that remains is whether the aforementioned processes can be related to a common magmatic parent within the lower crust.

A parental magma is a magma that more evolved magmas are thought to be derived from. In the case of the Aleutians, high-Al basalt is inferred to be the predominate parent (Kay and Kay, 1994). It is likely derived from a high-Mg basalt that becomes stagnated in the lower crust due to density contrasts with ambient country rock and declining isotherms which inhibit magmatic ascent (Gust and Perfit, 1987). Through the fractionation of olivine and clinopyroxene, and to a lesser extent spinel and amphibole, less dense high-Al basalts and basaltic andesites may be produced (Gust and Perfit, 1987). Following lower crustal differentiation, magmas may

follow a tholeiitic to calc alkaline trend based on whether they reside in a crustal region of relative extension or compression (Fig. 8; Kay et al., 1982; Kay and Kay, 1994). Within this framework, it is tangible to have a common high-Al parent for both Gareloi (tholeiitic) and Kiska (calc-alkaline) magmas.

Following the categorization scheme of Kay and Kay (1994), high-Al basalts within the Aleutians contain 17–21 wt. % Al_2O_3, have high FeO/MgO ratios (>1.8), low MgO (<5 wt. %), as well as low Ni and Cr content. Additionally, olivine compositions typically range from 70 to 79 mol % Fo and plagioclase compositions range from 80 to 90 mol % An. When compared to representative compositions of high-Al basalt throughout the arc compiled in Kay and Kay (1994), both Kiska sample 51P54 and Gareloi sample 03GRBB59 meet the requirements of high-Al basalt compositions (Table 6).

While the samples from Kay and Kay (1994) listed in Table 6 were not available for analysis in this study, some parallels in mineral chemistry are worth highlighting. Fo content in olivine cores from Kiska basaltic-andesite sample 15KKMP006-01 range from 76 to 78 mol % (Fig. 15B). The olivine rim has lower Fo content (70 mol %) and is mantled by orthopyroxene suggesting a peritectic reaction between olivine + melt (Fig. 18A). The most anorthite-rich plagioclase compositions from Gareloi and Kiska basaltic-andesites bound the lower limit of high-Al basalt anorthite content (Fig. 15C). Therefore, it can be established that based on bulk rock chemistry, high-Al basalts are present from both Gareloi and Kiska and that mineral compositions from more evolved rocks are consistent with those of high-Al basalts through magmatic differentiation. Further evidence for a shared high-Al basaltic parent comes from experimental phase relation studies.

While Korovin lavas from Atka Island (174°W) are designated as transitional tholeiites (Kay and Kay, 1994) as opposed to transitional calc-alkaline (Kiska), polybaric differentiation of parental high-Al basalt involving crystallization at similar depths to Kiska is seen for Korovin volcano basalts and andesites in the experimental phase relation studies of Baker and Eggler (1987). It is suggested that primitive high-alumina basalts differentiated in deep magma reservoirs at 5–8 kbar. Fractionating phases at these depths are not listed, but it is shown that fractionation of plagioclase + olivine + augite or plagioclase + augite + pigeonite exclusively at this pressure range is incapable of generating the major element concentrations of Korovin rocks. Therefore, Korovin magmatic differentiation is a multi-stage, polybaric process wherein Korovin rock mineralogy only captures the last stage of these processes. Basaltic andesites are inferred to have differentiated toward andesitic compositions between 2–5 kbar at 2 wt. % H_2O with a fractionating assemblage of plagioclase, augite, and either olivine or orthopyroxene. Additionally, dacites are shown to be produced from andesites through the fractionation of plagioclase, augite, and orthopyroxene at the same pressure but with higher water content. While samples from Kiska are limited and are generally basaltic-andesites, the parallels between Kiska and Korovin mineralogy, magmatic series, and geobarometric constraints suggests similar magmatic evolutionary histories.

Given that high-Al basalt differentiation in the 5–8 kbar range is inferential in Baker and Eggler (1987) and polybaric differentiation of orthopyroxene is apparent for Kiska magmas (Fig. 23B), another experimental analogue may be used to address deeper crustal processes for both Kiska and Gareloi. Gust and Perfit (1987) use sample MK-15 from Makushin with the assumption that it represents a parental high-Mg basalt. With their experimental phase relation study they show that a high-Mg basalt will differentiate in the lower-middle crust to a high-Al

basalt. Assuming that Kiska and Gareloi share a common high-Al basaltic parent, comparisons between phase relations from Gust and Perfit (1987) and thermobarometric constrains provide a coherent model for how most distal Aleutian magmas differentiate.

At ~8 kbar and ~1250 °C olivine and clinopyroxene are the fractionating phases present producing a high-Al basalt from a high Mg-basalt which is parental to both Kiska and Gareloi magmas (Fig. 35). Kiska magmas cross the phase line at ~8 kbar and ~1200 °C and continue to fractionate olivine and clinopyroxene with the addition of orthopyroxene, and plagioclase. Adhering to calc-alkaline differentiation trends, Kiska magmas stall and crystalize phases at lower temperatures and higher pressures relative to tholeiitic Gareloi. Gareloi magmas differentiate to high-Al basalt at ~8 kbar by fractionating clinopyroxene and olivine. Evidence for deeper crustal fractionation is seen by the two clinopyroxene compositions which formed at ~6 kbar and 8.5 kbar (Fig. 22B). Adhering to characteristic tholeiitic magma behavior, Gareloi magmas ascend relatively rapidly through the crust with minimal heat loss (~50 °C) and plagioclase begins to fractionate. Extensive clinopyroxene fractionation at elevated temperatures (~1075 °C) and shallow depths (0.3–3.8 kbar) is evidenced by thermobarometric constraints (Fig. 22B).

One important point to make with regards to the phase relation study of Gust and Perfit (1987) is that it was conducted on an anhydrous basis. Sisson and Grove (2003) suggest that parental Aleutian high-MgO basalts contain ~2.5–4.5 wt. % H_2O. Baker and Eggler (1983) suggests that high-Al basalts from Korovin volcano contain 1–2 wt. % H_2O. H_2O would have the effect of lowering the liquidus at any given pressure on the phase diagram seen in Fig. 35 and may also cause amphibole to be a fractionating phase. For instance, Baker and Eggler (1983) suggest that when high-Al basalts have water concentrations of 4–6 wt. % at 2 kbar underneath

Korovin volcano, amphibole has to be near or on the liquidus. Given the negative trends in Dy/Yb and Dy*/Dy (Fig. 30), estimated preeruptive water contents of 2.5 wt. % for Gareloi and 2.8 wt. % for Kiska, MELTS modelling (Figs. 25–26), as well as amphibole bearing cumulates inferred to have formed at >6 kbar underneath Adak Island volcanoes (176.5 °C) (Conrad and Kay 1984), it is likely that distal Aleutian magmas are hydrous and fractionate amphibole. As suggested by Davidson (2007), there may be a lower-middle crustal reservoir wherein amphibole cumulates act as filter for water dissolved in mantle-derived magmas. This would explain why the high-MgO basalts of Sisson and Grove (1993) have elevated water concentrations compared to the more evolved high-Al basalts from Baker and Eggler (1983) and why the anhydrous phase relations of Gust and Perfit (1987) do approximate the inferred differentiation trends of Gareloi and Kiska.

Through these two experimental analogs as well as the evidence outlined herein, a precedent for a common high-Al basaltic parent for Gareloi and Kiska has been established. Given that major element and trace element trends (to a lesser extent) are gradational between the two volcanic centers, it can be inferred that Semisopochnoi and Little Sitkin also share the same parental magma. For instance, Semisopochnoi samples are thought to be derived from a high-Al basaltic parent (Delong et al., 1985). However, the same cannot be said for volcanoes west of Kiska.

Buldir basaltic-andesite tephras are inferred to be produced by crystallization of a parental liquid at ~8 kbar under hydrous and oxidizing conditions followed by crystallization at ~2 kbar (Waters et al., 2021). This places Buldir magmas in a similar framework to what has been outlined for Kiska; however, there are some caveats. While Baker and Eggler (1987) applied a fO_2 buffer near nickel-nickel oxide (NNO), Waters et al. (2021) applied a fO_2 buffer

near rhenium-rhenium oxide (Re-ReO_2), which implies higher fO_2. The occurrence of oxides on the basalt liquidus is correlated with high $Fe^{3+}/\sum Fe$ (Botcharnikov et al., 2008). This may explain why Buldir magmas have chromite as a liquidus phase and lack orthopyroxene, yet still parallel the depths at which differentiation occurs at Kiska. Additionally, there are no high-Al basalts present west of Kiska. All Buldir samples have FeO/MgO <1.8 and all but one sample (BUL6A) have MgO >5 wt. %. Instead, Buldir samples follow a similar trend to Ingenstrem Depression samples with regards to basaltic HREE depletion relative to LREE (Fig. 32A), La/Yb vs. SiO_2 (Fig. 33A–B), Mg# vs. SiO_2 (Fig. 33D), and Th/La vs. Mg# (Fig. 34B). With increased samples collected and analyzed from Buldir, this alignment with Ingenstrem Depression samples would likely be even more pronounced. Ingenstrem Depression (and Western Cones) magmas are not derived from a basaltic parent that has undergone fractional crystallization (Yogodzinski et al., 2015) which obviates the presence of a common high-Al basaltic parent. Given the evidence presented that the parental magma in the region likely shifts west of Kiska, the petrogenetic origins of distal Aleutian magmas may be addressed to uncover what source processes dictate primary and subsequent parental magma compositions.

Source Components

Within the distal Aleutians a MORB eclogite melt and aqueous fluid component increases while sediment flux decreases systematically westward (Figures 34A–B, D). High Sr/Y (>50) is a defining characteristic of the aforementioned high Mg# andesites found within select localities of the Aleutian arc (Kelemen et al., 2003b). In conjunction with steep REE patterns, it is suggested that a basaltic melt component at eclogite facies derived from the subducting slab is necessary to drive these geochemical trends (Kay, 1978; Yogodzinski et al., 2017). Ingenstrem Depression and Western Cones samples both have high Sr/Y (Fig. 34A), steep REE patterns

(Fig. 32; Fig. 33A–B), and high Mg# (Fig. 33D). Alternatively, volcanic centers that reside on the arc ridge appear to grade towards an increased eclogite melt component as indicated by increasing steepness in REE patterns and Mg#. However, Sr/Y is elevated for more primitive Gareloi samples (Fig. 34A). Instead of eclogite melt, this may reflect metasomatic reactions between mantle peridotite and a sediment derived fluid and/or melt (Castillo, 2012). A similar scenario has been suggested for Semisopochnoi (Delong et al., 1985). Additionally, the low Mg# of Gareloi andesites precludes them from being high Mg# andesites (Kelemen et al., 2003a). Therefore, the overall trends in REE patterns, Sr/Y, and Mg# suggest a gradational shift to an increased eclogite melt source component westward within the distal Aleutians.

Incompatible elements such as U, Th, and Ba do not vary based on magmatic series and are established in the source region (Kay and Kay, 1994). Ba has been invoked to describe a subducted fluid component dehydrated off of the slab due to its mobility in an aqueous fluid compared to La, Nb, and Ta which are relatively immobile (Elliott et al., 1997). However in the Aleutians, both Ba/La and Th/La correlate well with Pb radiogenic isotopic ratios (Yogodzinski et al., 1994). Elevated radiogenic Pb isotopic ratios have been associated with the presence of a recycled terrigenous sediment component in the subducted slab (Hawkesworth et al., 1997). Therefore, it is inferred that Ba, Pb, and Th in Aleutian magmas are transported from the subducted slab via a partial melt of sediment instead of an aqueous fluid (Yogodzinski et al., 1994; Kelemen et al., 2003a).

In conjunction with highly depleted isotopic compositions (e.g. Tl, Sr, Pb) incompatible trace element ratios such as Th/La suggest that west of Buldir, sediment flux from the subducted slab is minimal (Yogodzinski et al., 2015; Nielsen et al., 2016). Within the distal Aleutians, Th/La systematically decreases westward. This suggests that this region captures the transition

from a sediment component (which likely influences primary magma compositions within the arc) to the primitive high Mg# andesites and dacites influenced predominately by an eclogite melt component (Fig. 34A–B). Further supporting this suggestion, Ba concentrations gradationally decrease westward from Gareloi (~580–1275 ppm) to Kiska (~200–425 ppm) and correlate with decreasing Th/La (Figure 34B–C).

Further support for a westward decrease in sediment comes from U/Th vs. Th. U is inferred to be preferentially mobilized in a fluid component from the subducted slab while Th is less fluid mobile and is preferentially mobilized in the sediment component (Hawkesworth et al., 1997). Eastern distal Aleutian volcanic centers have an affinity for a stronger sediment source component (Fig. 34D). Whereas from Kiska westward, a role for a dehydrated slab fluid component is evident. It is notable that the fluid component is most pronounced in Kiska and Ingenstrem Depression samples and suggests that a greater proportion of eclogite melt dominates Western Cones compositions.

The shift in tectonic regime present within the distal Aleutians as well as the Komandorsky block to the west likely exerts primary control on the proportion of eclogite melt, sediment melt, and fluid components fluxing the mantle underneath the distal Aleutians. The decrease in orthogonal convergence velocity (Fig. 1B) results in increased heating of the subducted slab and cooling of the overlying mantle (Kincaid and Sacks, 1997). Combined with increased heating of the slab due to the tear in the subducting Pacific Plate (Fig. 4B; (Yogodzinski et al., 2001) the eclogite melt component would be expected to systematically increase westward, which it does. As the amount of sediment entering the subduction zone decreases westward (Kelemen et al., 2003a) even with elevated temperatures causing greater extents of partial melting, a sediment melt signature would decrease westward. Lastly, a fluid

component fluxing the mantle would become more pronounced as sediment input decreases (i.e. Kiska). However as slab temperature increases, dehydration of the lithosphere would result in less H_2O being available to flux the mantle wedge (Kelemen et al., 2003a). The end result being the anomalous high Mg# rhyodacites of the Western Cones.

CHAPTER 7

CONCLUSION

Based on the combination of whole-rock chemistry analysis for all distal Aleutian volcanoes, mineral chemistry analysis and thermobarometry for Gareloi and Kiska volcanoes, and thermodynamic modeling, a gradational shift in both primary magmatic composition and subsequent differentiation trends is present within the distal Aleutians. This shift in geochemistry is coincident with a westward decrease in orthogonal convergence velocity and decrease in dip of the subducting slab (Syracuse and Abers, 2006), which results in an increasingly hotter subducting plate and cooler overlying mantle wedge (Kincaid and Sacks, 1997; Kelemen et al., 2003a). Additionally, the presence of a tear in the subducting Pacific Plate proximal to the Aleutian-Kamchatka junction may play a significant role in the thermal regime underlying the Komandorsky block and the distal Aleutians (Yogodzinski et al., 2001). This tear in the Pacific plate likely causes increased heating of the subducting plate by asthenospheric flow. Sediment flux to the mantle from the subducted slab decreases while an aqueous fluid and MORB eclogite melt systematically increase westward. This results in the generation of a primary picritic basalt underneath the distal Aleutian volcanoes residing on the arc ridge (Gareloi–Kiska) that is characteristic of the majority of the arc (Kay and Kay, 1994). Subsequent fractionation of olivine within the mantle generates high-Mg basalt which stalls in the lower crust to produce a parental high-Al basalt common to both the tholeiitic and calc-alkaline magmatic series (Gust and Perfit, 1987). High-Al basalt undergoes further differentiation and follows a tholeiitic (Gareloi) or calc-

alkaline (Kiska) trend based on whether a volcanic center resides in the center or edge of one of the five crustal blocks composing the Aleutian arc (Kay et al., 1982).

Negative trends for Dy/Yb vs. SiO_2 and Dy/Dy* vs. Dy/Yb suggest that amphibole fractionates within the lower–middle crust throughout the distal Aleutians. However, this trend is obfuscated by an increased garnet source signature in the Western Cones samples, even though amphibole is an observed phase in these rocks (Yogodzinski et al., 2015). Buldir and Ingenstrem Depression samples capture the westward shift to a more pronounced MORB eclogite source as indicated by gradational increases in Mg#, La/Yb, and Sr/Y. Coupled with the fact that no high-Al basalt samples are present in the distal Aleutians west of Kiska, it is likely that a shift in primary and subsequent parental magma is coincident with the volcanic front migrating northward off of the arc ridge west of Kiska. An eclogite melt component from the subducted slab may be present in all Aleutian magmas (Yogodzinski et al., 2017) or be relegated exclusively to the western Aleutians (George et al., 2003; Jicha and Kay, 2018). Regardless, the volcanoes within the distal Aleutians represent the surficial expression of a dynamic subduction zone.

References

Annen, C., Blundy, J.D., and Sparks, R.S.J., 2006, The Genesis of Intermediate and Silicic Magmas in Deep Crustal Hot Zones: Journal of Petrology, v. 47, p. 505–539.

Arculus, R.J., 2003, Use and Abuse of the Terms Calc-alkaline and Calc-alkalic: Journal of Petrology, v. 44, p. 929–935.

Arculus, R.J., and Wills, K.J.A., 1980, The Petrology of Plutonic Blocks and Inclusions from the Lesser Antilles Island Arc: Journal of Petrology, v. 21, p. 743–799.

Armstrong, J.T., 1988, Quantitative analysis of silicate and oxide materials: comparison of monte carlo, ZAF, and ψ(ρz) procedures: Microbeam Analysis, p. 239–246.

Atwater, T., 1989, Plate tectonic history of the northeast Pacific and western North America, *in* Winterer, E.L., Hussong, D.M., and Decker, R.W. eds., The Eastern Pacific Ocean and Hawaii, North America, Geological Society of America, p. 21–72.

Bacon, C., and Lowenstern, J., 2005, Late Pleistocene granodiorite source for recycled zircon and phenocrysts in rhyodacite lava at Crater Lake, Oregon: Earth and Planetary Science Letters, v. 233, p. 277–293.

Bacon, C.R., Sisson, T.W., and Mazdab, F.K., 2007, Young cumulate complex beneath Veniaminof caldera, Aleutian arc, dated by zircon in erupted plutonic blocks: Geology, v. 35, p. 491–494.

Baker, D.R., and Eggler, D.H., 1983, Fractionation paths of Atka (Aleutians) high-alumina basalts: Constraints from phase relations: Journal of Volcanology and Geothermal Research, v. 18, p. 387–404.

Baker, D.R., and Eggler, D.H., 1987, Compositions of anhydrous and hydrous melts coexisting with plagioclase, augite, and olivine or low-Ca pyroxene from 1 atm to 8 kbar; application to the Aleutian volcanic center of Atka: American Mineralogist, v. 72, p. 12–28.

Beattie, P., 1993, Olivine-melt and orthopyroxene-melt equilibria: Contributions to Mineralogy and Petrology, v. 115, p. 103–111.

Behn, M.D., and Kelemen, P.B., 2003, Relationship between seismic P-wave velocity and the composition of anhydrous igneous and meta-igneous rocks: Geochemistry, Geophysics, Geosystems, v. 4

Botcharnikov, R.E., Almeev, R.R., Koepke, J., and Holtz, F., 2008, Phase Relations and Liquid Lines of Descent in Hydrous Ferrobasalt—Implications for the Skaergaard Intrusion and Columbia River Flood Basalts: Journal of Petrology, v. 49, p. 1687–1727.

Brophy, J.G., 1986, The Cold Bay Volcanic Center, Aleutian Volcanic arc: Contributions to Mineralogy and Petrology, v. 93, p. 368–380.

Brophy, J.G., and Marsh, B.D., 1986, On the Origin of High-Alumina Arc Basalt and the Mechanics of Melt Extraction: Journal of Petrology, v. 27, p. 763–789.

Brophy, J., Whittington, C., and Park, Y.-R., 1999, Sector-zoned augite megacrysts in Aleutian high alumina basalts: Implications for the conditions of basalt crystallization and the generation of calc-alkaline series magmas: Contributions to Mineralogy and Petrology, v. 135, p. 277–290.

Burns, L.E., 1985, The Border Ranges ultramafic and mafic complex, south-central Alaska: cumulate fractionates of island-arc volcanics: Canadian Journal of Earth Sciences, v. 22, p. 1020–1038.

Buurman, H., Nye, C.J., West, M.E., and Cameron, C., 2014, Regional controls on volcano seismicity along the Aleutian arc: Geochemistry, Geophysics, Geosystems, v. 15, p. 1147–1163.

Cai, Y., Rioux, M., Kelemen, P.B., Goldstein, S.L., Bolge, L., and Kylander-Clark, A.R.C., 2015, Distinctly different parental magmas for calc-alkaline plutons and tholeiitic lavas in the central and eastern Aleutian arc: Earth and Planetary Science Letters, v. 431, p. 119–126.

Castillo, P.R., 2012, Adakite petrogenesis: Lithos, v. 134–135, p. 304–316.

Coats, R.R., 1959, Geologic reconnaissance of Gareloi Island, Aleutian Islands, Alaska: U.S. Geological Survey Alaska: U.S. Geological Survey Bulletin 1028-J, p. 249–256.

Coats, R.R., Nelson, W.H., Lewis, R.Q., and Powers, H.A., 1961, Geologic reconnaissance of Kiska Island, Aleutian Islands, Alaska: U.S. Govt. Print. Off., U.S. Geological Survey Bulletin 1028-R 1028-R, p. 563–581.

Conrad, W.K., and Kay, R.W., 1984, Ultramafic and Mafic Inclusions from Adak Island: Crystallization History, and Implications for the Nature of Primary Magmas and Crustal Evolution in the Aleutian Arc: Journal of Petrology, v. 25, p. 88–125.

Coombs, M.L., Larsen, J.F., and Neal, C.A., 2018, Postglacial eruptive history and geochemistry of Semisopochnoi volcano, western Aleutian Islands, Alaska: U.S. Geological Survey Scientific Investigations Report USGS Numbered Series 2017–5150, 40 p.

Coombs, M.L., McGimsey, R.G., and Browne, B.L., 2012, Geologic map of Mount Gareloi, Gareloi Island, Alaska: U.S. Geological Survey Scientific Investigations Map USGS Numbered Series 3145.

Coombs, M.L., McGimsey, R.G., and Browne, B.L., 2008, Preliminary Volcano-Hazard Assessment for Gareloi Volcano, Gareloi Island, Alaska: U.S. Geological Survey Scientific Investigations Report USGS Numbered Series 2008–5159.

Couch, S., Sparks, R.S.J., and Carroll, M.R., 2001, Mineral disequilibrium in lavas explained by convective self-mixing in open magma chambers: Nature, v. 411, p. 1037–1039.

Cox, K.G., Bell, J.D., and Pankhurst, R.J., 1979, The interpretation of igneous rocks: London ; Boston, G. Allen & Unwin, 450 p.

Crabtree, S.M., and Lange, R.A., 2011, Complex Phenocryst Textures and Zoning Patterns in Andesites and Dacites: Evidence of Degassing-Induced Rapid Crystallization? Journal of Petrology, v. 52, p. 3–38.

Crawford, A., Falloon, T., and Eggins, S., 1987, The origin of island arc high-alumina basalts:

Contributions to Mineralogy and Petrology, v. 97, p. 417–430.

Daly, R.A., 1925, The Geology of Ascension Island: Proceedings of the American Academy of Arts and Sciences, v. 60, p. 3–80.

Davidson, J.P., 2013, Deciphering Mantle and Crustal Signatures in Subduction Zone Magmatism, *in* Bebout, G.E., Scholl, D.W., Kirby, S.H., and Platt, J.P. eds., Geophysical Monograph Series, Washington, D. C., American Geophysical Union, p. 251–262.

Davidson, J.P., Hora, J.M., Garrison, J.M., and Dungan, M.A., 2005, Crustal forensics in arc magmas: Journal of Volcanology and Geothermal Research, v. 140, p. 157–170.

Davidson, J., Turner, S., Handley, H., Macpherson, C., and Dosseto, A., 2007, Amphibole "sponge" in arc crust? Geology, v. 35, p. 787.

Davidson, J., Turner, S., and Plank, T., 2013, Dy/Dy*: Variations Arising from Mantle Sources and Petrogenetic Processes: Journal of Petrology, v. 54, p. 525–537.

Davidson, J., and Wilson, M., 2011, Differentiation and Source Processes at Mt Pelée and the Quill; Active Volcanoes in the Lesser Antilles Arc: Journal of Petrology, v. 52, p. 1493–1531.

DeBari, S.M., and Coleman, R.G., 1989, Examination of the deep levels of an island arc: Evidence from the Tonsina Ultramafic-Mafic Assemblage, Tonsina, Alaska: Journal of Geophysical Research: Solid Earth, v. 94, p. 4373–4391.

Defant, M.J., and Drummond, M.S., 1990, Derivation of some modern arc magmas by melting of young subducted lithosphere: Nature, v. 347, p. 662–665.

Delong, S.E., Perfit, M.R., McCulloch, M.T., and Ach, J., 1985, Magmatic Evolution of Semisopochnoi Island, Alaska: Trace-Element and Isotopic Constraints: The Journal of Geology, v. 93, p. 609–618.

Duncan, R., and Keller, R., 2004, Radiometric ages for basement rocks from the Emperor Seamounts, ODP Leg 197: Geochem. Geophys. Geosyst., v. 5.

Elliott, T., Plank, T., Zindler, A., White, W., and Bourdon, B., 1997, Element transport from slab to volcanic front at the Mariana arc: Journal of Geophysical Research: Solid Earth, v. 102, p. 14991–15019.

Fischer, T.P., Lopez, T.M., Aiuppa, A., Rizzo, A.L., Ilanko, T., Kelley, K.A., and Cottrell, E., 2021, Gas Emissions From the Western Aleutians Volcanic Arc: Frontiers in Earth Science, v. 9.

Fournelle, J.H., Marsh, B.D., and Myers, J.D., 1994, Age, character, and significance of Aleutian arc volcanism, *in* Plafker, G. and Berg, H.C. eds., The Geology of Alaska, Boulder, Colorado, Geological Society of America, p. 723–757.

Geist, E.L., Childs, J.R., and Scholl, D.W., 1988, The origin of summit basins of the Aleutian Ridge: Implications for block rotation of an arc massif: Tectonics, v. 7, p. 327–341.

George, R., Turner, S., Hawkesworth, C., Morris, J., Nye, C., Ryan, J., and Zheng, S.-H., 2003, Melting processes and fluid and sediment transport rates along the Alaska-Aleutian arc from an integrated U-Th-Ra-Be isotope study: Variations along the Alaska-Aleutian Arc: Journal of Geophysical Research: Solid Earth, v. 108.

Ghiorso, M., and Gualda, G., 2015, An H_2O–CO_2 mixed fluid saturation model compatible with rhyolite-MELTS: Contributions to Mineralogy and Petrology, v. 169.

Gill, J.B., 1981, Orogenic Andesites and Plate Tectonics: Berlin, Heidelberg, Springer Berlin Heidelberg, Minerals and Rocks, v. 16.

Greene, A., DeBari, S., Kelemen, P., Blusztajn, J., and Clift, P., 2006, A Detailed Geochemical Study of Island Arc Crust: the Talkeetna Arc Section, South-Central Alaska: Journal of Petrology, v. 47.

Grove, T.L., and Baker, M.B., 1984, Phase equilibrium controls on the tholeiitic versus calc-alkaline differentiation trends: Journal of Geophysical Research, v. 89, p. 3253–3274.

Grove, T.L., Elkins-Tanton, L.T., Parman, S.W., Chatterjee, N., Muntener, O., and Gaetani,

G.A., 2003, Fractional crystallization and mantle-melting controls on calc-alkaline differentiation trends: Contributions to Mineralogy and Petrology, v. 145, p. 515–533.

Gualda, G., Ghiorso, M., RV, L., and Carley, T., 2012, Rhyolite-MELTS: a Modified Calibration of MELTS Optimized for Silica-rich, Fluid-bearing Magmatic Systems: Journal of Petrology, v. 53, p. 875–890.

Gust, D.A., and Perfit, M.R., 1987, Phase relations of a high-Mg basalt from the Aleutian Island Arc: Implications for primary island arc basalts and high-Al basalts: Contributions to Mineralogy and Petrology, v. 97, p. 7–18.

Hawkesworth, C., Turner, S., McDermott, F., Peate, D., and Calsteren, P., 1997, U-Th Isotopes in Arc Magmas: Implications for Element Transfer from the Subducted Crust: Science (New York, N.Y.), v. 276, p. 551–5.

Hildreth, W., and Moorbath, S., 1988, Crustal contributions to arc magmatism in the Andes of Central Chile: Contributions to Mineralogy and Petrology, v. 98, p. 455–489.

Holbrook, W.S., Lizarralde, D., McGeary, S., Bangs, N., and Diebold, J., 1999, Structure and composition of the Aleutian island arc and implications for continental crustal growth: Geology, v. 27, p. 31–34.

House, L.S., and Jacob, K.H., 1983, Earthquakes, plate subduction, and stress reversals in the Eastern Aleutian Arc: Journal of Geophysical Research: Solid Earth, v. 88, p. 9347–9373.

Iddings, J.P., 1892, The Origin of Igneous Rocks: Philosophical Society, 140 p.

Irvine, T.N., and Baragar, W.R.A., 1971, A Guide to the Chemical Classification of the Common Volcanic Rocks: Canadian Journal of Earth Sciences, v. 8, p. 523–548.

Janiszewski, H., Abers, G., Shillington, D., and Calkins, J., 2013, Crustal structure along the Aleutian island arc: New insights from receiver functions constrained by active-source data: Geochemistry Geophysics Geosystems, v. 14, p. 2977–2992.

Jerram, D.A., and Davidson, J.P., 2007, Frontiers in Textural and Microgeochemical Analysis:

Elements, v. 3, p. 235–238.

Jicha, B.R., and Kay, S.M., 2018, Quantifying arc migration and the role of forearc subduction erosion in the central Aleutians: Journal of Volcanology and Geothermal Research, v. 360, p. 84–99.

Jicha, B.R., Scholl, D.W., Singer, B.S., Yogodzinski, G.M., and Kay, S.M., 2006, Revised age of Aleutian Island Arc formation implies high rate of magma production: Geology, v. 34, p. 661.

Kay, R.W., 1978, Aleutian magnesian andesites: Melts from subducted Pacific ocean crust: Journal of Volcanology and Geothermal Research, v. 4, p. 117–132.

Kay, R.W., 1980, Volcanic Arc Magmas: Implications of a Melting-Mixing Model for Element Recycling in the Crust-Upper Mantle System: The Journal of Geology, v. 88, p. 497–522.

Kay, S.M., Jicha, B.R., Citron, G.L., Kay, R.W., Tibbetts, A.K., and Rivera, T.A., 2019, The Calc-Alkaline Hidden Bay and Kagalaska Plutons and the Construction of the Central Aleutian Oceanic Arc Crust: Journal of Petrology, v. 60, p. 393–439.

Kay, S.M., and Kay, R.W., 1994a, Aleutian magmas in space and time, *in* Plafker, G. and Berg, H.C. eds., The Geology of Alaska, Boulder, Colorado, Geological Society of America, p. 687–717.

Kay, S.M., and Kay, R.W., 1994b, Aleutian magmatism in space and time, *in* v. 1, p. 687–722.

Kay, S.M., and Kay, R.W., 1985, Aleutian tholeiitic and calc-alkaline magma series I: The mafic phenocrysts: Contributions to Mineralogy and Petrology, v. 90, p. 276–290

Kay, S.M., Kay, R.W., and Citron, G.P., 1982, Tectonic controls on tholeiitic and calc-alkaline magmatism in the Aleutian Arc: Journal of Geophysical Research, v. 87, p. 4051.

Kay, S.M., Kay, R.W., Citron, G.P., and Perfit, M.R., 1990, Calc-alkaline plutonism in the intra-oceanic Aleutian arc, Alaska, *in* Geological Society of America Special Papers, Geological Society of America, v. 241, p. 233–256.

Kelemen, P.B., Yogodzinski, G.M., and Scholl, D.W., 2003a, Along-strike variation in the Aleutian Island Arc: Genesis of high Mg# andesite and implications for continental crust, *in* Eiler, J. ed., Geophysical Monograph Series, Washington, D. C., American Geophysical Union, v. 138, p. 223–276.

Kelemen, P.B., Hanghøj, K., and Greene, A.R., 2003b, One View of the Geochemistry of Subduction-related Magmatic Arcs, with an Emphasis on Primitive Andesite and Lower Crust: Treatise on Geochemistry, v. 3, p. 659.

Kincaid, C., and Sacks, I., 1997, Thermal and dynamical evolution of the upper mantle in subduction zones: Journal of Geophysical Research, v. 1021, p. 12295–12316.

Kushiro, I., 2001, Partial Melting Experiments on Peridotite and Origin of Mid-Ocean Ridge Basalt: Annual Review of Earth and Planetary Sciences, v. 29, p. 71–107.

Larsen, J.F., 2016, Unraveling the diversity in arc volcanic eruption styles: Examples from the Aleutian volcanic arc, Alaska: Journal of Volcanology and Geothermal Research, v. 327, p. 643–668.

Larsen, J.F., Nye, C.J., Coombs, M., Tilman, M., Izbekov, P., and Cameron, C., 2010, Petrology and geochemistry of the 2006 eruption of Augustine Volcano: The 2006 Eruption of Augustine Volcano, Alaska, v. 1769.

Larsen, J.F., Schaefer, J., Vallance, J.W., and Neill, O.K., 2020, Petrology and geochemistry of three Early Holocene eruptions from Makushin Volcano, Alaska: Bulletin of Volcanology, v. 82, p. 72.

Le Maitre, R.W., 1982, Numerical petrology: statistical interpretation of geochemical data: Amsterdam ; New York, Elsevier Scientific Pub. Co, Developments in petrology 8, 281 p.

Le Maitre, R.W., Streckeisen, A., Zanettin, B., Le Bas, M.J., Bonin, B., and Bateman, P. (Eds.), 2002, Igneous Rocks: A Classification and Glossary of Terms: Recommendations of the

International Union of Geological Sciences Subcommission on the Systematics of Igneous Rocks: Cambridge, Cambridge University Press

Lee, C.-T.A., and Bachmann, O., 2014, How important is the role of crystal fractionation in making intermediate magmas? Insights from Zr and P systematics: Earth and Planetary Science Letters, v. 393, p. 266–274.

Loewen, M.W., Izbekov, P., Moshrefzadeh, J., Coombs, M., Larsen, J., Graham, N., Harbin, M., Waythomas, C., and Wallace, K., 2019, Petrology of the 2016–2017 eruption of Bogoslof Island, Alaska: Bulletin of Volcanology, v. 81, p. 72.

Mackey, K.G., Fujita, K., Gunbina, L.V., Kovalev, V.N., Imaev, V.S., Koz'min, B.M., and Imaeva, L.P., 1997, Seismicity of the Bering Strait region: Evidence for a Bering block: Geology, v. 25, p. 979–982.

Marlow, M.S., Scholl, D.W., Buffington, E., and Rho, T.R., 1973, Tectonic History of the Central Aleutian Arc: GSA Bulletin, v. 84, p. 1555–1574.

McCulloch, M.T., and Perfit, M.R., 1981, 143Nd/144Nd,87Sr/86Sr and trace element constraints on the petrogenesis of Aleutian island arc magmas: Earth and Planetary Science Letters, v. 56, p. 167–179.

Miller, D., Langmuir, C., Goldstein, S., and Franks, A., 1992, The Importance of Parental Magma Composition to Calc-Alkaline and Tholeiitic Evolution: Evidence From Umnak Island in the Aleutians: Journal of Geophysical Research, v. 97, p. 321–343.

Miller, T.P., McGimsey, R.G., Richter, D.H., Riehle, J.R., Nye, C.J., Yount, M.E., and Dumoulin, J.A., 1998, Catalog of the historically active volcanoes of Alaska: U.S. Geological Survey Open-File Report 98-582, 104 p.

Miyashiro, A., 1974, Volcanic rock series in island arcs and active continental margins: American Journal of Science, v. 274, p. 321–355.

Morris, J.D., and Hart, S.R., 1983, Isotopic and incompatible element constraints on the genesis

of island arc volcanics from Cold Bay and Amak Island, Aleutians, and implications for mantle structure: Geochimica et Cosmochimica Acta, v. 47, p. 2015–2030.

Müntener, O., Kelemen, P.B., and Grove, T.L., 2001, The role of H_2O during crystallization of primitive arc magmas under uppermost mantle conditions and genesis of igneous pyroxenites: an experimental study: Contributions to Mineralogy and Petrology, v. 141, p. 643–658.

Myers, J., Marsh, B., and Sinha, A., 1985, Strontium isotopic and selected trace element variations between two Aleutian volcanic centers (Adak and Atka): implications for the development of arc volcanic plumbing systems: Contributions to Mineralogy and Petrology, v. 91, p. 221–234.

Nandedkar, R.H., Ulmer, P., and Müntener, O., 2014, Fractional crystallization of primitive, hydrous arc magmas: an experimental study at 0.7 GPa: Contributions to Mineralogy and Petrology, v. 167, p. 1015.

Nelson, S.T., and Montana, A., 1992, Sieve-textured plagioclase in volcanic rocks produced by rapid decompression: American Mineralogist, v. 77, p. 1242–1249.

Nielsen, S.G., Yogodzinski, G., Prytulak, J., Plank, T., Kay, S.M., Kay, R.W., Blusztajn, J., Owens, J.D., Auro, M., and Kading, T., 2016, Tracking along-arc sediment inputs to the Aleutian arc using thallium isotopes: Geochimica et Cosmochimica Acta, v. 181, p. 217–237.

Nye, C.J., Begét, J.E., Layer, P.W., Mangan, M.T., McConnell, V.S., McGimsey, R.G., Miller, T.P., Moore, R.B., and Stelling, P.L., 2018, Geochemistry of some quaternary lavas from the Aleutian Arc and Mt. Wrangell: Alaska Division of Geological & Geophysical Surveys RDF 2018-1, RDF 2018-1 p.

Perfit, M., Brueckner, H., Lawrence, J., and Kay, R., 1980, Trace element and isotopic variations in a zoned pluton and associated volcanic rocks, Unalaska Island, Alaska: A model for

fractionation in the Aleutian calcalkaline suite: Contributions to Mineralogy and Petrology, v. 73, p. 69–87.

Pistone, M., Blundy, J.D., and Brooker, R.A., 2016, Textural and chemical consequences of interaction between hydrous mafic and felsic magmas: an experimental study: Contributions to Mineralogy and Petrology, v. 171, p. 8.

Price, R.C., Gamble, J.A., Smith, I.E.M., Maas, R., Waight, T., Stewart, R.B., and Woodhead, J., 2012, The Anatomy of an Andesite Volcano: a Time–Stratigraphic Study of Andesite Petrogenesis and Crustal Evolution at Ruapehu Volcano, New Zealand: Journal of Petrology, v. 53, p. 2139–2189.

Putirka, K.D., 2008, Thermometers and Barometers for Volcanic Systems: Reviews in Mineralogy and Geochemistry, v. 69, p. 61–120.

Rader, E., Kobs Nawotniak, S., and Heldmann, J., 2018, Variability of Spatter Morphology in Pyroclastic Deposits in Southern Idaho, as Correlated to Thermal Conditions and Eruptive Environment: Earth and Space Science, v. 5, p. 592–603.

Rader, E.L., and Larsen, J.F., 2013, Experimental phase relations of a low MgO Aleutian basaltic andesite at $XH_2O = 0.7–1$: Contributions to Mineralogy and Petrology, v. 166, p. 1593–1611.

Rapp, R.P., and Watson, E.B., 1995, Dehydration Melting of Metabasalt at 8–32 kbar: Implications for Continental Growth and Crust-Mantle Recycling: Journal of Petrology, v. 36, p. 891–931.

Roeder, P.L., and Emslie, R.F., 1970, Olivine-liquid equilibrium: Contributions to Mineralogy and Petrology, v. 29, p. 275–289.

Rollinson, H., and Pease, V., 2021, Using Geochemical Data: To Understand Geological Processes: Cambridge, Cambridge University Press.

Romick, J.D., Kay, S.M., and Kay, R.W., 1992, The influence of amphibole fractionation on the

evolution of calc-alkaline andesite and dacite tephra from the central Aleutians, Alaska: Contributions to Mineralogy and Petrology, v. 112, p. 101–118.

Scarfe, C.M., and Fujii, T., 1987, Petrology of crystal clots in the pumice of Mount St. Helens' March 19, 1982 eruption; significant role of Fe-Ti oxide crystallization: Journal of Volcanology and Geothermal Research, v. 34, p. 1–14.

Scholl, D.W., 2007, Viewing the tectonic evolution of the Kamchatka-Aleutian (KAT) connection with an Alaska crustal extrusion perspective: Washington DC American Geophysical Union Geophysical Monograph Series, v. 172, p. 3–35.

Scholl, D.W., Vallier, T.L., and Stevenson, A.J., 1987, Geologic Evolution and Petroleum Geology of the Aleutian Ridge: Circum Pacific Council Publications,.

Shillington, D.J., Van Avendonk, H.J.A., Holbrook, W.S., Kelemen, P.B., and Hornbach, M.J., 2004, Composition and structure of the central Aleutian island arc from arc-parallel wide-angle seismic data: Composition Structure Aleutian Arc: Geochemistry, Geophysics, Geosystems, v. 5.

Singer, B.S., and Myers, J.D., 1990, Intra-arc extension and magmatic evolution in the central Aleutian arc, Alaska: Geology, v. 18, p. 1050.

Sisson, T.W., and Grove, T.L., 1993, Temperatures and H_2O contents of low-MgO high-alumina basalts: Contributions to Mineralogy and Petrology, v. 113, p. 167–184.

Sisson, T.W., Ratajeski, K., Hankins, W., and Glazner, A., 2005, Voluminous granitic magmas from common basaltic sources: Contributions to Mineralogy and Petrology, v. 148, p. 635–661.

Syracuse, E.M., and Abers, G.A., 2006, Global compilation of variations in slab depth beneath arc volcanoes and implications: Arc Volcano Slab Depth: Geochemistry, Geophysics, Geosystems, v. 7.

Vernon, R.H., 2018, A Practical Guide to Rock Microstructure: Cambridge, Cambridge

University Press.

Waters, L.E., Cottrell, E., Coombs, M.L., and Kelley, K.A., 2021, Generation of Calc-Alkaline Magmas during Crystallization at High Oxygen Fugacity: An Experimental and Petrologic Study of Tephras from Buldir Volcano, Western Aleutian Arc, Alaska, USA: Journal of Petrology, v. 62.

Waters, L.E., and Lange, R.A., 2015, An updated calibration of the plagioclase-liquid hygrometer-thermometer applicable to basalts through rhyolites: American Mineralogist, v. 100, p. 2172–2184.

Wieser, P., Petrelli, M., Lubbers, J., Wieser, E., Kent, A., and Till, C., 2021, Thermobar: A Critical Evaluation of Mineral-melt Thermobarometry and Hygrometry in Arc Magmas Using a New Open-source Python 3 Tool, *in* p. 367080.

Wilson, M., 1989, Igneous petrogenesis: London, Unwin Hyman, 466 p.

Winter, J.D., 2001, An introduction to igneous and metamorphic petrology: Upper Saddle River, NJ, Prentice Hall, 697 p.

Yogodzinski, G.M., Brown, S.T., Kelemen, P.B., Vervoort, J.D., Portnyagin, M., Sims, K.W.W., Hoernle, K., Jicha, B.R., and Werner, R., 2015, The Role of Subducted Basalt in the Source of Island Arc Magmas: Evidence from Seafloor Lavas of the Western Aleutians: Journal of Petrology, v. 56, p. 441–492.

Yogodzinski, G.M., Kay, R.W., Volynets, O.N., Koloskov, A.V., and Kay, S.M., 1995, Magnesian andesite in the western Aleutian Komandorsky region: Implications for slab melting and processes in the mantle wedge: Geological Society of America Bulletin, v. 107, p. 505–519.

Yogodzinski, G.M., Kelemen, P.B., Hoernle, K., Brown, S.T., Bindeman, I., Vervoort, J.D., Sims, K.W.W., Portnyagin, M., and Werner, R., 2017, Sr and O isotopes in western Aleutian seafloor lavas: Implications for the source of fluids and trace element character

of arc volcanic rocks: Earth and Planetary Science Letters, v. 475, p. 169–180.

Yogodzinski, G.M., Lees, J.M., Churikova, T.G., Dorendorf, F., Wöerner, G., and Volynets, O.N., 2001, Geochemical evidence for the melting of subducting oceanic lithosphere at plate edges: Nature, v. 409, p. 500–504.

Yogodzinski, G.M., Vervoort, J.D., Brown, S.T., and Gerseny, M., 2010, Subduction controls of Hf and Nd isotopes in lavas of the Aleutian island arc: Earth and Planetary Science Letters, v. 300, p. 226–238.

Yogodzinski, G.M., Volynets, O.N., Koloskov, A.V., Seliverstov, N.I., and Matvenkov, V.V., 1994, Magnesian Andesites and the Subduction Component in a Strongly Calc-Alkaline Series at Piip Volcano, Far Western Aleutians: Journal of Petrology, v. 35, p. 163–204.

Zellmer, G.F., Pistone, M., Iizuka, Y., Andrews, B.J., Gómez-Tuena, A., Straub, S.M., and Cottrell, E., 2016, Petrogenesis of antecryst-bearing arc basalts from the Trans-Mexican Volcanic Belt: Insights into along-arc variations in magma-mush ponding depths, H_2O contents, and surface heat flux: American Mineralogist, v. 101, p. 2405–2422.

Zimmer, M.M., Plank, T., Hauri, E.H., Yogodzinski, G.M., Stelling, P., Larsen, J., Singer, B., Jicha, B., Mandeville, C., and Nye, C.J., 2010, The Role of Water in Generating the Calc-alkaline Trend: New Volatile Data for Aleutian Magmas and a New Tholeiitic Index: Journal of Petrology, v. 51, p. 2411–2444.

Table 1: Sample rock type, location, and modal mineralogy

	Kiska						Gareloi
Sample	15KKMP005-1A	15KKMP005-02	15KKMP005-03	15KKMP005-04	15KKMP006-01	15KKKS001-1	G-05
Rock type	Tephra	Spatter	Spatter	Spatter	Spatter	Hyaloclastite	Lava Flow
Lat. (N)	52.0	52.1	52.1	52.1	52.1	52.0	51.8
Long. (E)	177.5	177.6	177.6	177.6	177.6	177.5	178.8
Modal Abundances (in percent)							
plag	29.1	22.1	26.2	29.3	31.7	28.1	21.4
opx	4.1	6.5	6.7	8.9	2.8	—	—
cpx	2.8	5.8	5.0	8.3	4.6	2.4	1.7
ol	—	—	—	—	—	—	0.8
ox	1.3	2.6	1.5	2.8	0.8	1.1	0.5
gmass	62.7	63.0	60.6	50.7	60.2	68.4	75.6
vesicles	16.9	15.5	28.5	46.0	21.7	—	3.7

Plag, plagioclase; opx, orthopyroxene; cpx, clinopyroxene; ol, olivine; ox, oxides; gmass, groundmass

Table 2: Representative pyroxene and olivine analyses from Kiska and Gareloi volcanoes

Clinopyroxene

	Kiska		Gareloi		
Sample:	15KKMP005-02	15KKMP006-01	G-01	G-02	G-03
SiO_2	52.13	52.70	51.13	47.90	48.22
TiO_2	0.52	0.42	0.76	1.65	1.34
Al_2O_3	2.04	1.61	2.42	5.30	4.55
Cr2O3	0.01	0.02	—	—	—
FeO*	9.65	9.40	10.06	9.93	10.38
MnO	0.37	0.44	0.37	0.29	0.33
MgO	14.89	15.00	14.55	13.10	13.42
CaO	20.67	20.88	19.94	20.36	19.56
Na_2O	0.31	0.27	0.34	0.41	0.35
Total	100.59	100.76	99.61	98.94	98.15

Orthopyroxene

SiO_2	53.48	52.65	—	—	—
TiO_2	0.24	0.32	—	—	—
Al_2O_3	0.92	2.81	—	—	—
Cr2O3	0.01	0.02	—	—	—
FeO*	19.26	17.26	—	—	—
MnO	0.73	0.51	—	—	—
MgO	24.16	25.23	—	—	—
CaO	1.45	1.69	—	—	—
Na_2O	0.01	0.03	—	—	—
Total	100.26	100.51	—	—	—

Olivine

	Kiska		Gareloi		
Sample:	15KKMP005-02	15KKMP006-01	G-01	G-02	G-03
SiO_2	—	—	37.23	37.82	36.29
TiO_2	—	—	0.05	0.06	0.10
Al_2O_3	—	—	0.02	0.06	0.05
Cr2O3	—	—	—	0.01	0.02
NiO	—	—	0.03	0.01	0.05
FeO*	—	—	25.64	21.12	30.62
MnO	—	—	0.57	0.80	0.76
MgO	—	—	34.78	38.02	30.39
CaO	—	—	0.30	0.19	0.20
Na_2O	—	—	—	0.01	—
Total	—	—	98.61	98.10	98.48

*Total Fe given as FeO.

Table 3: Representative plagioclase and oxide analyses from Kiska and Gareloi volcanoes

Plagioclase					
	Kiska		Gareloi		
Sample:	15KKMP005-02	15KKMP006-01	G-01	G-02	G-03
SiO_2	51.17	51.23	50.11	54.56	54.57
Al_2O_3	31.16	31.24	29.95	28.27	28.39
FeO*	0.72	0.06	1.66	0.99	0.88
MgO	0.08	0.06	0.36	0.11	0.10
CaO	14.01	13.84	13.70	11.04	10.95
Na_2O	3.62	3.69	3.33	4.68	4.87
K_2O	0.19	0.17	0.41	0.52	0.46
Total	100.95	100.93	99.52	100.17	100.23
Oxides					
SiO_2	0.12	0.10	0.13	0.10	0.18
TiO_2	10.91	10.73	10.61	9.51	10.20
Al_2O_3	2.95	3.25	4.83	3.40	3.21
Cr2O3	0.06	0.06	0.13	0.05	0.05
FeO*	80.92	80.34	78.36	78.89	80.33
MnO	0.50	0.44	0.40	0.14	0.50
MgO	2.75	2.82	3.94	1.70	2.20
CaO	0.01	0.02	0.03	0.10	0.14
Na_2O	0.00	0.01	0.00	0.02	0.01
Total	98.21	97.78	98.43	93.91	96.82

*Total Fe given as FeO.

Table 4: Whole-rock major and trace element data from Kiska and Gareloi volcanoes

	Kiska							Gareloi
Sample:	15KKKS001-1	15KKMP005-1A	15KKMP005-02	15KKMP005-03	15KKMP005-04	15KKMP006-01	15KKMP007-01	G-04
Rock type:	Hyaloclastite	Bomb (Tephra)	Spatter	Spatter	Spatter	Spatter	Lava Flow	Lava Flow
SiO_2	52.50	56.94	56.65	57.07	57.04	56.87	56.51	53.24
TiO_2	0.82	0.79	0.78	0.77	0.77	0.79	0.88	1.08
Al_2O_3	18.80	17.88	17.75	18.01	17.95	18.06	17.03	18.29
FeO*	8.62	7.59	7.65	7.41	7.43	7.48	7.99	8.51
MnO	0.16	0.16	0.16	0.16	0.16	0.15	0.16	0.19
MgO	4.17	3.62	3.64	3.54	3.55	3.41	3.90	2.70
CaO	8.77	7.66	7.63	7.73	7.67	7.61	7.21	5.80
Na_2O	3.24	3.42	3.33	3.44	3.45	3.43	3.29	4.21
K_2O	0.78	1.40	1.41	1.41	1.41	1.41	1.38	2.53
P_2O_5	0.18	0.17	0.17	0.17	0.17	0.17	0.15	0.46
LOI %	1.67	0.21	0.48	0.08	0.06	0.43	1.14	2.76
La	8.55	10.48	10.28	10.44	10.58	10.59	10.14	19.40
Ce	19.74	23.80	23.64	23.87	24.13	24.32	23.63	47.50
Pr	3.16	3.39	3.38	3.42	3.46	3.45	3.37	5.97
Nd	14.90	15.06	15.13	15.16	15.23	15.37	15.21	25.33
Sm	3.88	3.82	3.77	3.83	3.82	3.79	3.79	5.72
Eu	1.22	1.08	1.12	1.15	1.15	1.13	1.11	1.48
Gd	4.22	3.79	3.90	3.84	3.90	3.80	3.98	5.17
Tb	0.70	0.64	0.64	0.65	0.65	0.64	0.67	0.80
Dy	4.10	3.93	3.97	3.96	3.89	3.95	4.09	4.61
Ho	0.88	0.85	0.84	0.84	0.84	0.82	0.88	0.95
Er	2.51	2.42	2.42	2.40	2.43	2.39	2.48	2.65
Tm	0.38	0.38	0.38	0.38	0.38	0.38	0.40	0.42
Yb	2.45	2.42	2.47	2.47	2.42	2.44	2.57	2.68
Lu	0.39	0.40	0.40	0.39	0.39	0.39	0.41	0.42
Y	25.09	23.53	23.58	23.46	23.47	23.20	23.61	25.40

Table 4: Continued

Rb	9.07	27.93	27.58	28.53	28.22	27.71	27.46	70.47
Sr	561.23	351.67	349.00	361.67	360.82	363.05	323.35	478.10
Pb	4.64	4.89	4.01	4.37	5.43	5.82	7.06	15.43
Ba	235.36	383.55	381.03	391.49	392.06	390.67	372.17	897.47
Cs	0.54	1.29	1.33	1.38	1.34	1.30	1.30	4.62
U	0.41	1.14	1.15	1.16	1.17	1.15	1.12	3.11
Th	0.86	2.55	2.58	2.61	2.61	2.63	2.60	6.95
Zr	88.82	122.18	122.93	125.04	124.03	122.46	128.39	206.14
Hf	2.43	3.47	3.43	3.48	3.44	3.37	3.54	5.70
Ta	0.14	0.20	0.19	0.20	0.19	0.19	0.21	0.39
Nb	2.27	2.77	2.77	2.78	2.78	2.76	3.01	5.64
Sc	25.08	20.34	20.76	19.86	19.91	19.91	21.55	19.32
Cr	21.05	8.80	12.29	9.23	10.90	10.26	9.38	3.97
Ni	15.89	10.39	9.61	9.94	10.49	9.92	11.38	6.41

*Total Fe given as FeO.

Table 5: Average glass compositions used for geothermometry and hygrometry

	Kiska Glass	G-01 Glass	G-05 Glass
SiO_2	69.67 (2.89)	54.90 (0.51)	59.73 (1.62)
TiO_2	0.82 (0.16)	1.20 (0.04)	1.50 (0.29)
Al_2O_3	16.10 (1.61)	16.53 (0.29)	15.04 (1.61)
FeO*	2.66 (1.29)	9.98 (0.49)	8.72 (1.93)
MnO	—	0.21 (0.03)	0.22 (0.05)
MgO	0.76 (0.40)	3.15 (0.15)	1.24 (0.89)
CaO	3.36 (1.07)	6.09 (0.28)	3.01 (1.11)
Na_2O	3.99 (0.72)	3.99 (0.35)	4.56 (0.43)
K_2O	3.08 (0.77)	3.44 (0.24)	5.14 (0.63)
P_2O_5	0.24 (0.05)	0.50 (0.05)	0.84 (0.14)

*Total Fe given as FeO.
Values in parentheses are the standard deviation from the mean for each respective oxide.

Table 6: Representative analysis of high-Al basalts from the Aleutian Islands

Sample:	OK7	CHAG	GS727	ADG14	MOF15	MOFA7	KAN508	03GRGM40	51P54
SiO_2	50.60	51.04	49.68	48.62	49.35	52.40	47.66	52.10	51.74
TiO_2	1.10	0.98	0.85	0.99	0.86	0.98	1.18	0.93	0.89
Al_2O_3	18.06	21.12	19.39	18.71	18.57	20.43	18.58	18.44	19.93
FeO*	9.74	7.73	9.33	10.27	9.52	8.44	10.28	8.80	8.10
MnO	0.12	0.12	0.14	0.15	0.15	0.15	0.16	0.17	0.16
MgO	5.58	3.99	5.60	5.68	4.84	3.52	6.06	4.54	4.24
CaO	11.46	10.90	10.97	11.52	10.80	9.57	11.41	9.34	9.49
Na_2O	2.74	3.21	2.66	2.75	2.85	3.27	2.68	3.57	3.14
K_2O	0.53	0.59	0.82	1.05	1.11	1.39	0.87	1.76	0.86
P_2O_5	0.28	0.13	0.17	0.21	0.15	—	—	0.35	0.16
Total	100.21	99.81	99.44	99.95	98.20	100.15	98.88	100.01	98.71
Cr	72.00	27.00	49.00	41.00	18.00	8.00	35.00	7.47	30.00
Ni	9.00	16.00	22.00	18.00	8.00	14.00	18.00	12.39	30.00

Samples OK7, CHAG, GS727, ADG14, MOF15, MOFA7, and KAN508 are from Kay and Kay (1994) and references therein.
Samples 03GRGM40 and 51P54 are from Coombs et al. (2012) and Coats et al. (1961).

Figure 1. A map of the Aleutian arc as well as seismic data from Syracuse and Abers (2006). The area map was created using GeoMapApp (www.geomapap-p.org). A) The Aleutian arc spans from the Alaska Peninsula in the east to the Kamchatka Peninsula in the West (~4000 km). The colored circles and rectangles indicate the location of the active volcanoes within the distal Aleutians included in this study. This color scheme will be used throughout the entirety of this study. The white arrows indicate the approximate plate convergence direction from Yogodzinski et al. (2015). The white lines are the approximate location of the rotated crustal blocks described by Geist et al. (1988). B) The relative plate convergence velocity (km/Ma) and orthogonal convergence velocity (km/Ma) along-strike of the arc. C) The inferred dip (δ) of the subducted slab at each Aleutian volcanic center. D) The inferred depth (H) to the slab for each Aleutian volcanic center with an inset that shows the distance from the trench for the volcanoes in the arc that erupt alkalic lavas.

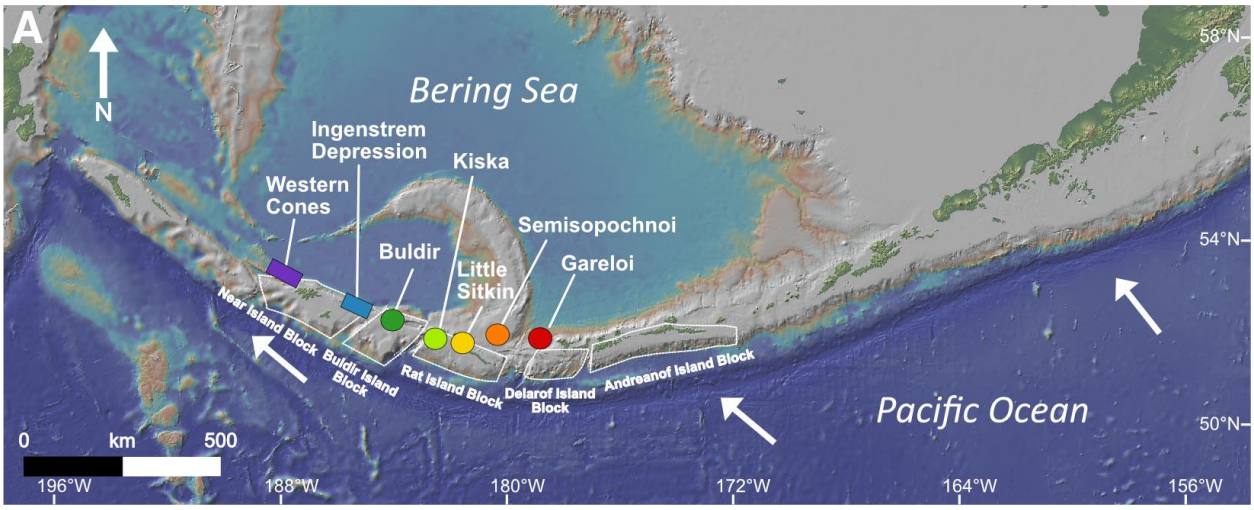
A
N
Bering Sea
Ingenstrem Depression
Kiska
Western Cones
Semisopochnoi
Buldir
Little Sitkin
Gareloi
Near Island Block
Buldir Island Block
Rat Island Block
Delarof Island Block
Andreanof Island Block
Pacific Ocean
0 km 500
196°W
188°W
180°W
172°W
164°W
156°W
58°N
54°N
50°N

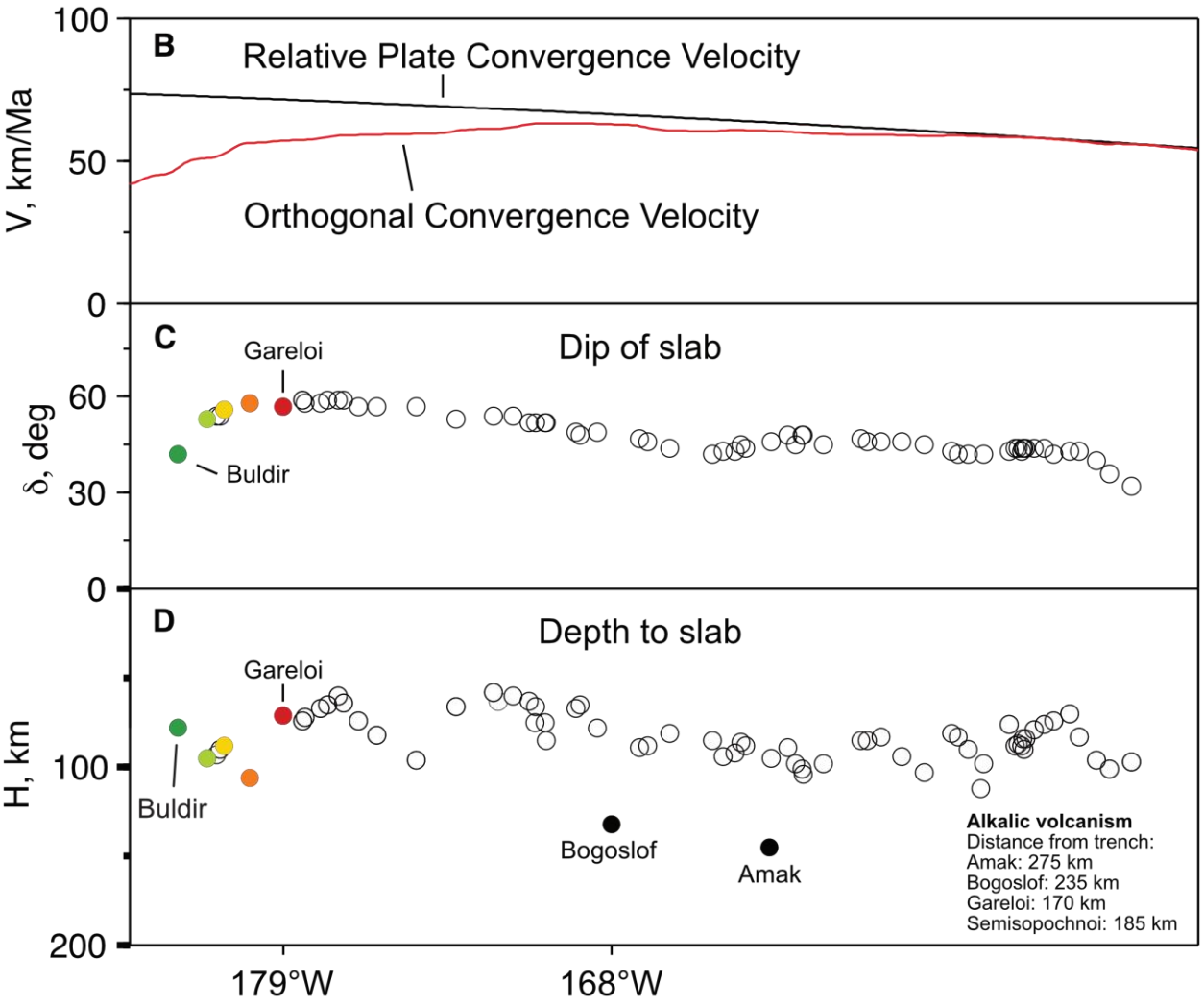
B
Relative Plate Convergence Velocity
Orthogonal Convergence Velocity
V, km/Ma
100
50
0
C
Dip of slab
Gareloi
Buldir
δ, deg
60
30
0
D
Depth to slab
Gareloi
Buldir
Bogoslof
Amak
H, km
100
200
179°W
168°W
Alkalic volcanism
Distance from trench:
Amak: 275 km
Bogoslof: 235 km
Gareloi: 170 km
Semisopochnoi: 185 km

Figure 2. Miyashiro (1974) discrimination diagram with tholeiitic and calc-alkaline delineated by heavy line. Other lines further divide samples into transitional tholeiitic (TTH) and transitional calc-alkaline (TCA) following Kay and Kay, (1985). Magmas become increasingly calc-alkaline westward along-strike of the distal portion of the arc. All geochemical data used in this study was queried from the Alaska Volcano Observatory database. Samples are from Coats (1953, 1959b); Snyder (1959); Coats et al. (1961); Delong (1974); McCulloch and Perfit (1981); White and Patchett (1984); Kay and Kay (1985); Delong et al. (1985); Brophy (1986); George et al. (2003); Singer et al. (2007); Yogodzinski et al. (2010, 2015); Coombs et al. (2012, 2018); Nye et al. (2018); Larsen et al. (2020); Waters et al. (2021). In this and all subsequent plots of major element oxides, weight percent (wt. %) concentrations are normalized to 100% on a volatile free basis, with all Fe as FeO.

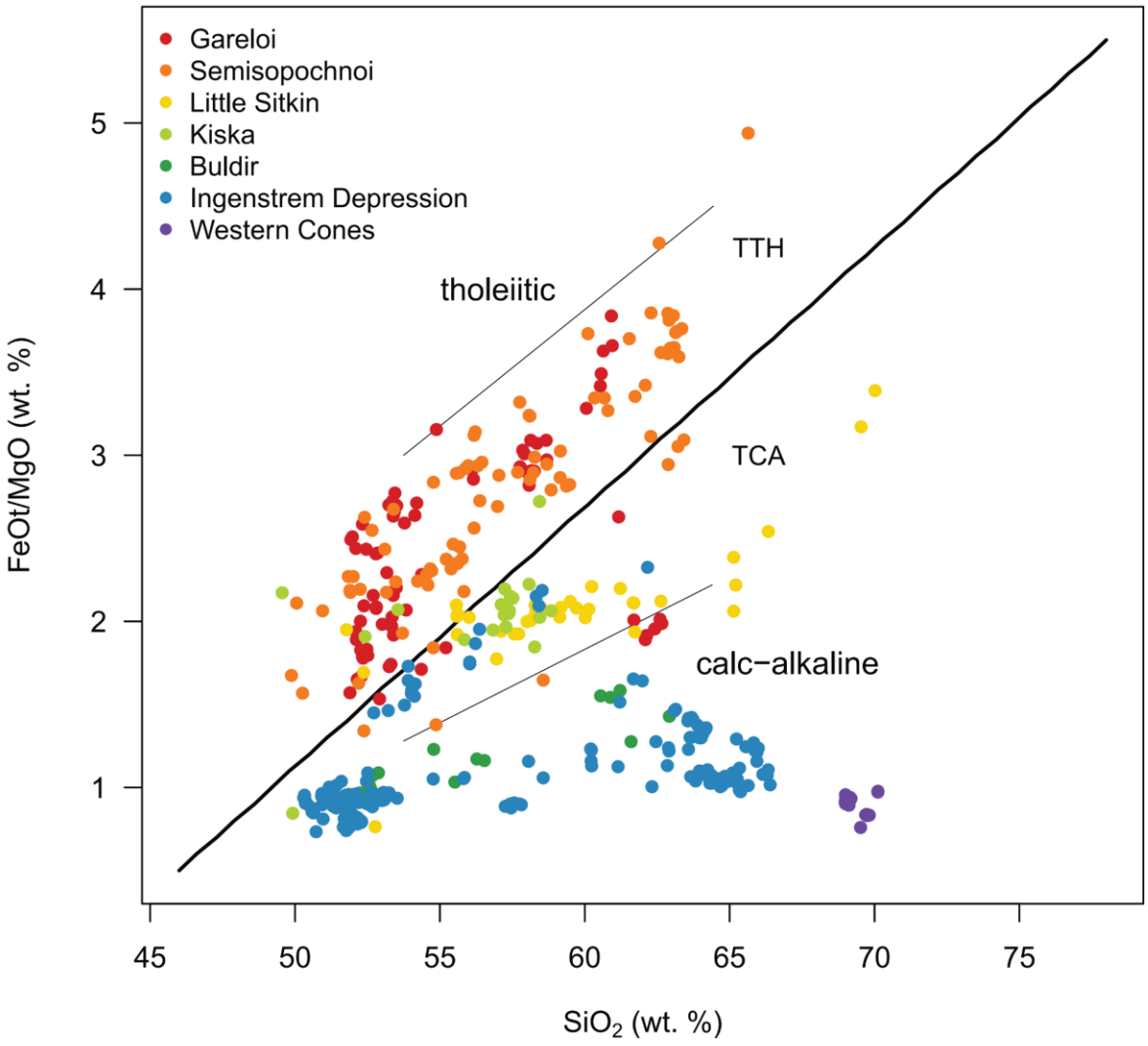
Gareloi
Semisopochnoi
Little Sitkin
Kiska
Buldir
Ingenstrem Depression
Western Cones
tholeiitic
TTH
TCA
calc−alkaline
FeOt/MgO (wt. %)
SiO2 (wt. %)
1
2
3
4
5
45
50
55
60
65
70
75

Figure 3. Lithological column and photographs from Greene et al., (2006) of the Talkeetna paleo-island arc section. A) Lithological column derived from field observations and geobarometry. B) Magma mingling features preserved in the Nelchina dike complex, adjacent to the Nelchina Glacier (sledgehammer is ~80 cm) C) Layered gabbronorite just west of Tazlina Lake, typical of exposures between Tazlina Lake and Barnette Creek. D) Magnetite gabbronorite prevalent in the lower crust (photomicrograph is ~8 mm across).

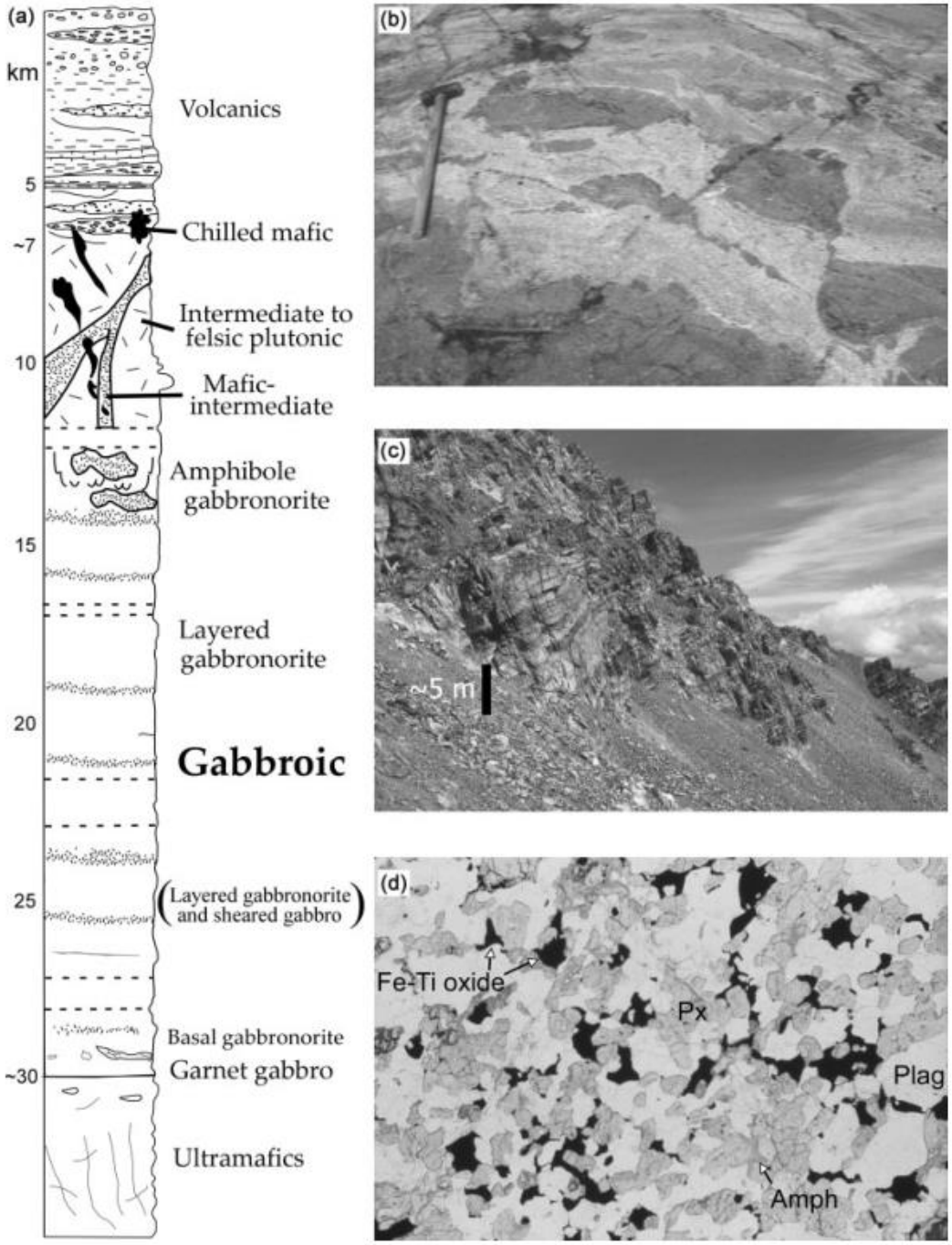
(a)
km
5
~7
10
15
20
25
~30
Volcanics
Chilled mafic
Intermediate to felsic plutonic
Mafic-intermediate
Amphibole gabbronorite
Layered gabbronorite
Gabbroic
(Layered gabbronorite and sheared gabbro)
Basal gabbronorite
Garnet gabbro
Ultramafics
(b)
(c)
~5 m
(d)
Fe-Ti oxide
Px
Plag
Amph

Figure 4. A) The active volcanoes within the distal Aleutians analyzed in this study. The area map was created using GeoMapApp (www.geomapap-p.org). From east to west the active volcanoes within the distal Aleutians are Gareloi, Semisopochnoi, Little Sitkin, Kiska, Buldir, ~134 submarine volcanic cones within the Ingenstrem Depression, and 5 submarine Western Cones. Note how particularly Buldir, Ingenstrem Depression, and Western Cones are on the northern margin of the arc ridge. B) Perspective drawing showing a torn Pacific plate subducting to the north beneath the central Aleutians (Adak) and to the west beneath Kamchatka after Yogodzinski et al. (2001). The geometry shown here implies that the Pacific plate is being torn in an unzipping motion as the Aleutian slab sinks to the north beneath the Bearing Sea. High Mg# andesitic volcanism is observed at Sheveluch volcano, immediately above the torn plate edge beneath Kamchatka, and above the inferred position of the active tear in the Pacific plate beneath the western Aleutians. The large arrows indicate asthenospheric flow around the plate edges and through the slab window. This kind of mantle flow would explain the melting of relatively old subducting plates along their edges, as well as the relatively high heat flow from the area of the Komandorsky basin in the western Bering Sea. Asterisks indicate the seismicity (schematically) which shoals to the north beneath Kamchatka and to the west beneath the Aleutians.

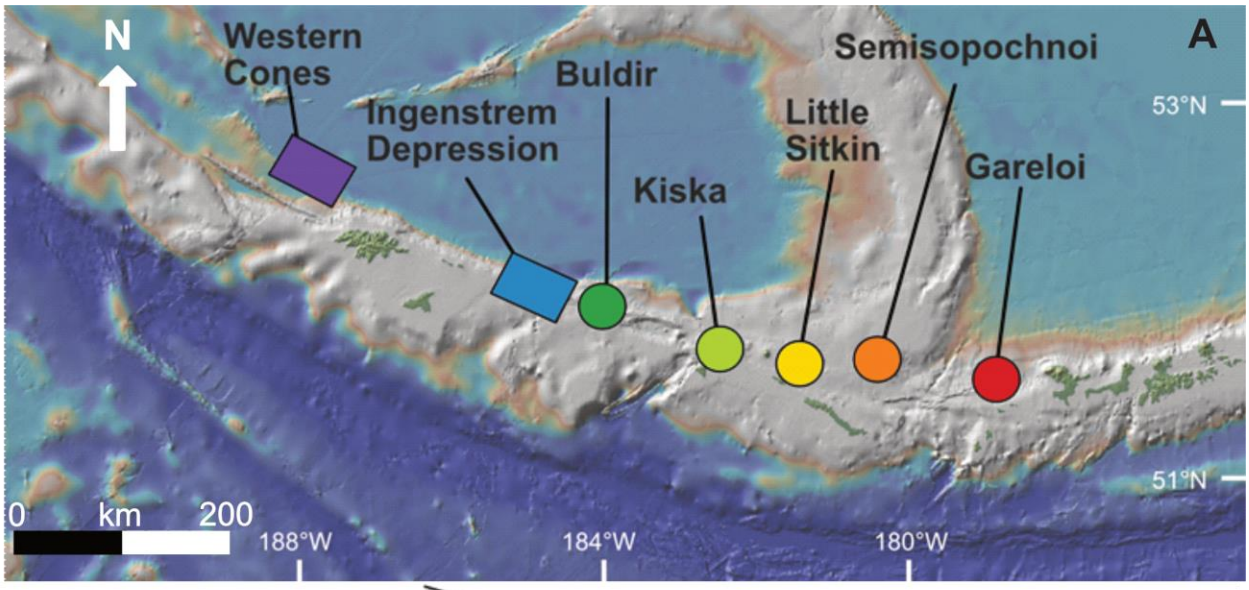
N
Western Cones
Ingenstrem Depression
Buldir
Kiska
Little Sitkin
Semisopochnoi
Gareloi
A
53°N
51°N
0 km 200
188°W
184°W
180°W

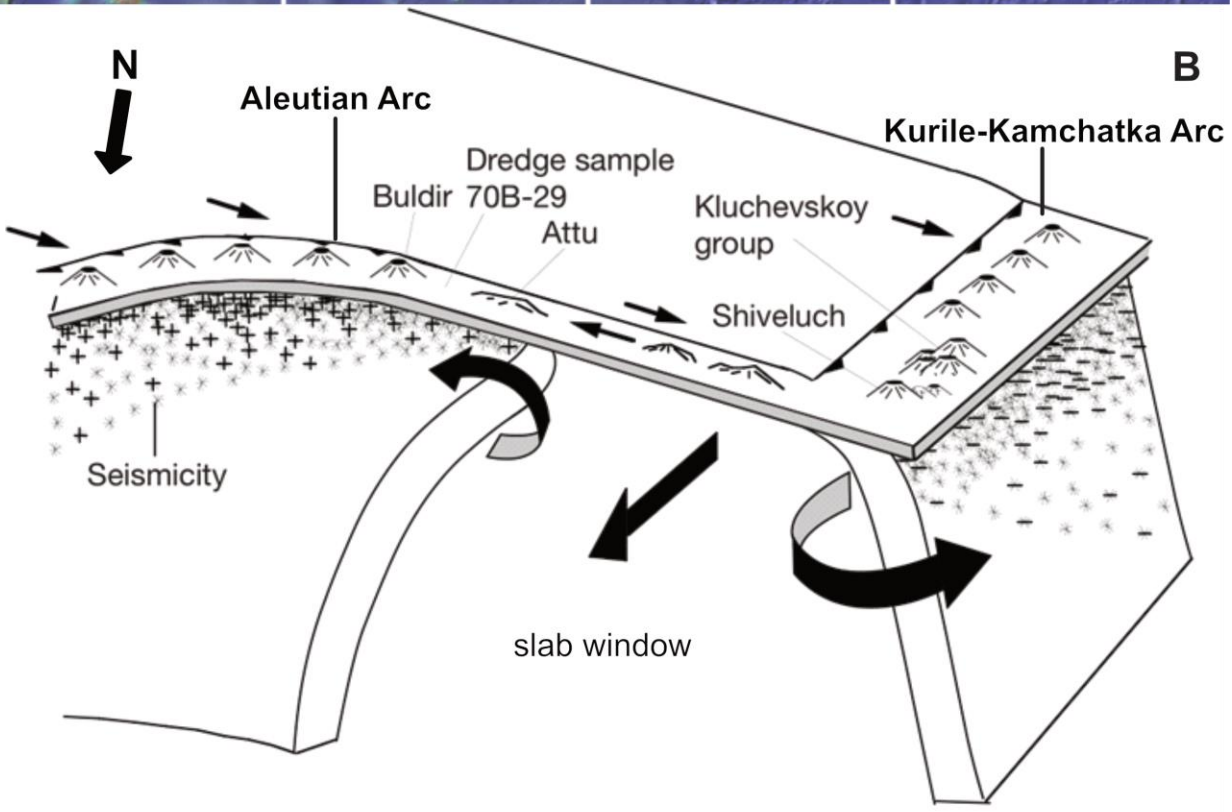
N
B
Aleutian Arc
Kurile-Kamchatka Arc
Dredge sample
Buldir 70B-29
Attu
Kluchevskoy group
Shiveluch
Seismicity
slab window

Figure 5. Geologic map of Gareloi Island from Coats (1959). A detailed geologic map of Gareloi Island from Coombs et al. (2012) is provided in the appendix of this study.

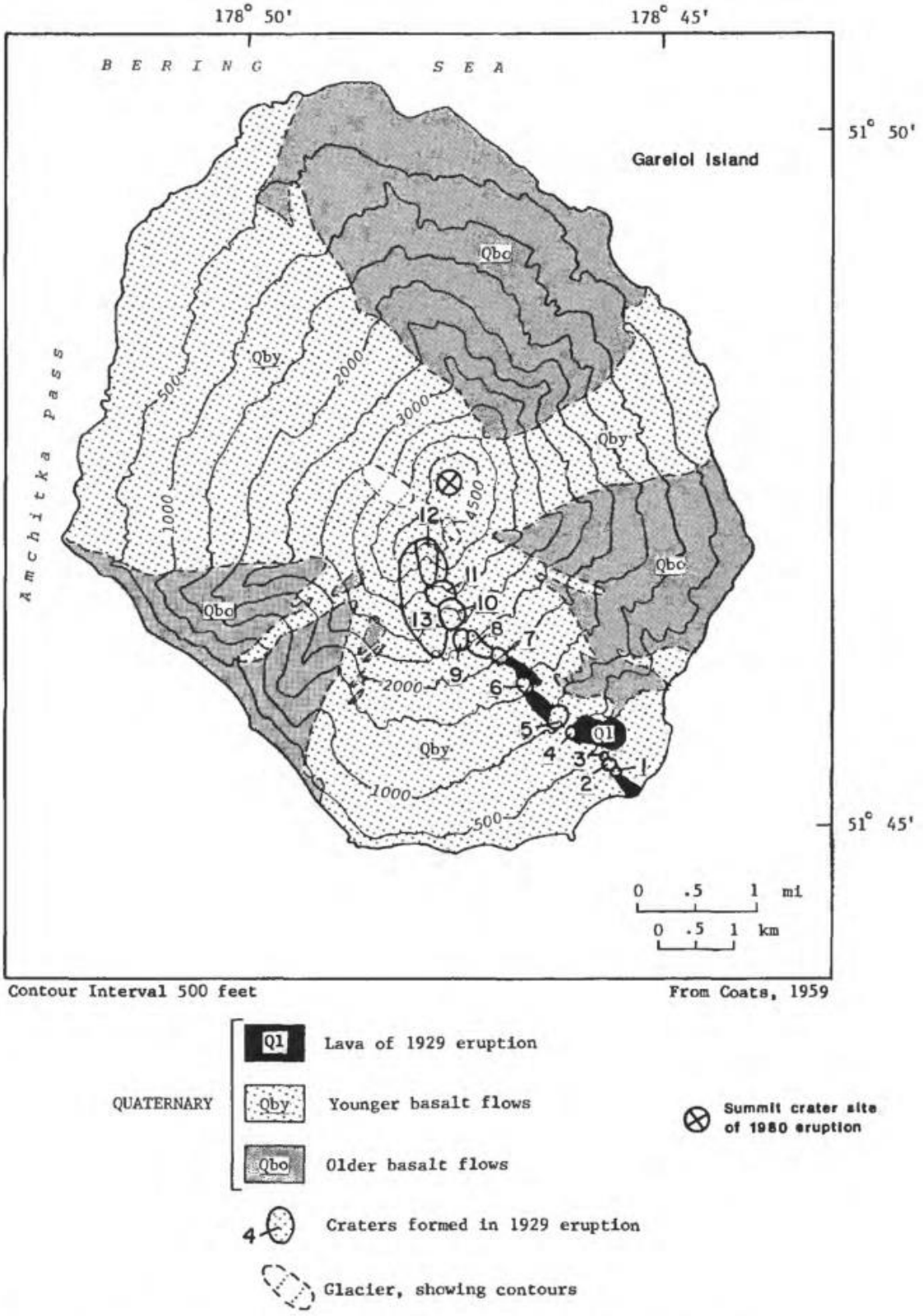
178° 50'
178° 45'
BERING SEA
51° 50'
51° 45'
Gareloi Island
Amchitka pass
Qbc
Qby
Q1
500
1000
2000
3000
4500
1
2
3
4
5
6
7
8
9
10
11
12
13
0 .5 1 mi
0 .5 1 km
Contour Interval 500 feet
From Coats, 1959
Q1 Lava of 1929 eruption
QUATERNARY
Qby Younger basalt flows
Qbo Older basalt flows
Summit crater site of 1980 eruption
Craters formed in 1929 eruption
Glacier, showing contours

Figure 6. Geologic map of Kiska Island from Coats et al. (1961).

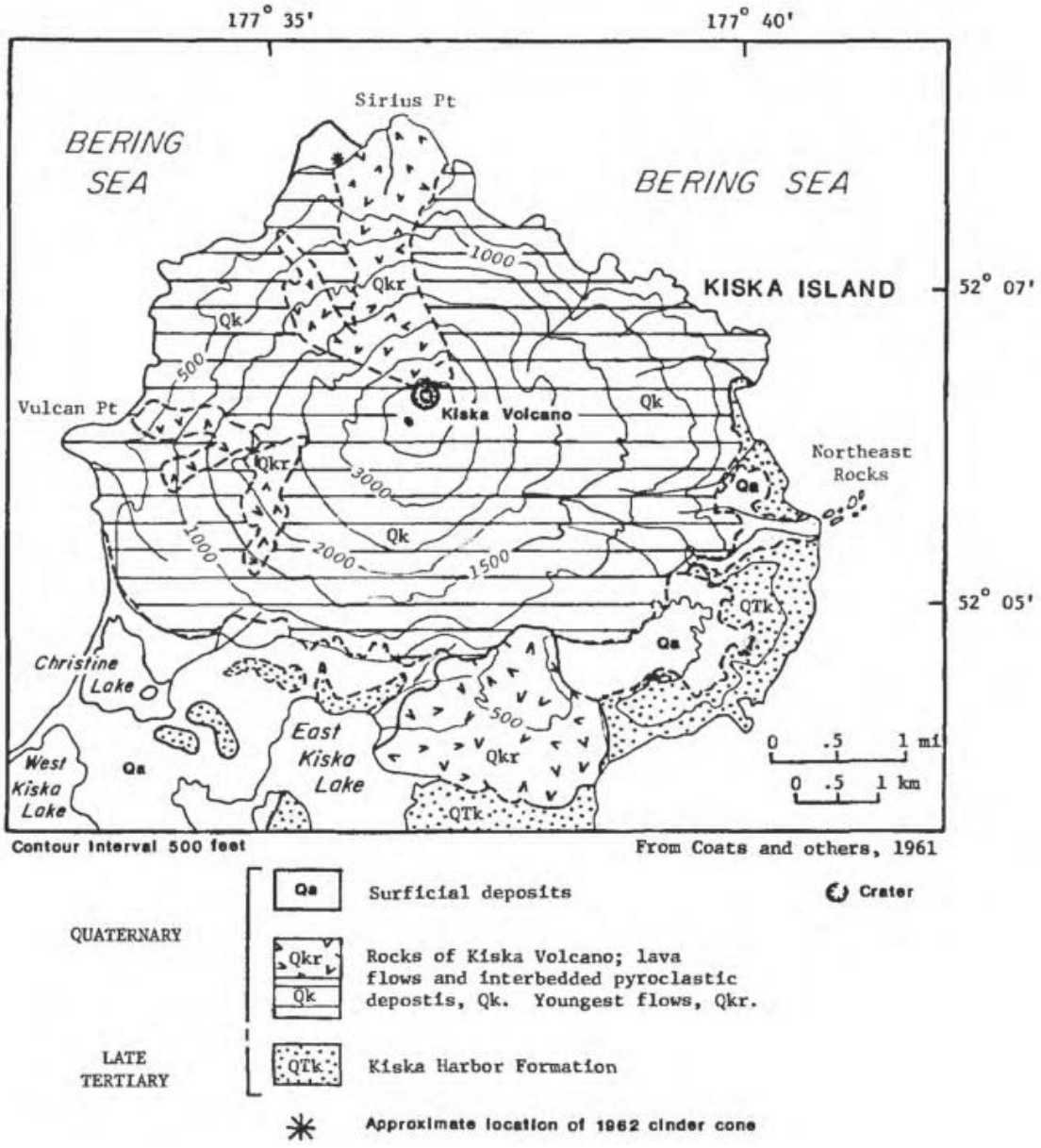
177° 35'
177° 40'
52° 07'
52° 05'
Sirius Pt
BERING SEA
BERING SEA
KISKA ISLAND
1000
Qkr
Qk
500
Vulcan Pt
Kiska Volcano
Qk
Northeast Rocks
Qa
Qkr
3000
1000
Qk
2000
1500
QTk
Qa
Christine Lake
500
East Kiska Lake
Qkr
West Kiska Lake
Qa
QTk
0 .5 1 mi
0 .5 1 km
Contour interval 500 feet
From Coats and others, 1961
Crater
QUATERNARY
Qa
Surficial deposits
Qkr
Qk
Rocks of Kiska Volcano; lava flows and interbedded pyroclastic depostis, Qk. Youngest flows, Qkr.
LATE TERTIARY
QTk
Kiska Harbor Formation
Approximate location of 1962 cinder cone

Figure 7. Primary melt composition derived from peridotite as a function of temperature, pressure, and melt fraction (Kushiro, 2001).

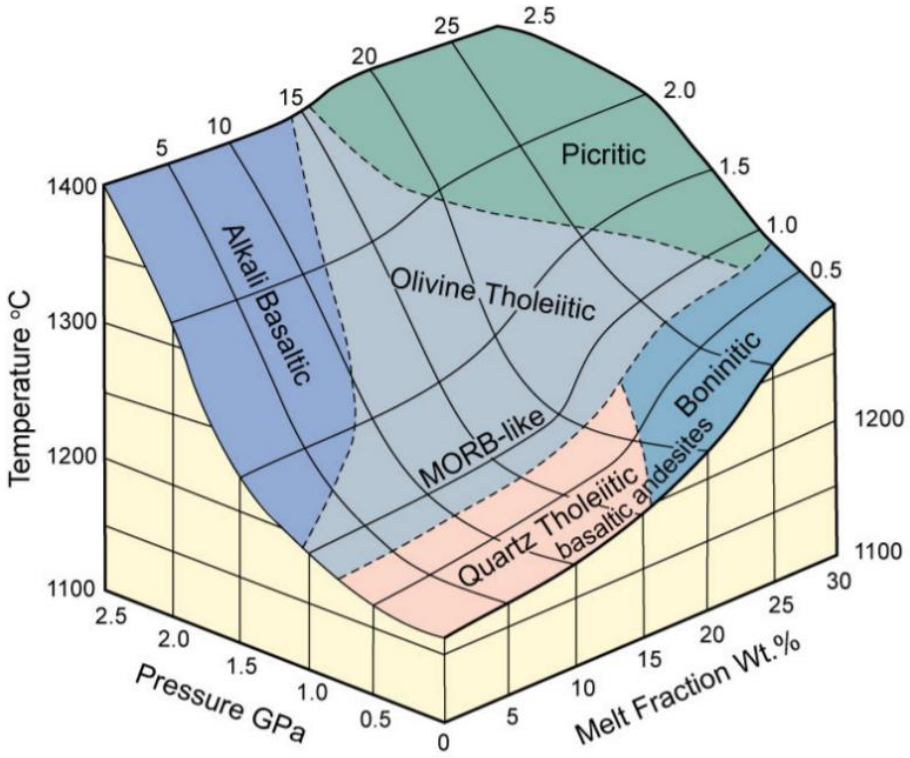
Temperature °C
1400
1300
1200
1100
Pressure GPa
2.5
2.0
1.5
1.0
0.5
0
Melt Fraction Wt.%
5
10
15
20
25
30
1200
1100
Picritic
Alkali Basaltic
Olivine Tholeiitic
MORB-like
Boninitic
Quartz Tholeiitic
basaltic andesites

Figure 8. Schematic diagram from Kay and Kay (1994) illustrating the role tectonic regime plays in generating tholeiitic to calc-alkaline magmas.

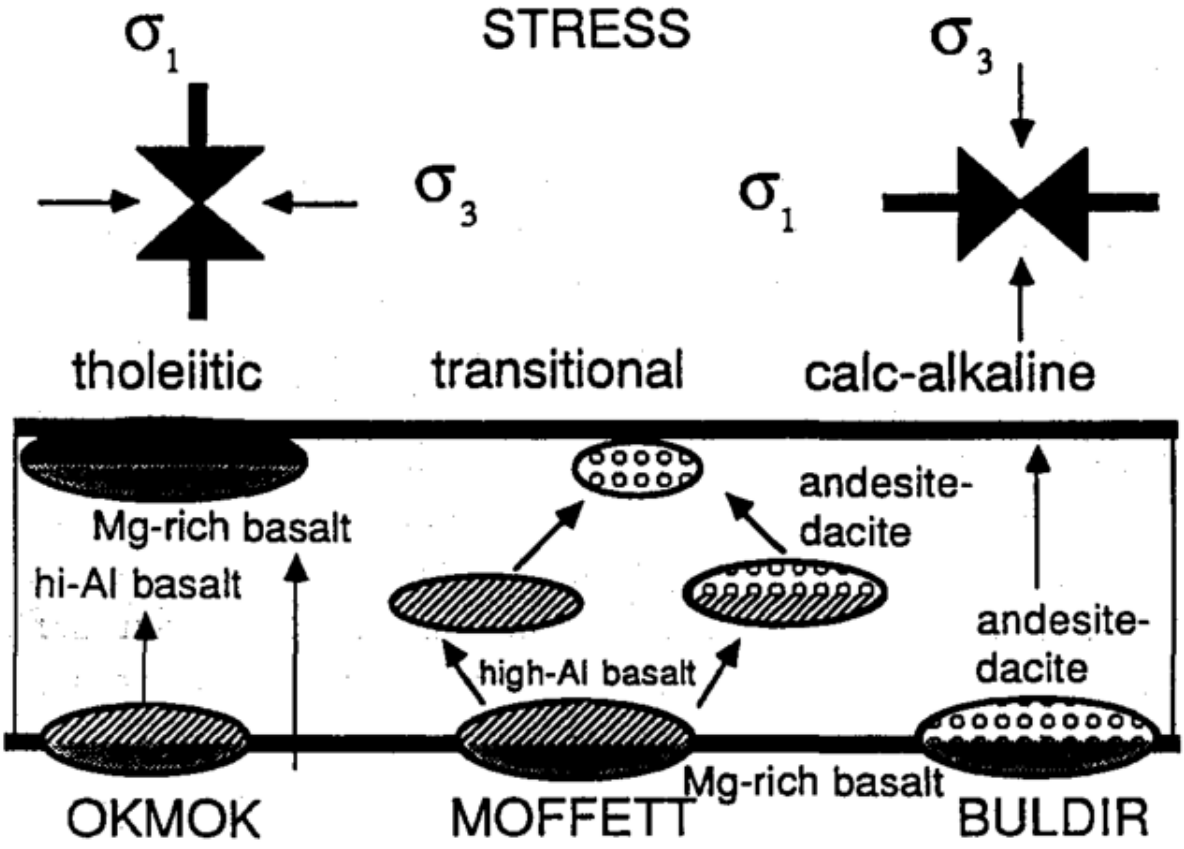
σ1
STRESS
σ3
σ3
σ1
tholeiitic
transitional
calc-alkaline
Mg-rich basalt
hi-Al basalt
andesite-
dacite
high-Al basalt
andesite-
dacite
Mg-rich basalt
OKMOK
MOFFETT
BULDIR

Figure 9. The categorization of the alkaline and sub-alkaline magmatic series from Irvine and Baragar (1971). Gareloi samples with >53.5 wt. % SiO_2 are classified as alkaline rocks. However, given that more primitive samples from Gareloi are sub-alkaline and the suite is assumed to be comagmatic, this study will use the term “tholeiite” to describe Gareloi rocks.

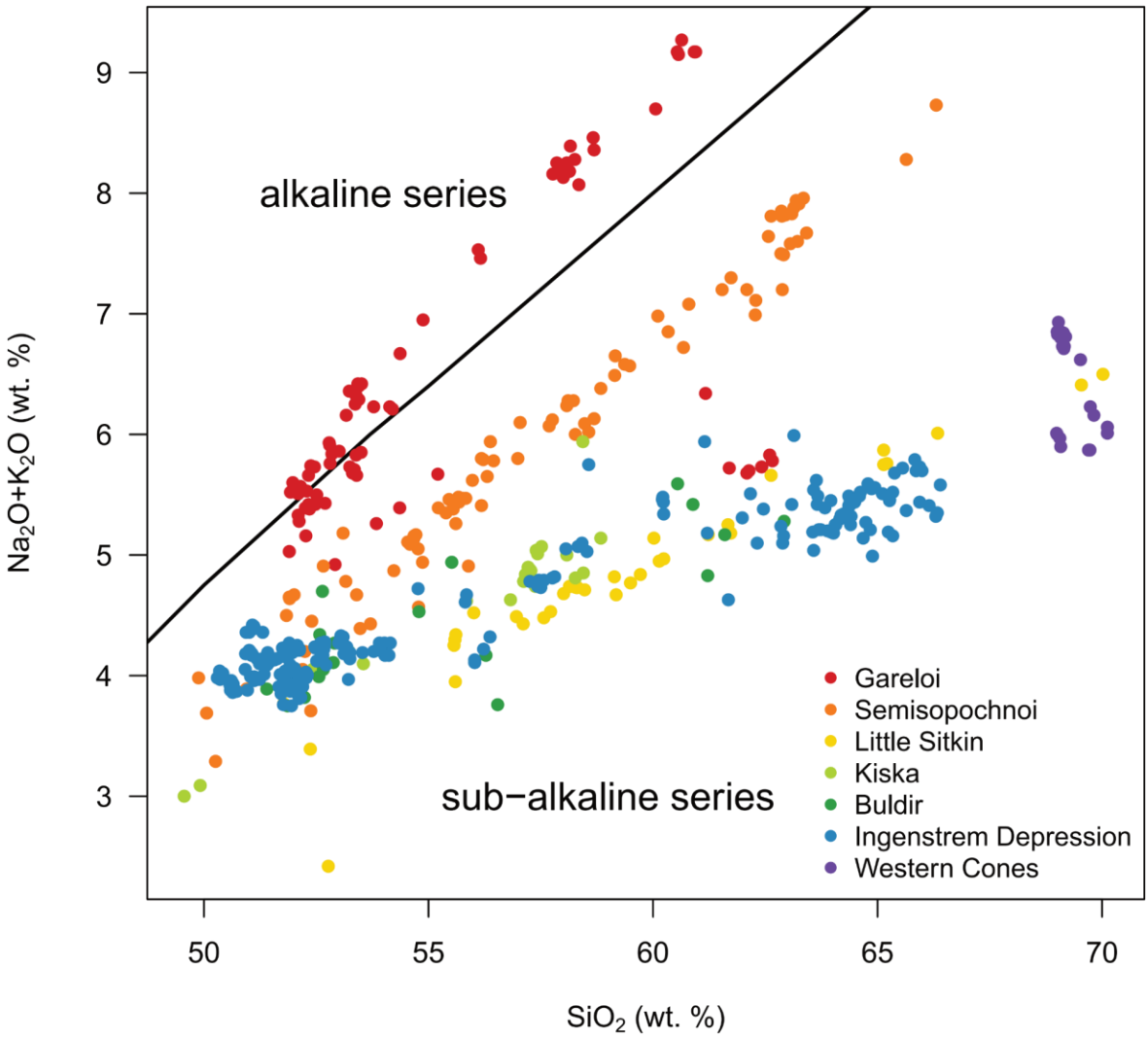
alkaline series
sub−alkaline series
Gareloi
Semisopochnoi
Little Sitkin
Kiska
Buldir
Ingenstrem Depression
Western Cones
Na2O+K2O (wt. %)
SiO2 (wt. %)
3
4
5
6
7
8
9
50
55
60
65
70

Figure 10. The locations of samples analyzed within this study.

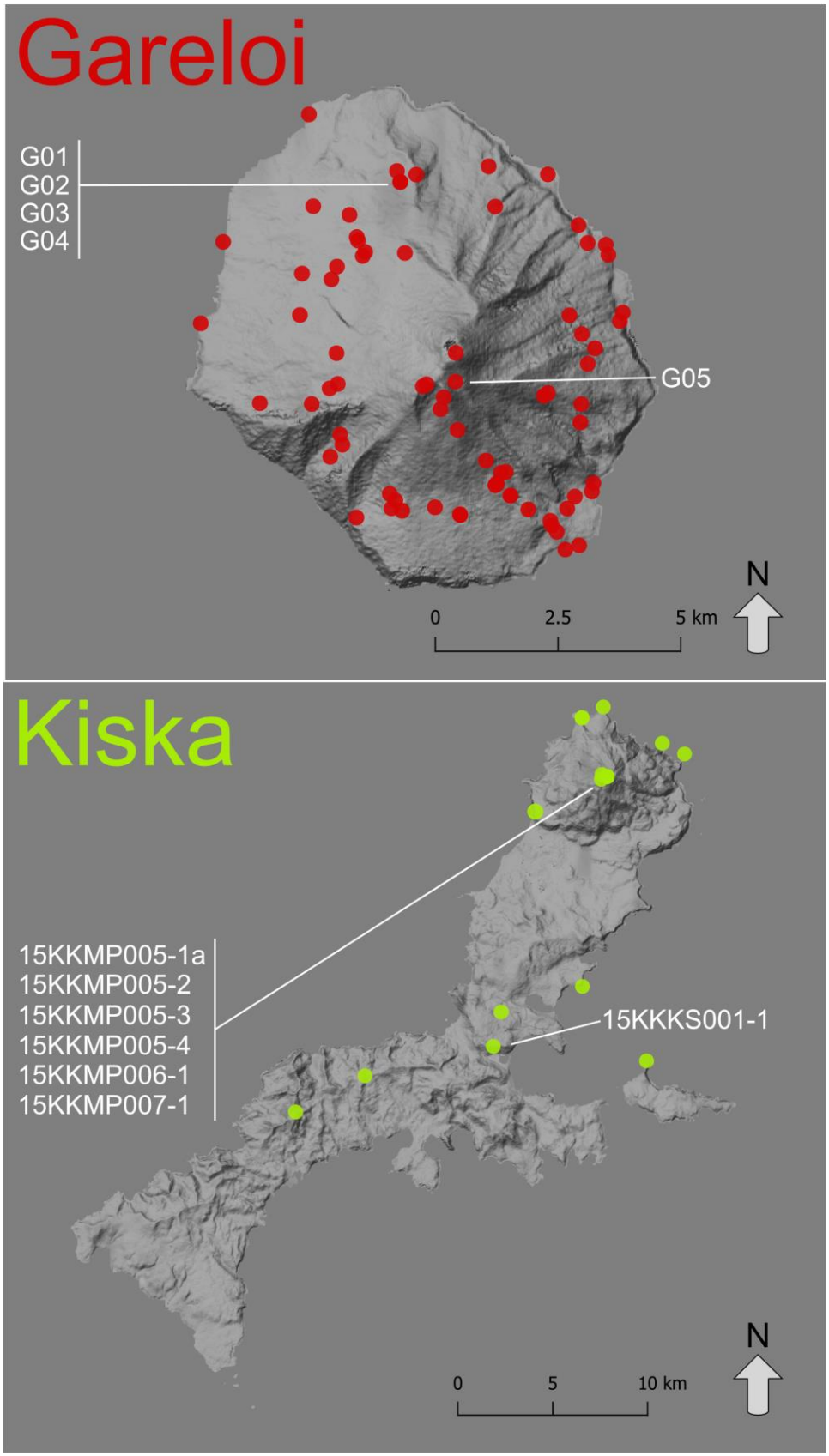
Gareloi
G01
G02
G03
G04
G05
N
0
2.5
5 km
Kiska
15KKMP005-1a
15KKMP005-2
15KKMP005-3
15KKMP005-4
15KKMP006-1
15KKMP007-1
15KKKS001-1
N
0
5
10 km

Figure 11. Gareloi scoria (A–B) and lithic fragments (C) collected proximal to GANO Seismic Station constructed as 1-inch epoxy rounds for SEM and EMPA analysis.

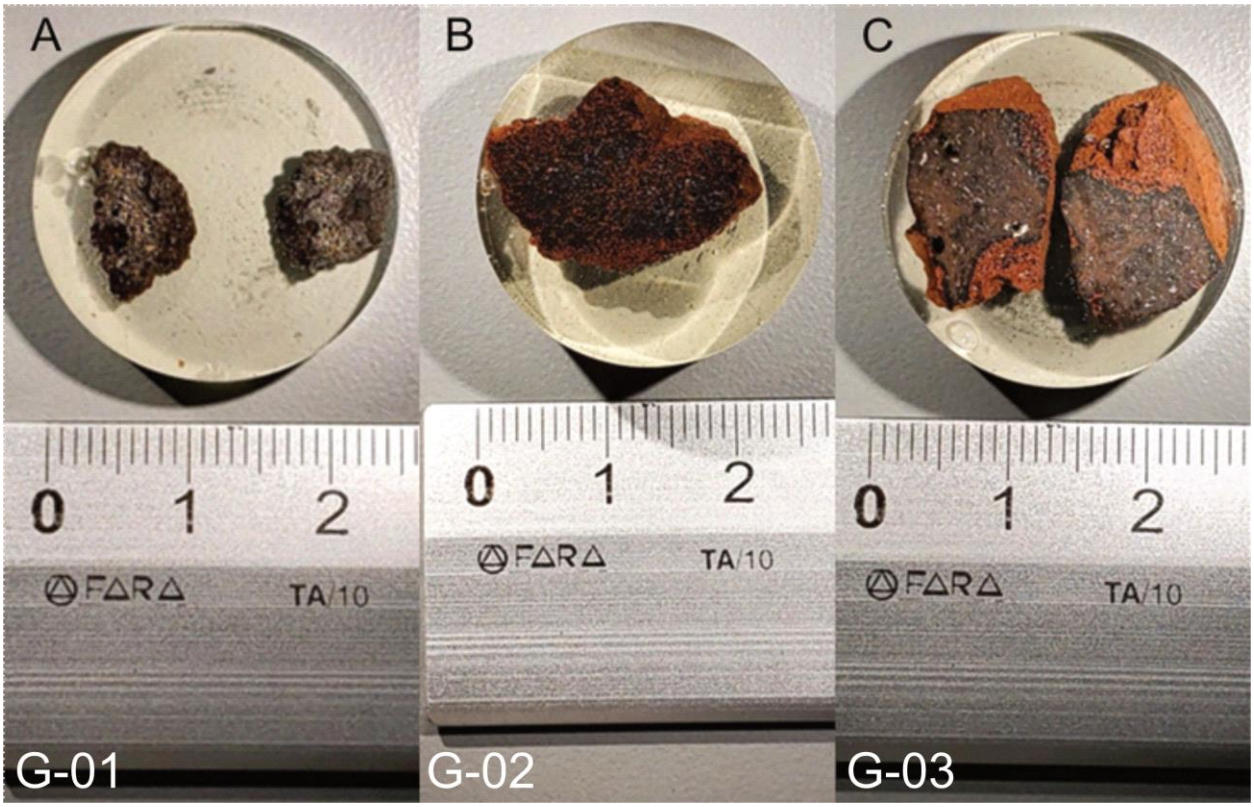
A
B
C
0 1 2
FARA
TA/10
G-01
G-02
G-03

Figure 12. Seven Kiska samples and one aggregate of scoria from Gareloi (G-04) were cut using a wet saw to remove surficial weathering and then cleaned using a DI-water sonication bath. Samples were then sent to the Peter Hooper GeoAnalytical Lab at Washington State University for bulk major and trace element analysis by use of XRF and ICP-MS, respectively.

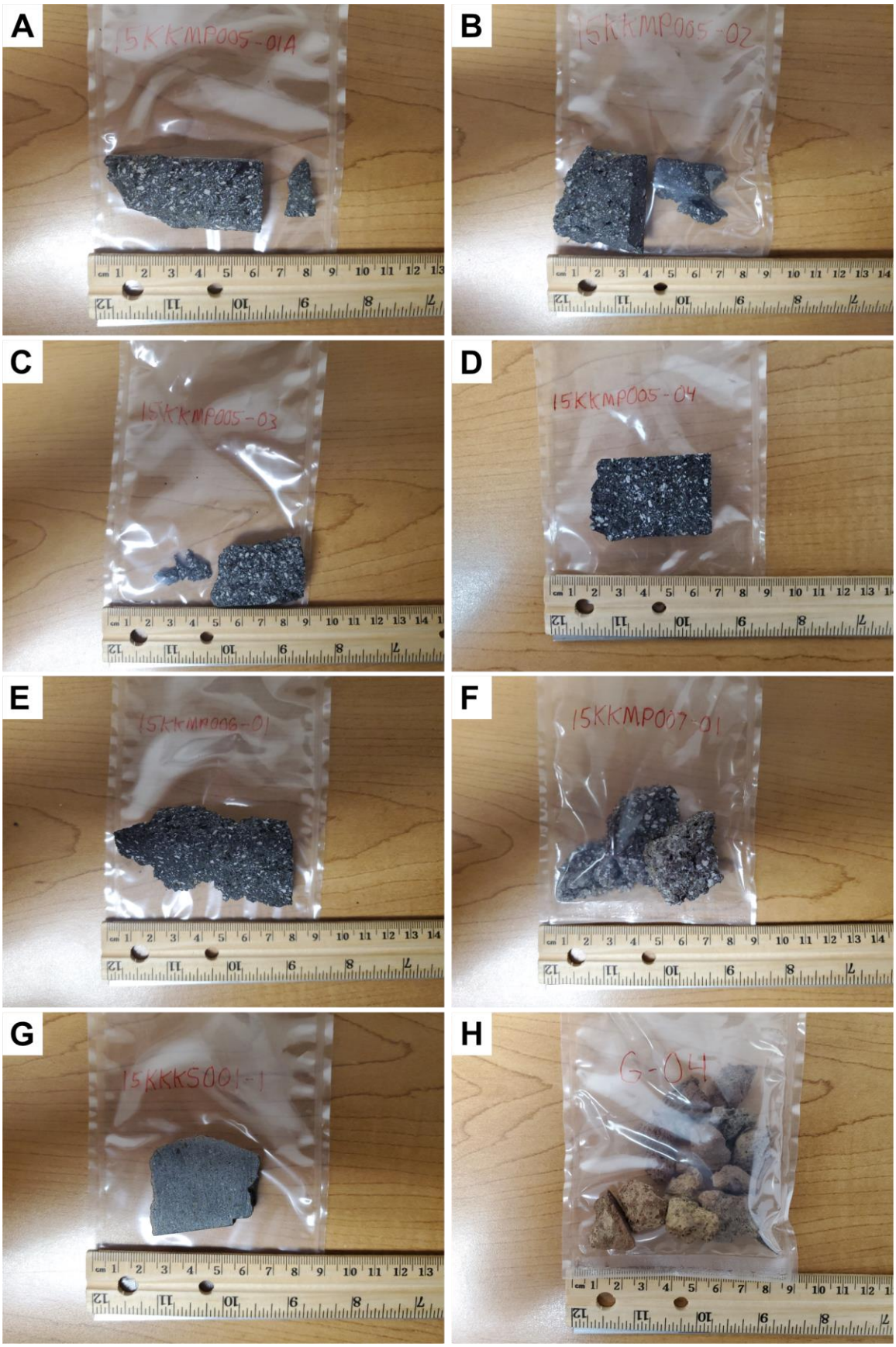
A
15KKMP005-01A
B
15KKMP005-02
C
15KKMP005-03
D
15KKMP005-04
E
15KKMP006-01
F
15KKMP007-01
G
15KKKS001-1
H
G-04

Figure 13. A mosaic of photomicrographs from sample 15KKMP006-01. All thin sections analyzed are 40 μm thick. Each thin section mosaic was point counted on a randomized grid for 1000 points within JMicroVision in order to derive modal mineralogy.

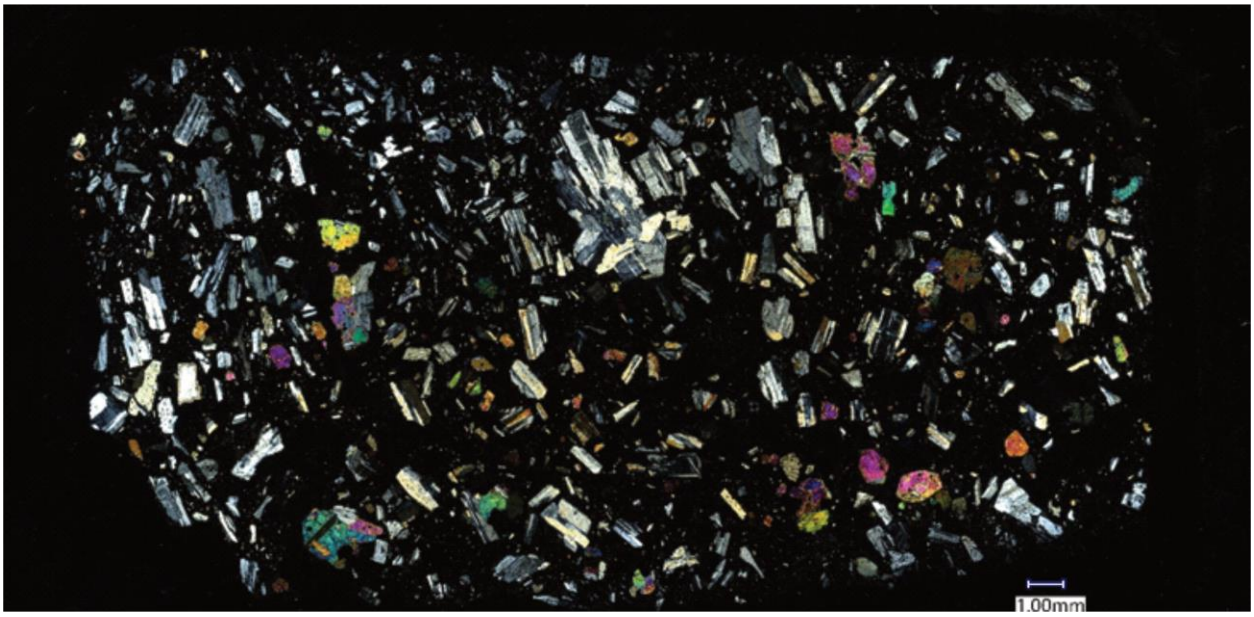
1.00mm

Figure 14. Photomicrographs of Kiska (A–F) and Gareloi samples (G–H); plag, plagioclase; cpx, clinopyroxene; v, vesicle; opx, orthopyroxene; ol, olivine. All thin sections analyzed are 40 μm thick. A) Clinopyroxene and plagioclase phenocrysts with disequilibrium textures and oxide inclusions. Sector zoning indicated by heterogeneous interference colors as well as twinning are common for clinopyroxenes (15KKMP0050-1A). B) Phenocrysts up to ~3400 μm in length are present within sample 15KKMP0050-1A. Oscillatory zoning is present in nearly half of the larger phenocrysts. C) A cumulophyric clot of plagioclase + clinopyroxene + oxides (15KKMP006-01). D) A resorbed orthopyroxene phenocryst (first order yellow interference color) with an oxide inclusion at the interface between phenocryst and groundmass (15KKMP50-52). E) The only cumulophyric clot (plagioclase + clinopyroxene + oxides) present within sample 15KKKS00-11**,** a hyaloclastite collected on a high ridge south of Kiska harbor on the east side of the lagoon**.** Note the plagioclase rich nature of the sample and the prominent palagonite (orange–red) overprint within the groundmass. F) The largest plagioclase phenocryst from sample 15KKKS00-11 (~1750 μm in length). Note the sieved nature of the phenocryst and the embayed rims. G) A cumulophyric clot of clinopyroxene + olivine + oxides. Inclusions of olivine (light-blue interference colors) are present within clinopyroxene. To the right is a sieved phenocryst of plagioclase (G-04). H) A cumulophyric clot of clinopyroxene + plagioclase. Clinopyroxene has inclusions of plagioclase and oxides. Plagioclase contains inclusions of olivine (pink interference color). Plagioclase is sieved and has embayed rims. On the right is a cumulophyric clot of clinopyroxene + olivine + oxides (G-04).

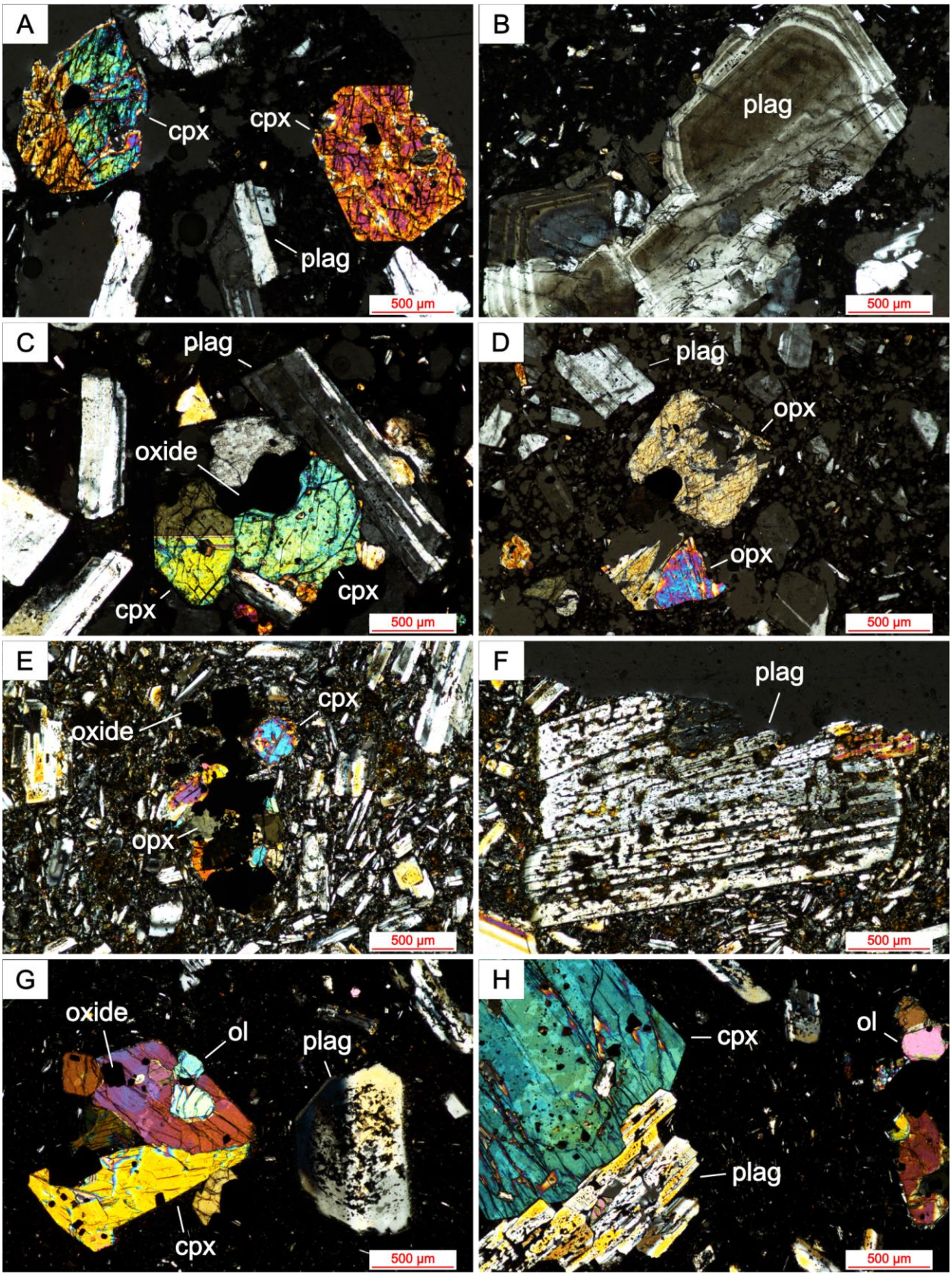
A
cpx
cpx
plag
500 µm
B
plag
500 µm
C
plag
oxide
cpx
cpx
500 µm
D
plag
opx
opx
500 µm
E
oxide
cpx
opx
500 µm
F
plag
500 µm
G
oxide
ol
plag
cpx
500 µm
H
cpx
ol
plag
500 µm

Figure 15. Mineral discrimination diagrams from EPMA data. The only exception is Kiska olivine compositions were collected using SEM. A) Pyroxene ternary diagrams showing the compositions of the pyroxene present in both Kiska and Gareloi samples. B) Fo (mol %) of olivine compositions from both Kiska and Gareloi C) Feldspar ternary diagrams showing the composition of plagioclase in Kiska and Gareloi samples. Wo, wollastonite; En, enstatite; Fs, ferrosillite; Or, orthoclase; Ab, albite; An, anorthite.

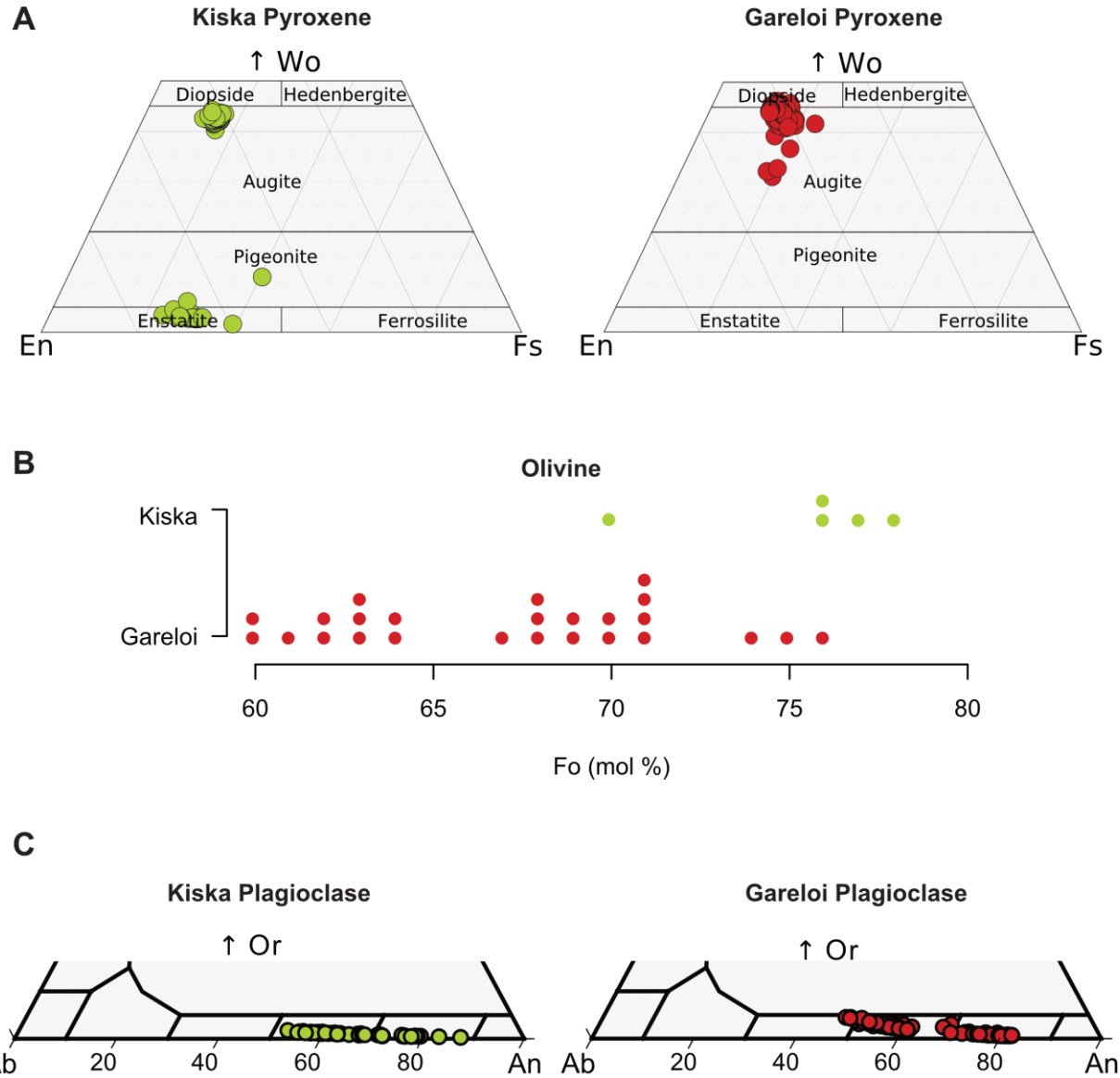
A
Kiska Pyroxene
↑ Wo
Diopside
Hedenbergite
Augite
Pigeonite
Enstatite
Ferrosilite
En
Fs
Gareloi Pyroxene
↑ Wo
Diopside
Hedenbergite
Augite
Pigeonite
Enstatite
Ferrosilite
En
Fs
B
Olivine
Kiska
Gareloi
60
65
70
75
80
Fo (mol %)
C
Kiska Plagioclase
↑ Or
Ab
20
40
60
80
An
Gareloi Plagioclase
↑ Or
Ab
20
40
60
80
An

Figure 16. BSE images from SEM with a white line demarcating the location of mineral transect data collected using EDS. A) A representative plagioclase phenocryst from Kiska sample 15KKMP005-03. Anorthite content oscillates from core to rim before a homogenous rim of 60 mol % is reached. B) A representative plagioclase phenocryst from Gareloi sample G-05. Anorthite content oscillates from ~70 to 81 mol % before reaching a homogenous rim of ~60 mol %.

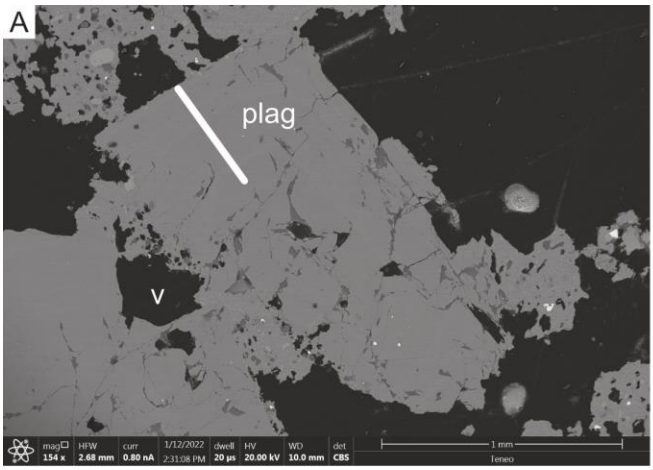
A
plag
v
mag HFW curr 1/12/2022 dwell HV WD det
154 x 2.68 mm 0.80 nA 2:31:08 PM 20 µs 20.00 kV 10.0 mm CBS
1 mm
Teneo

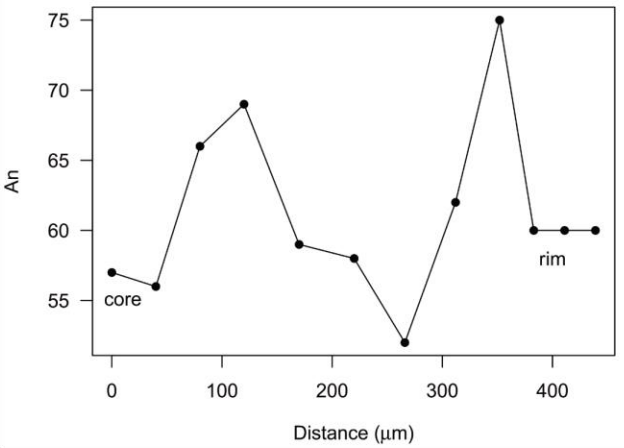
An
75
70
65
60
55
core
rim
0
100
200
300
400
Distance (µm)

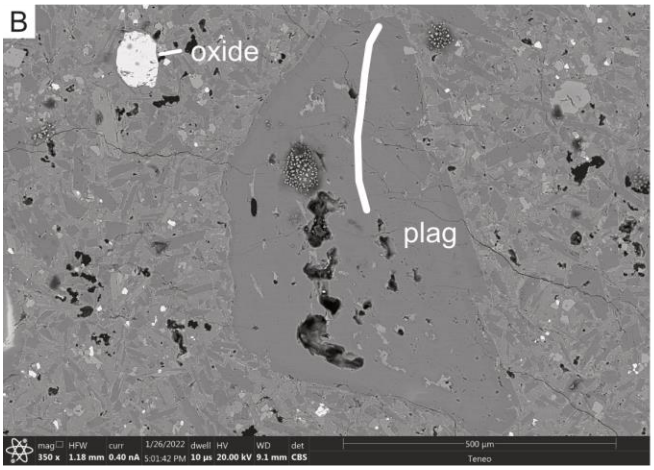
B
oxide
plag
mag HFW curr 1/26/2022 dwell HV WD det
350 x 1.18 mm 0.40 nA 5:01:42 PM 10 µs 20.00 kV 9.1 mm CBS
500 µm
Teneo

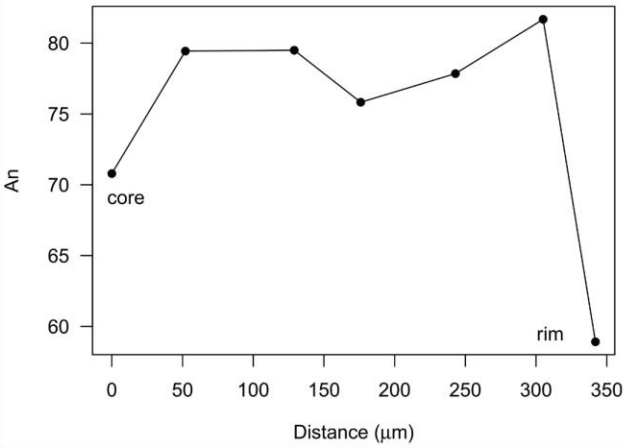
An
80
75
70
65
60
core
rim
0
50
100
150
200
250
300
350
Distance (µm)

Figure 17. BSE images with compositional point data captured during EPMA analysis. Images A–D are from Gareloi. Images E–H are from Kiska. A) A representative clinopyroxene phenocryst with an inclusion of spinel from sample G-01. Mg# (MgO/(MgO+FeO)*100) generally decreases from core to rim in Gareloi clinopyroxenes. B) An additional representative clinopyroxene phenocryst from sample G-01. Chemical zonation is evident from bands of lighter and darker greys within the image. C) A representative plagioclase phenocryst from sample G-01. The phenocryst has disequilibrium textures and has irregular chemical zonation patterns as indicated by oscillating An content. D) A representative microlite of plagioclase from sample G-02. Microlites of plagioclase are normally zoned in Gareloi samples. E) A representative plagioclase phenocryst from Kiska sample 15KKMP50-52. An (mol %) increases from core to rim with three distinct compositional zones indicated by grey-scale color. F) A plagioclase phenocryst from sample 15KKMP006-01. Sector zoning is evident with the highest An content being towards the rim of the phenocryst. G) A representative clinopyroxene phenocryst from sample 15KKMP50-52. Clinopyroxenes are normally zoned in Kiska samples. H) A representative plagioclase phenocryst from sample 15KKMP006-01 that has patchy zoning as indicated by An content.

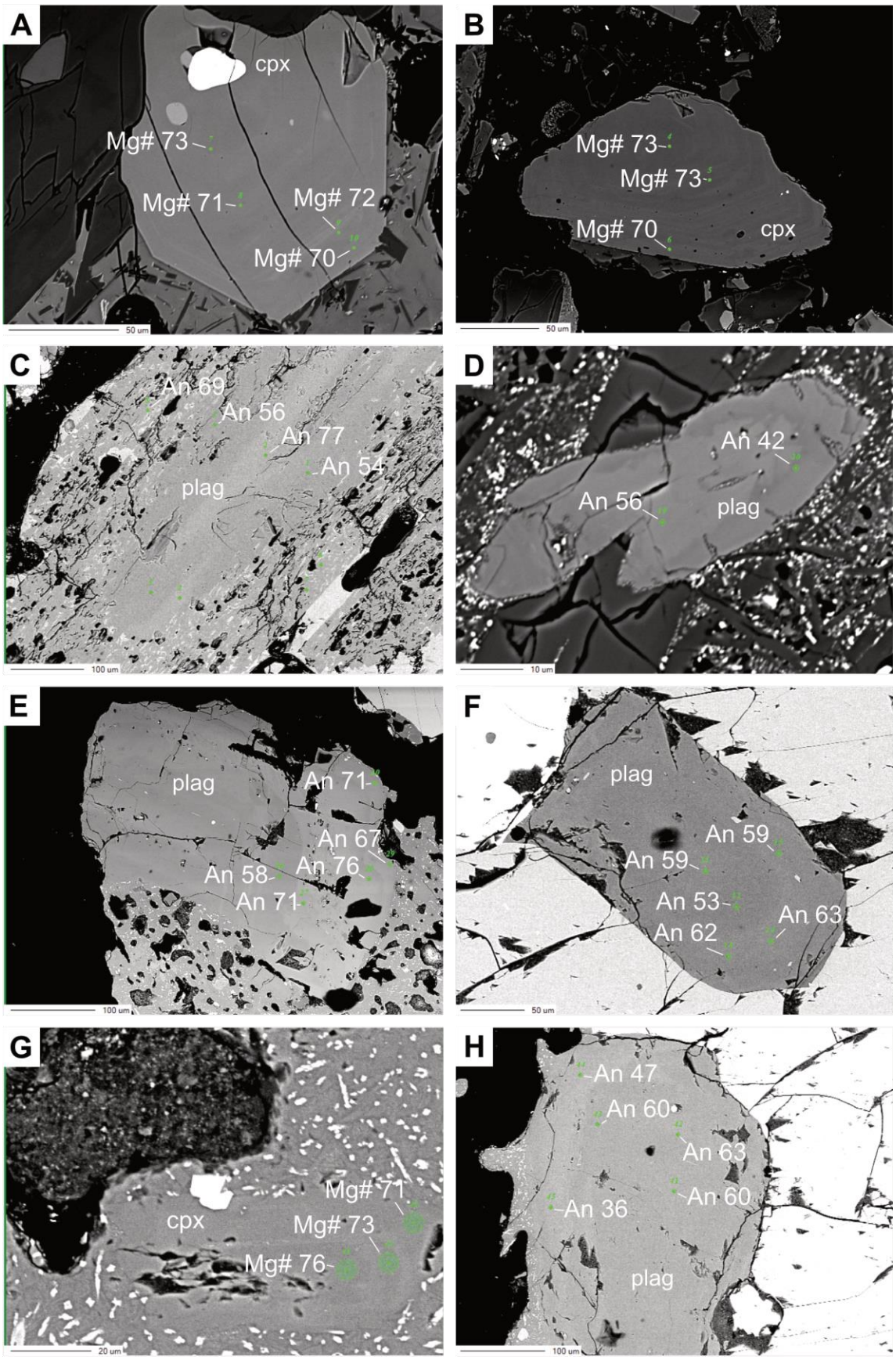
A
cpx
Mg# 73
Mg# 71
Mg# 72
Mg# 70
50 um
B
Mg# 73
Mg# 73
Mg# 70
cpx
50 um
C
An 69
An 56
An 77
An 54
plag
100 um
D
An 42
An 56
plag
10 um
E
plag
An 71
An 67
An 76
An 58
An 71
100 um
F
plag
An 59
An 59
An 53
An 63
An 62
50 um
G
Mg# 71
cpx
Mg# 73
Mg# 76
20 um
H
An 47
An 60
An 63
An 60
An 36
plag
100 um

Figure 18. BSE images from SEM with a white line demarcating the location of mineral transect data collected using EDS. A) A representative olivine phenocryst from Kiska sample 15KKMP006-01. Mg# is relatively constant (64–66) until reaching a reaction rim of orthopyroxene. B) A representative orthopyroxene phenocryst from Kiska sample 15KKMP006-01. Mg# increases from core to rim (~53.0–55.5) indicative of reverse zoning.

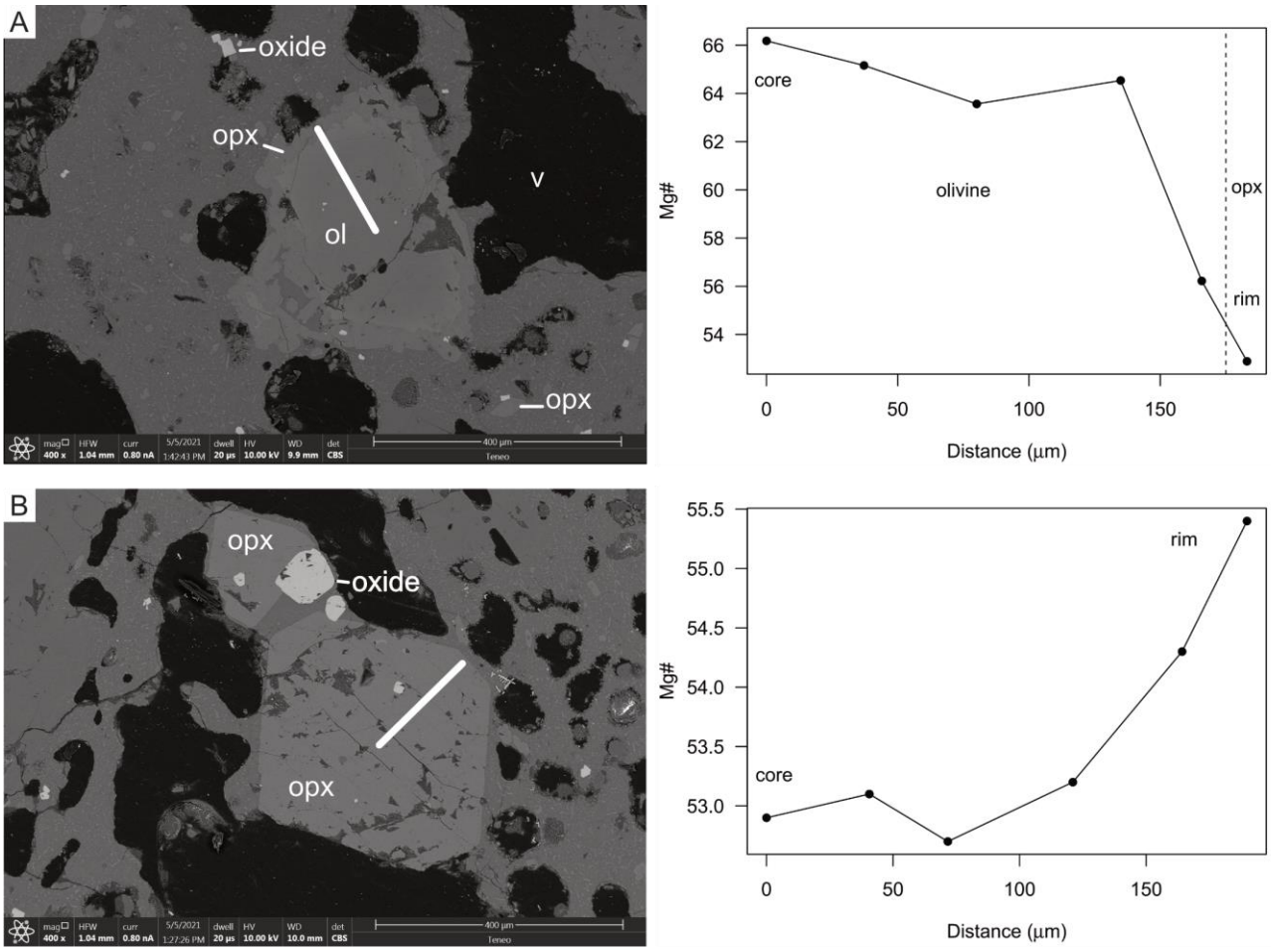
A
oxide
opx
v
ol
opx
mag HFW curr 5/5/2021 dwell HV WD det
400 x 1.04 mm 0.80 nA 1:42:43 PM 20 µs 10.00 kV 9.9 mm CBS
400 µm
Teneo
66
64
62
60
58
56
54
Mg#
core
olivine
opx
rim
0
50
100
150
Distance (µm)
B
opx
oxide
opx
mag HFW curr 5/5/2021 dwell HV WD det
400 x 1.04 mm 0.80 nA 1:27:26 PM 20 µs 10.00 kV 10.0 mm CBS
400 µm
Teneo
55.5
55.0
54.5
54.0
53.5
53.0
Mg#
rim
core
0
50
100
150
Distance (µm)

Figure 19. Rhodes diagram (olivine core Fo in mol % vs whole-rock Mg#) for Gareloi and Kiska samples. Mg# is molar MgO/(MgO+FeO) with all iron treated as FeO. Olivine-liquid equilibrium field after Roeder and Emslie (1970), using a K_D Fe-Mg of 0.30±0.03. A) G-01, B) G-02, C) G-03, D) G-05 paired with G-05 glass, E) G-05 paired with G-01 glass F) Kiska sample 15KKMP006-01, and G) olivine-liquid thermometry of Gareloi and Kiska samples conducted using equation 22 of Putirka (2008). Fo content is listed for compositions in equilibrium with resident glass. Ol, olivine.

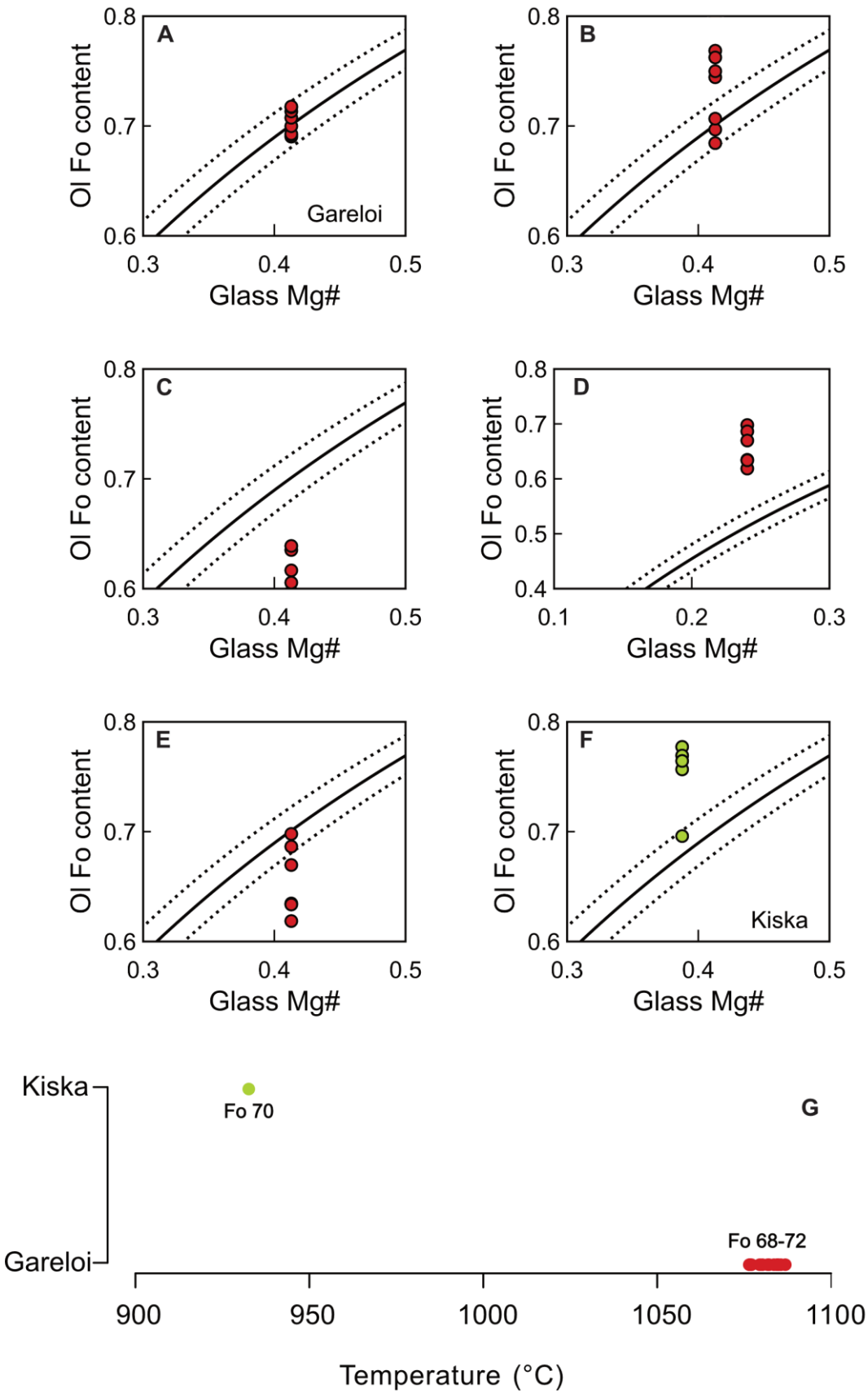
A
Gareloi
B
C
D
E
F
Kiska
Ol Fo content
Glass Mg#
G
Fo 70
Fo 68-72
Kiska
Gareloi
900
950
1000
1050
1100
Temperature (°C)

Figure 20. Rhodes diagram (Cpx Mg# vs whole-rock Mg#) for Gareloi and Kiska samples. Clinopyroxene-liquid equilibrium field after Putirka (2008), using a K_D(Fe-Mg) of 0.28±0.08. A) G-01, B) G-02, C) G-03, D) G-05 paired with G-05 glass, and E) G-05 paired with G-01 glass.

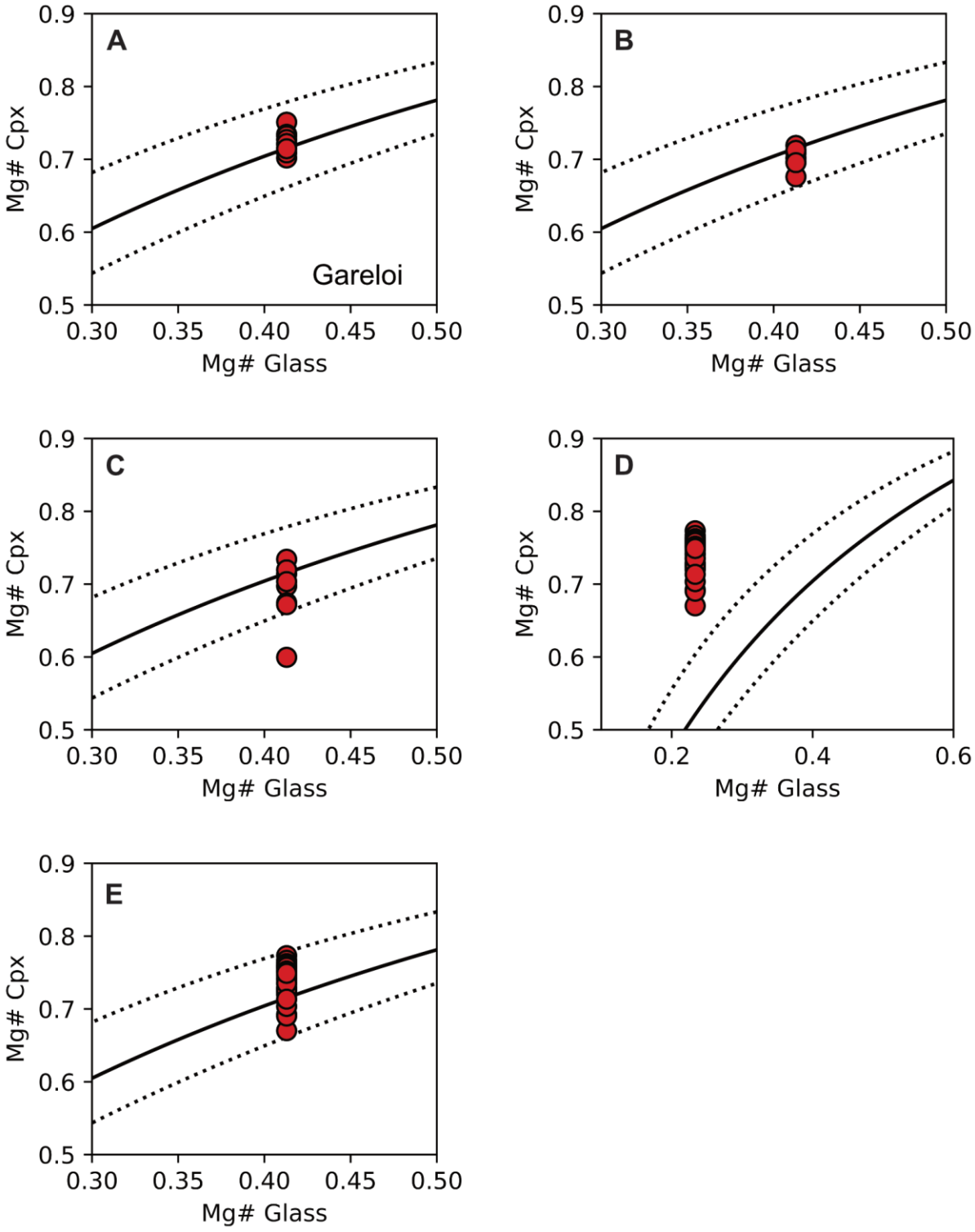
A
Gareloi
B
C
D
E
Mg# Cpx
Mg# Glass
0.9
0.8
0.7
0.6
0.5
0.30
0.35
0.40
0.45
0.50
0.2
0.4
0.6

Figure 21. Rhodes diagram (Cpx Mg# vs whole-rock Mg# and Opx Mg# vs whole-rock Mg#) for Kiska samples. Clinopyroxene-liquid equilibrium field after Putirka (2008), using a K_D(Fe-Mg) of 0.28±0.08. Orthopyroxene-liquid equilibrium field after Putirka (2008), using a K_D (Fe-Mg) of 0.29±0.07. A) 15KKMP005-02, B) 15KKMP006-01, C) 15KKMP005-02, and D) 15KKMP006-01.

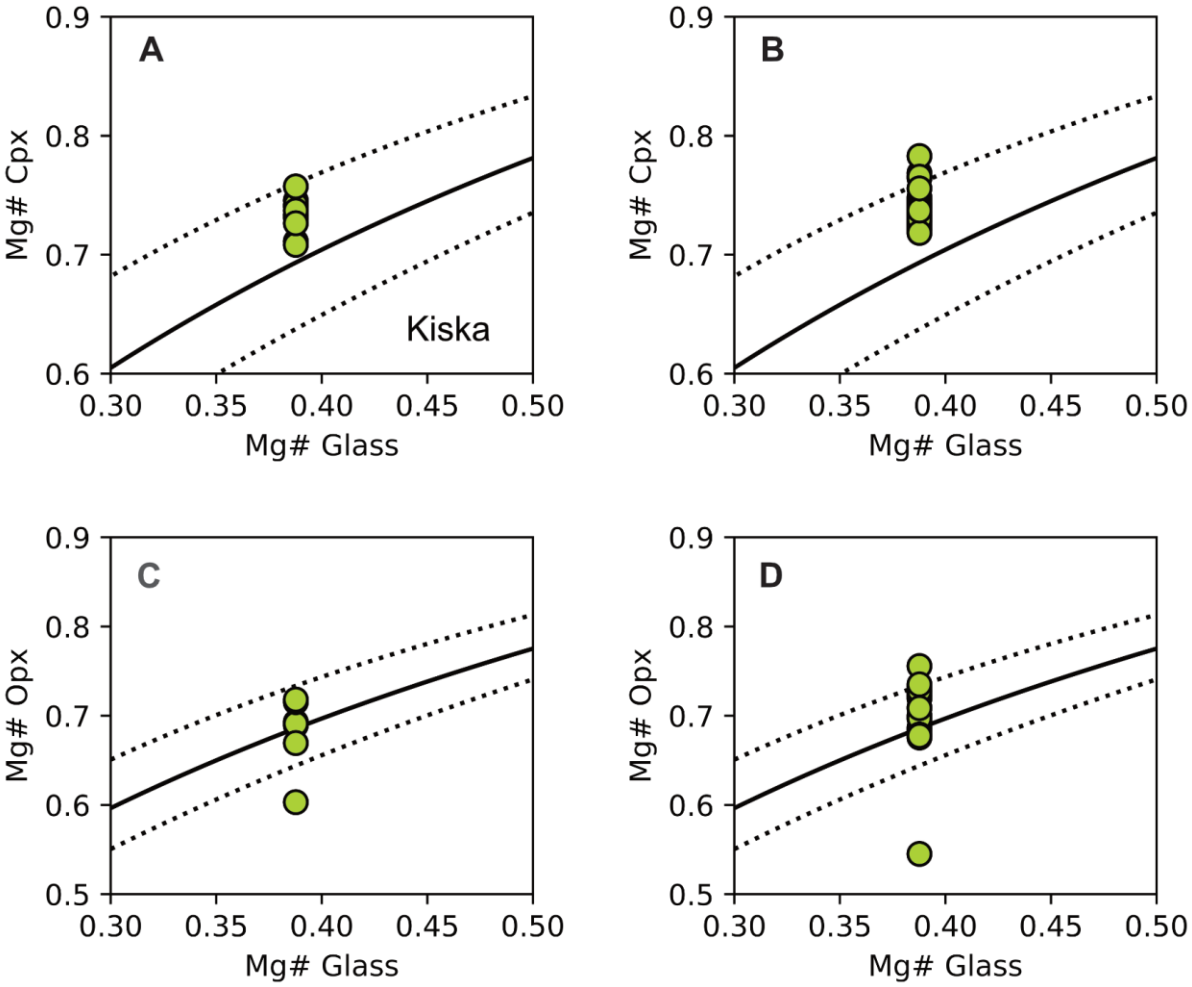
A
B
C
D
Kiska
Mg# Cpx
Mg# Opx
Mg# Glass
0.9
0.8
0.7
0.6
0.5
0.30
0.35
0.40
0.45
0.50

Figure 22. Thermobarometry of Kiska and Gareloi clinopyroxene compositions using equation 30 for pressure and equation 33 for temperature from the model of Putirka (2008). A) Temperature (°C) vs. Mg# for Gareloi and Kiska clinopyroxene compositions, and B) pressure (kbar) vs. Mg# for Gareloi and Kiska clinopyroxene compositions.

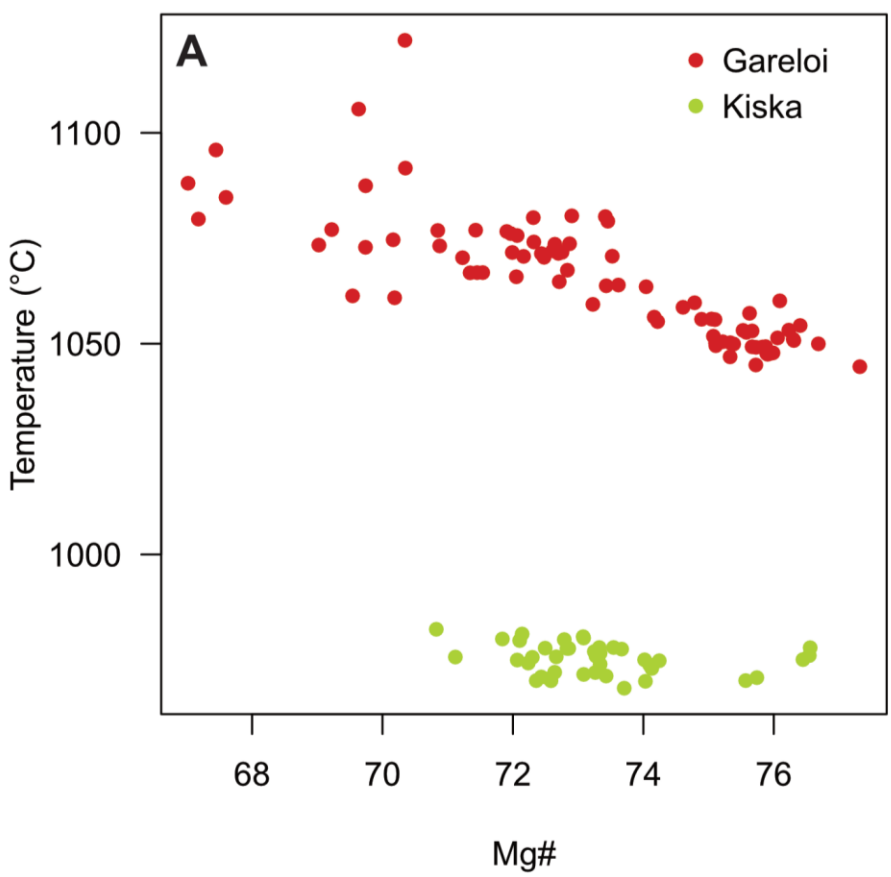
A
Gareloi
Kiska
1100
1050
1000
Temperature (°C)
68
70
72
74
76
Mg#

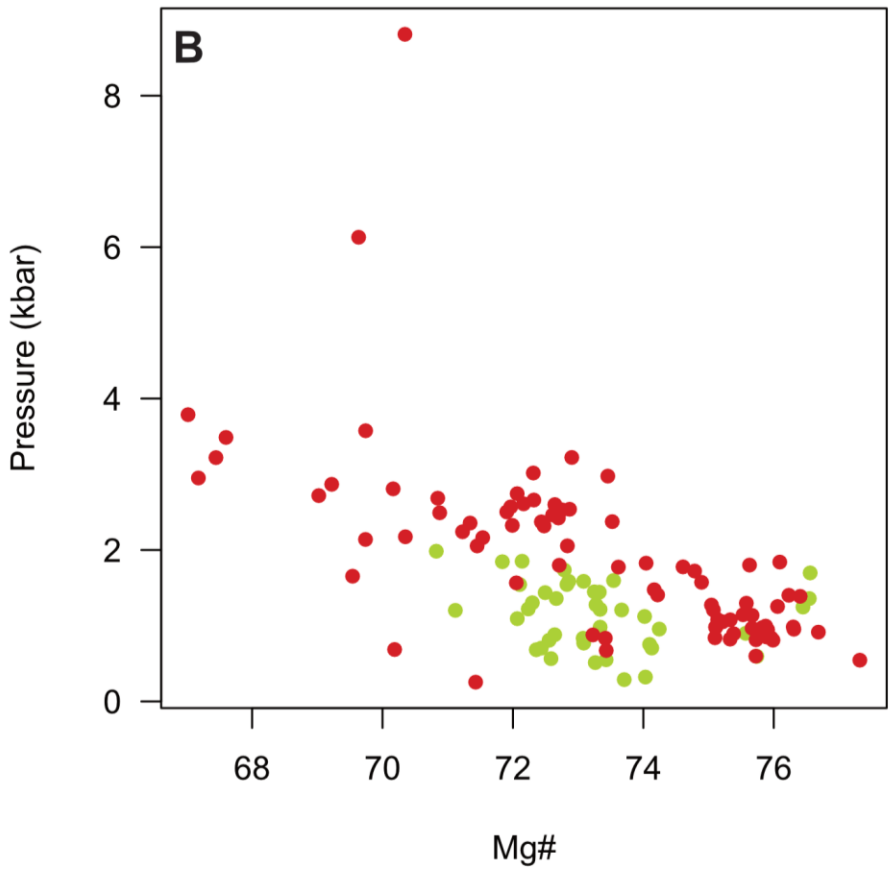
B
8
6
4
2
0
Pressure (kbar)
68
70
72
74
76
Mg#

Figure 23. Thermobarometry of Kiska orthopyroxene compositions using equation 29b for pressure from the model of Putirka (2008) and the geothermometer of Beattie (1993). A) Temperature (°C) vs. Mg# for Kiska orthopyroxene compositions, and B) pressure (kbar) vs. Mg# for Kiska orthopyroxene compositions.

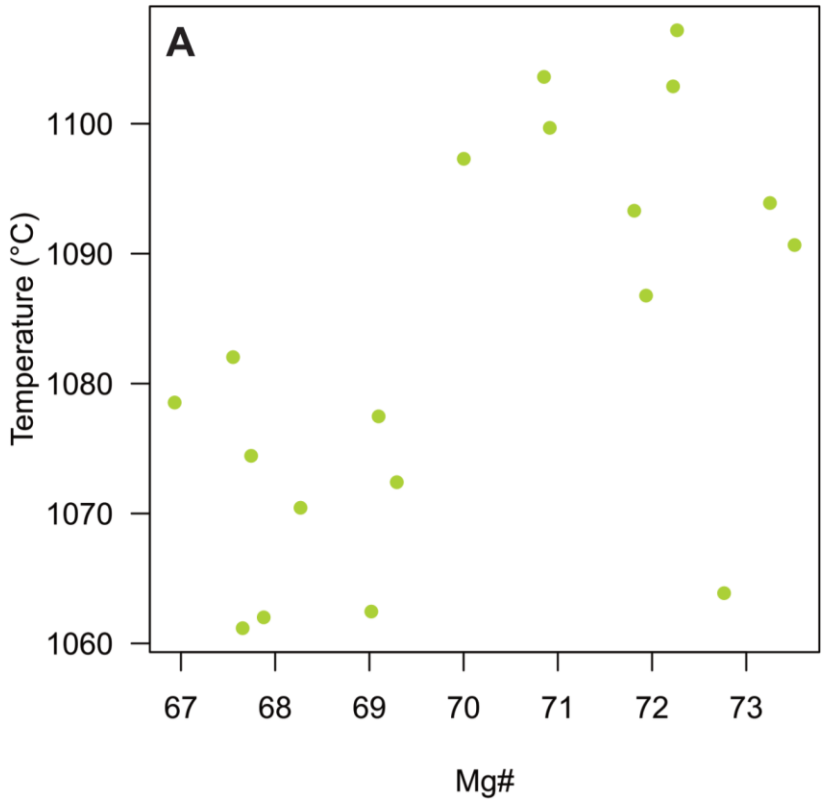
A
Temperature (°C)
1100
1090
1080
1070
1060
67
68
69
70
71
72
73
Mg#

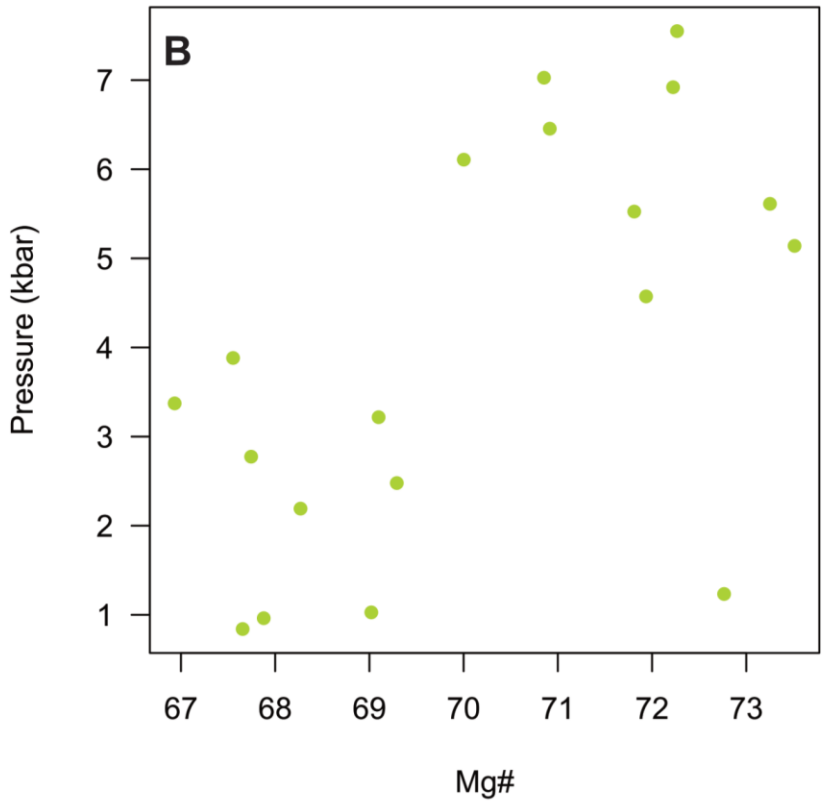
B
Pressure (kbar)
7
6
5
4
3
2
1
67
68
69
70
71
72
73
Mg#

Figure 24. H_2O vs. An content for Gareloi and Kiska samples using the plagioclase-liquid hygrometer of Waters and Lange (2015). A temperature of 980 °C was used for Gareloi samples based upon matching between MELTS and sample average An content (68 mol %). A temperature of 964 °C was used for Kiska samples based upon matching between MELTS and sample average An content (64 mol %).

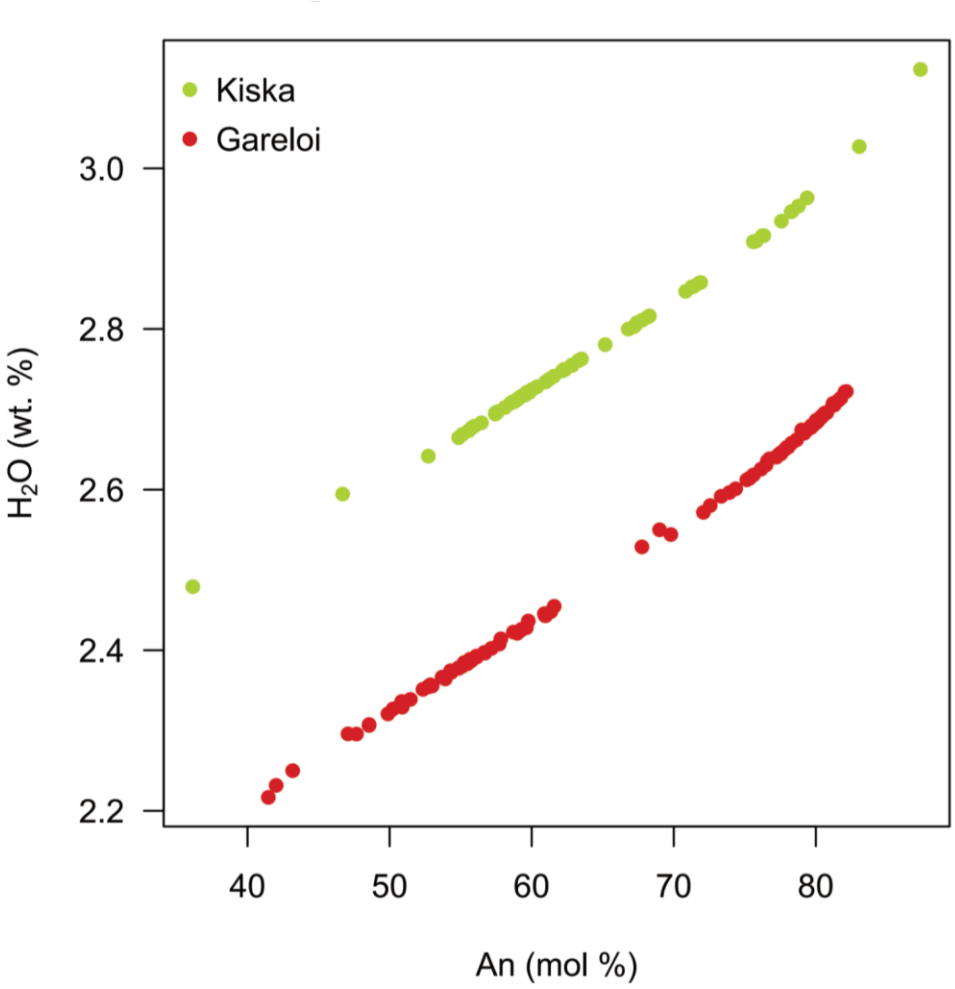
Kiska
Gareloi
3.0
2.8
2.6
2.4
2.2
H2O (wt. %)
40
50
60
70
80
An (mol %)

Figure 25. Harker diagrams of major elements from distal Aleutian samples. Glass compositions are from Table 5 and are indicated by red triangles for Gareloi glass and a green triangle for Kiska glass. MELTS models of isobaric fractional crystallization for Gareloi and Kiska are indicated by the red and green line, respectively. Sample 03GRBB41 was used as a starting composition for Gareloi based on SiO_2, Mg#, and overall fit with other sample data. Sample 15KKMP007-01, a basaltic-andesite was used as a starting composition for Kiska in order to simulate fractional crystallization in a shallow magmatic reservoir to determine if Kiska rocks approximate liquids and can generate a LLD which intersects glass compositions.

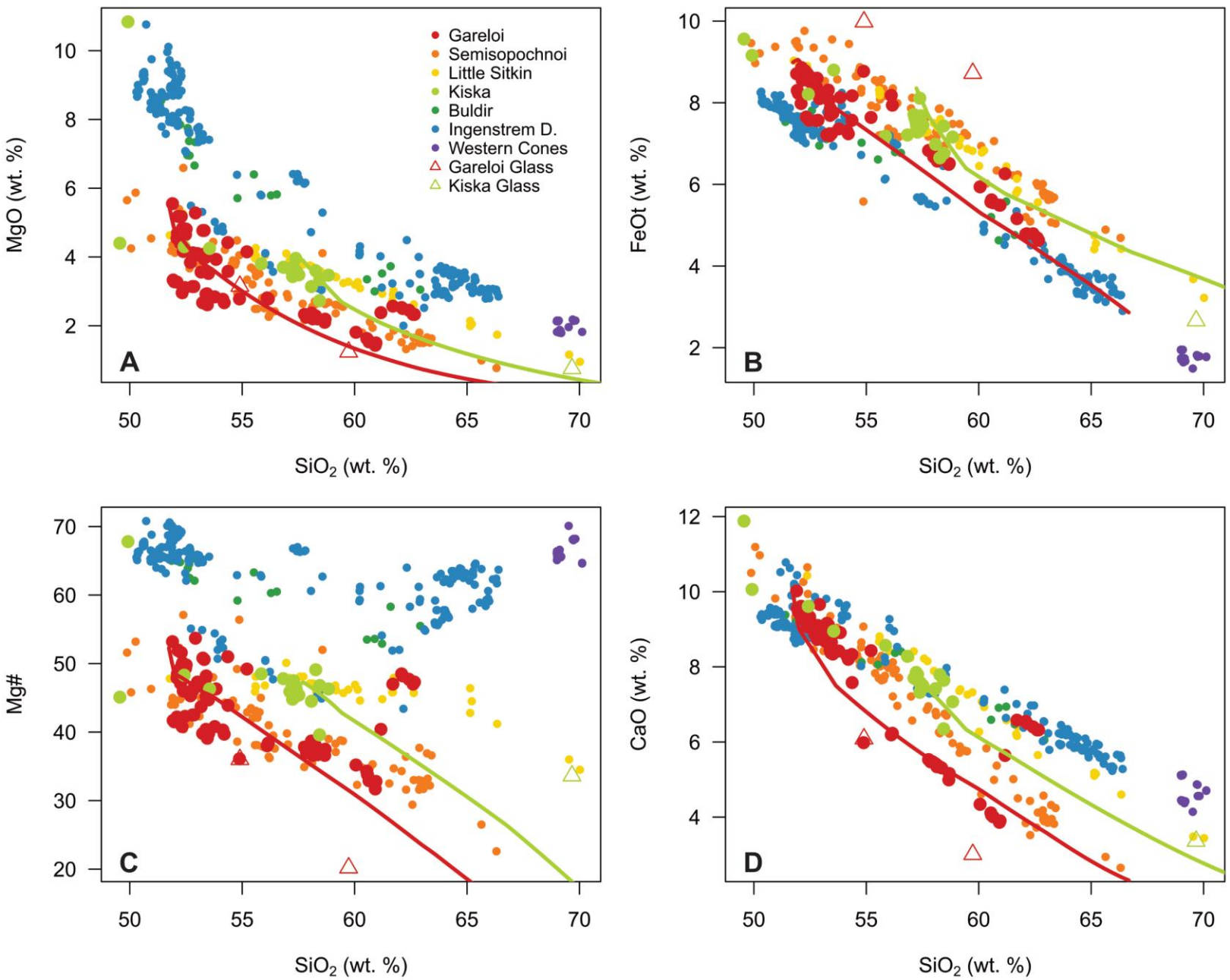
Gareloi
Semisopochnoi
Little Sitkin
Kiska
Buldir
Ingenstrem D.
Western Cones
Gareloi Glass
Kiska Glass
A
B
C
D
MgO (wt. %)
FeOt (wt. %)
Mg#
CaO (wt. %)
SiO2 (wt. %)

Figure 26. Harker diagrams of major elements from distal Aleutian samples. Glass compositions are from Table 5 and are indicated by red triangles for Gareloi glass and a green triangle for Kiska glass. MELTS models of fractional crystallization for Gareloi and Kiska are indicated by the red and green line, respectively. Sample 03GRBB41 was used as a starting composition for Gareloi. The intensive parameters used for the model are a pressure of 1 kbar, fO_2 buffer of QFM+2, and 2 wt. % H_2O. The order of crystallization is clinopyroxene (1128 °C), spinel (1107 °C), plagioclase (1080 °C), olivine (1068 °C), and apatite (918 °C). Sample 15KKMP007-01 was used as a starting composition for Kiska. The intensive parameters used for the model are a pressure of 1 kbar, fO_2 buffer of QFM+2, and 3 wt. % H_2O. The order of crystallization is spinel (1081 °C), orthopyroxene (1063 °C), clinopyroxene (1060 °C), feldspar (1021 °C), and olivine (865 °C). A) Al_2O_3 vs. SiO_2 B) CaO/Al_2O_3 vs. SiO_2 C) Na_2O vs. SiO_2 D) K_2O vs. SiO_2, Low-K, medium-K, and high-K fields are from Gill (1981).

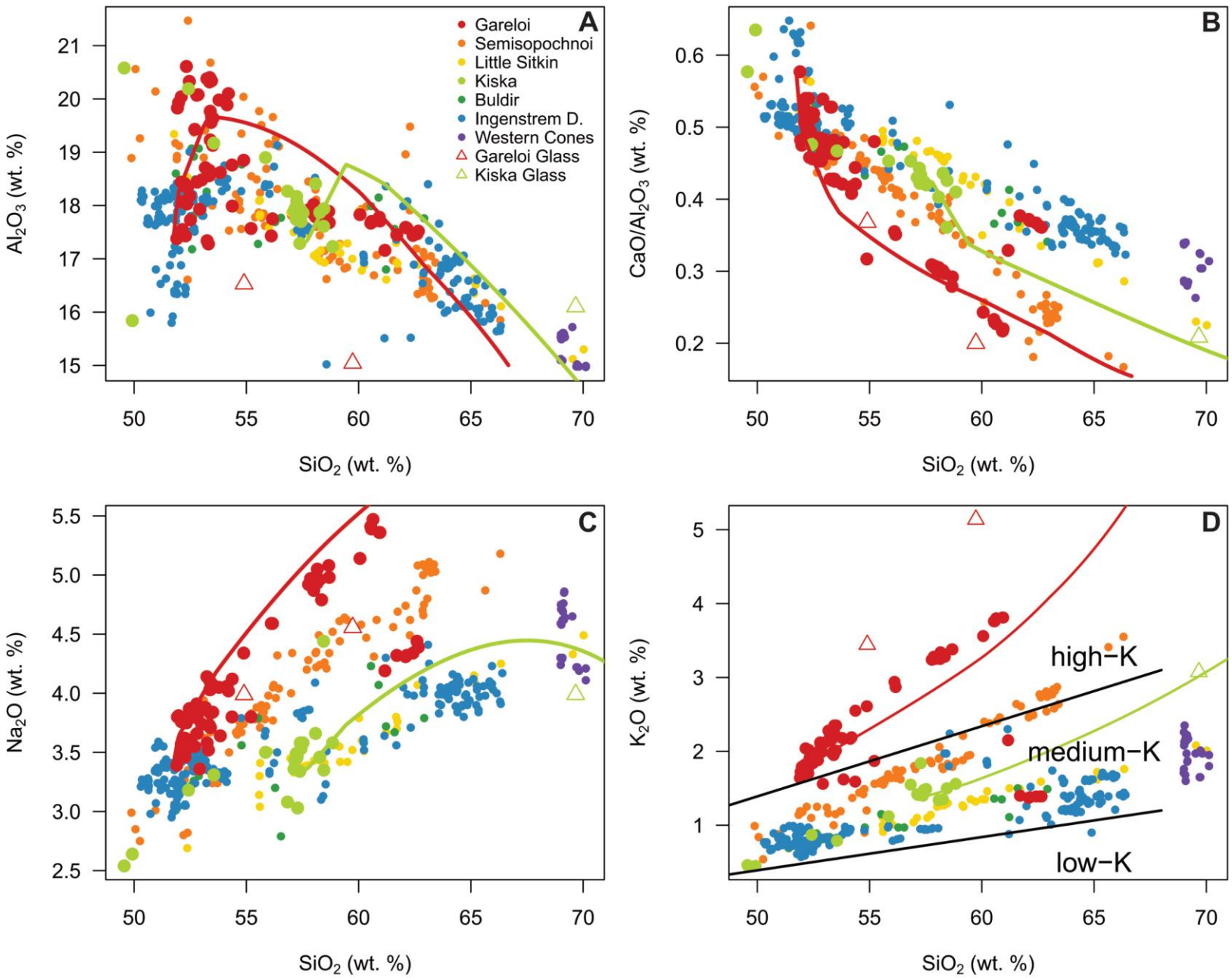
A
Gareloi
Semisopochnoi
Little Sitkin
Kiska
Buldir
Ingenstrem D.
Western Cones
Gareloi Glass
Kiska Glass
Al2O3 (wt. %)
SiO2 (wt. %)
B
CaO/Al2O3 (wt. %)
SiO2 (wt. %)
C
Na2O (wt. %)
SiO2 (wt. %)
D
K2O (wt. %)
high−K
medium−K
low−K
SiO2 (wt. %)

Figure 27. Chemical classification of Aleutian volcanic rocks using TAS (total alkali-silica) diagram after Le Bas et al. (1986). Further subdivisions of TAS diagram are after Le Maitre et al. (2002). Additional Aleutian geochemical data is from Kelemen et al. (2003a).

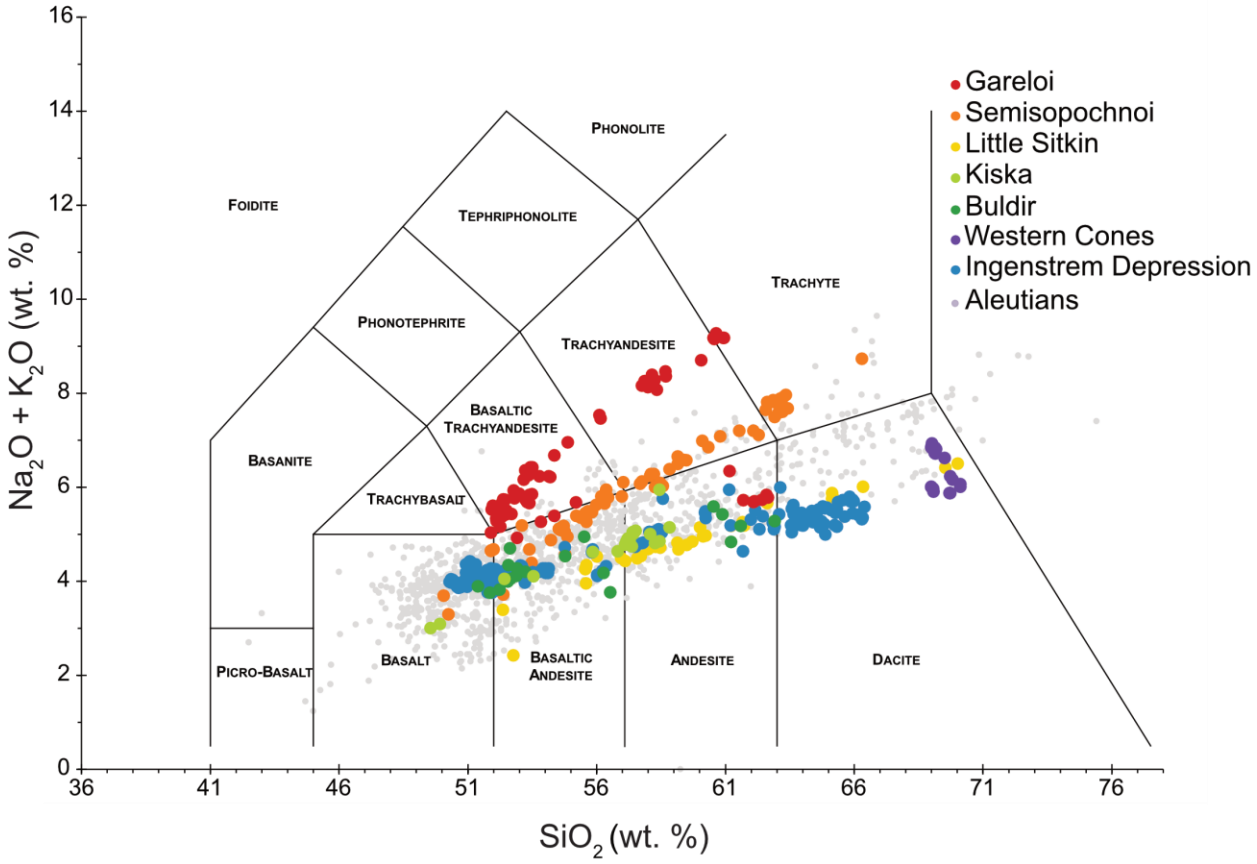

Further Subdivisions	trachybasalt	basaltic trachyandesite	trachyandesite
$Na_2O - 2.0 \geq K_2O$	hawaiite	mugearite	benmoreite
$Na_2O - 2.0 \leq K_2O$	potassic trachybasalt	shoshonite	latite

Gareloi	**Semisopochnoi**
potassic trachybasalt n=1	mugearite n=3
mugearite n=4	latite n=3
shoshonite n=40	benmoreite n=17
latite n=14	

Figure 28. A scree plot and distance biplot from principal component analysis. A) The scree plot depicts the percent of variation explained by each principal component. PC1 accounts for 58% of the explained variation in the dataset while PC2 accounts for 28%. In total, PC1 and PC2 account for 85% of the explained variation in the dataset. Loadings in bold emphasize any variable that contributes more than one variable's worth of information to the principal component. B) A distance biplot with scores sorted by volcanic center. The vectors are loadings that indicate each variable's influence on each respective principal component. PCA 1 is interpreted as representing the differentiation of mafic to felsic magmas. PCA 2 is interpreted as representing the shift from tholeiitic to calc-alkaline magmas.

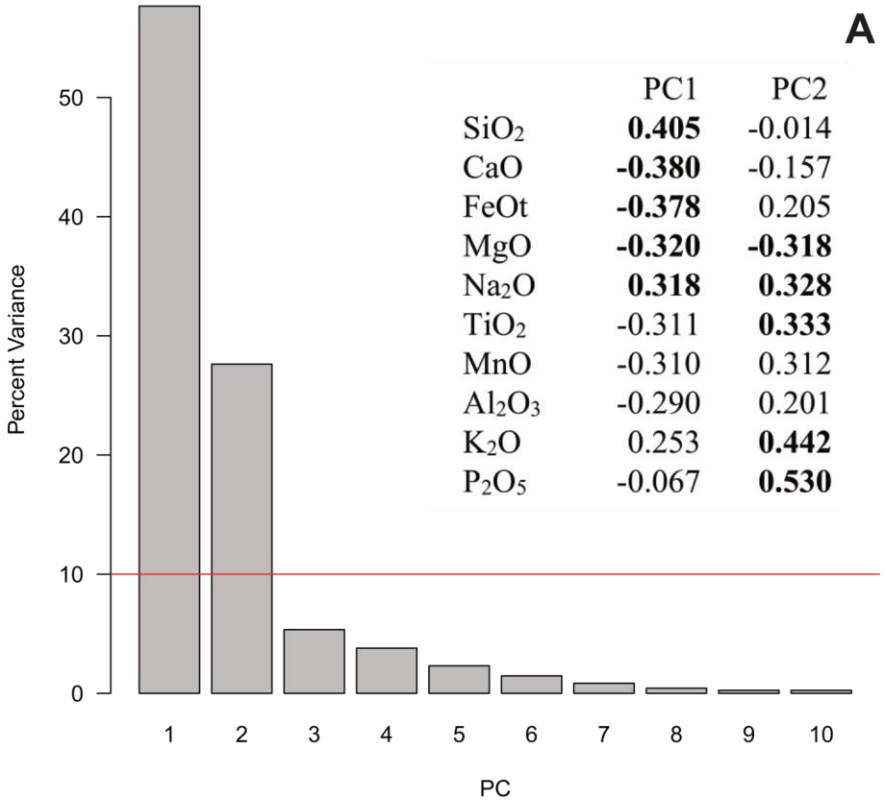

	PC1	PC2
SiO_2	**0.405**	-0.014
CaO	**-0.380**	-0.157
FeOt	**-0.378**	0.205
MgO	**-0.320**	**-0.318**
Na_2O	**0.318**	**0.328**
TiO_2	-0.311	**0.333**
MnO	-0.310	0.312
Al_2O_3	-0.290	0.201
K_2O	0.253	**0.442**
P_2O_5	-0.067	**0.530**

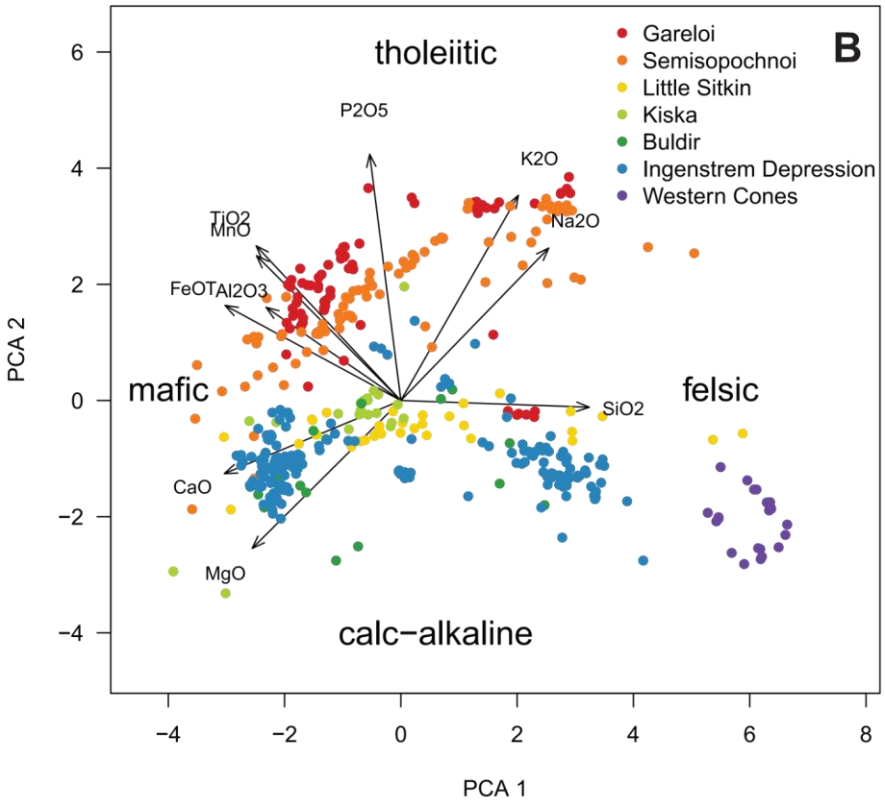

Figure 29. Identification of PC1 representing rock compositions and PC2 representing tholeiitic vs. calc-alkaline differentiation. A) PCA 2 vs. PCA 1 scores (samples) are sorted based off their SiO_2 content and designated as: basalts (<53 wt. % SiO_2); basaltic andesites (53–57 wt. % SiO_2); andesites (57–63 wt. % SiO_2); dacites (63–67 wt. % SiO_2); rhyodacites (67–70 wt. % SiO_2); rhyolite (>70 wt. % SiO_2). One caveat is that evolved samples from Gareloi are transitional between the alkaline and sub-alkaline series. Select Gareloi samples are classified as potassic trachybasalts, mugearites, shoshonites, and latites (Fig. 26; Le Maitre et al., 2002). Select Semisopochnoi samples are classified as mugearites, latites, and benmoreites (Fig. 26; Le Maitre et al., 2002). B) PCA 2 vs. PCA 1 with scores sorted as tholeiitic or calc-alkaline based on the categorization scheme of Miyashiro (1974). The two series overlap at basaltic compositions, but their paths diverge at basaltic-andesite compositions.

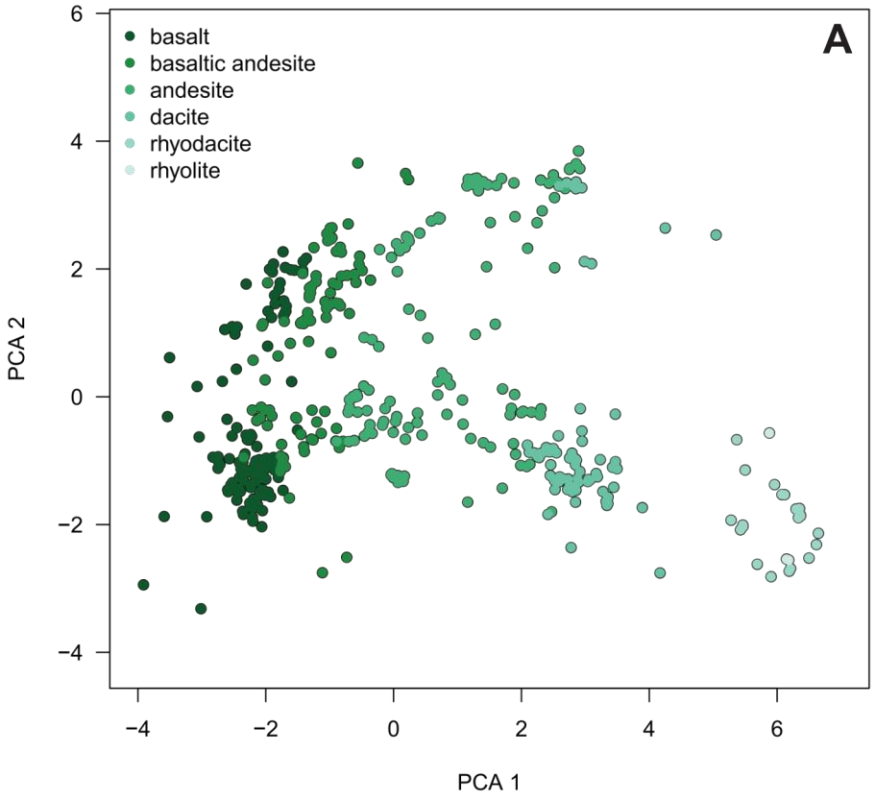
A
basalt
basaltic andesite
andesite
dacite
rhyodacite
rhyolite
PCA 2
PCA 1
6
4
2
0
−2
−4
−4
−2
0
2
4
6

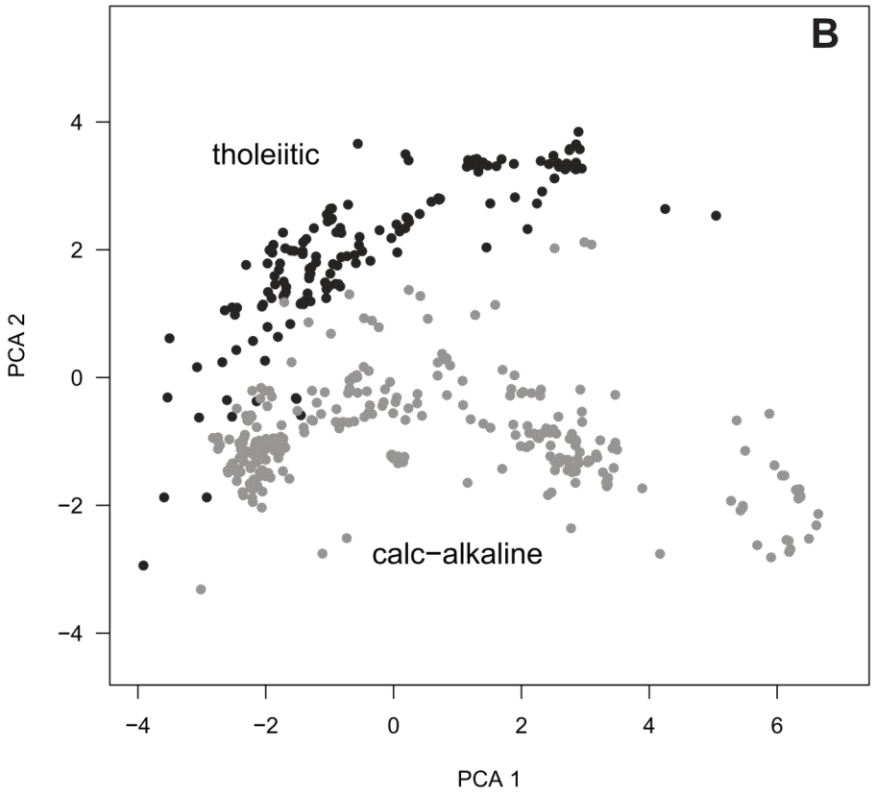
B
tholeiitic
calc−alkaline
PCA 2
PCA 1
4
2
0
−2
−4
−4
−2
0
2
4
6

Figure 30. Amphibole fractionation vs. residual garnet in influencing the geochemistry of distal Aleutian rocks. A) Dy/Yb vs. SiO_2 after Davidson et al. (2007), and B) Dy/Dy* vs. Dy/Yb after Davidson et al. (2013) in which all elemental concentrations are normalized to C1 chondrite values of Sun and McDonough (1989). Dy/Dy* is defined as $Dy \div (La^{4/13}Yb^{9/13})$.

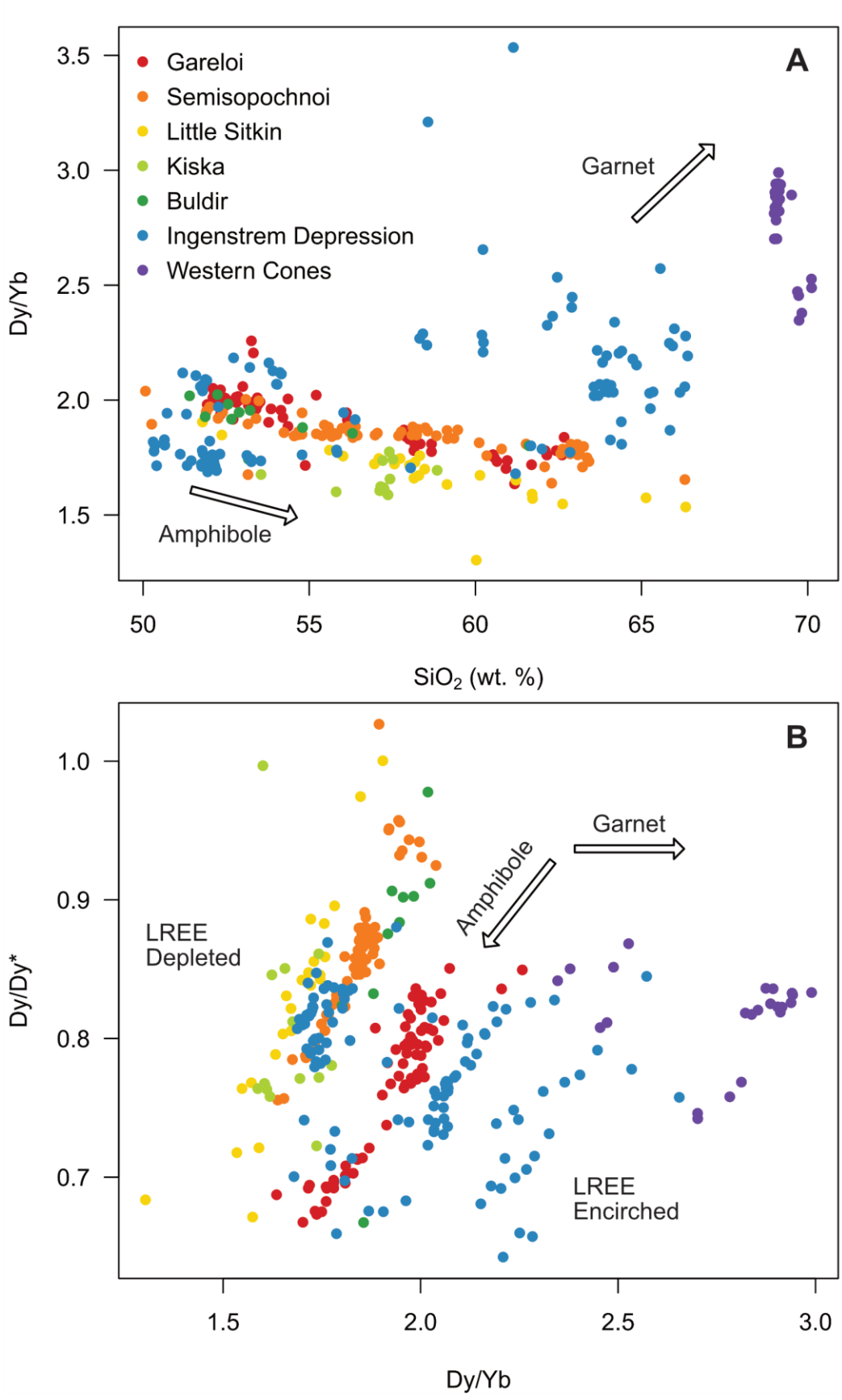
A
Gareloi
Semisopochnoi
Little Sitkin
Kiska
Buldir
Ingenstrem Depression
Western Cones
Garnet
Amphibole
Dy/Yb
SiO2 (wt. %)
B
Garnet
Amphibole
LREE
Depleted
LREE
Encirched
Dy/Dy*
Dy/Yb

Figure 31. REE patterns normalized to the C1 chondrite values of Sun and McDonough (1989) for Gareloi (A), Kiska (B), and Western Cones (C). Data are from Coats et al. (1961), Coombs et al. (2012), Yogodzinski et al. (2015), and Nye et al. (2018).

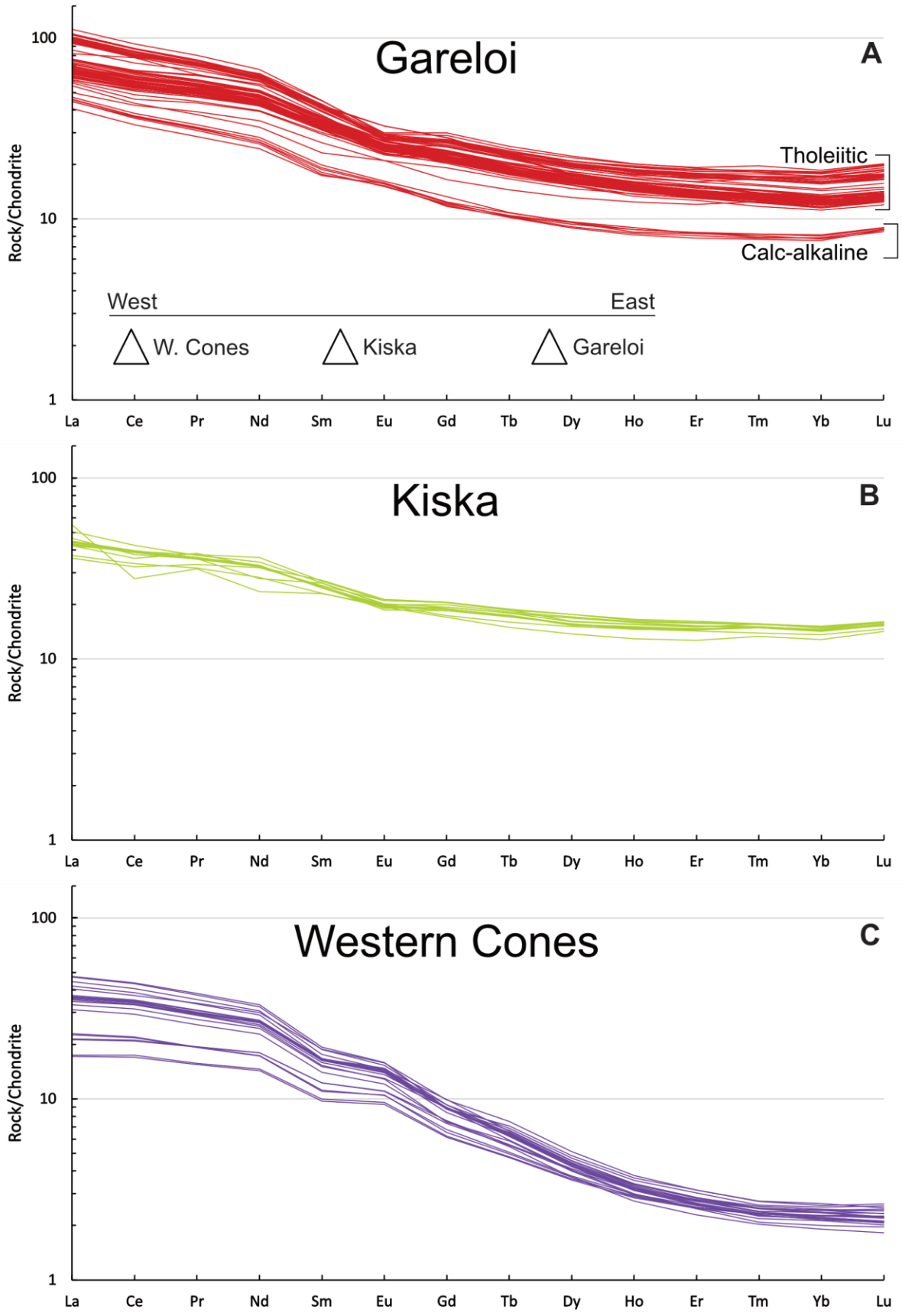
Gareloi
A
Tholeiitic
Calc-alkaline
West
East
W. Cones
Kiska
Gareloi
Kiska
B
Western Cones
C
Rock/Chondrite
100
10
1
La
Ce
Pr
Nd
Sm
Eu
Gd
Tb
Dy
Ho
Er
Tm
Yb
Lu

Figure 32. REE patterns normalized to the C1 chondrite values of Sun and McDonough (1989) for representative distal Aleutian basalts (A), andesites (B), and dacites (C). Data are from Kay and Kay (1994), Yogodzinski et al. (2010, 2015), Coombs et al. (2012, 2018), and Waters et al. (2021).

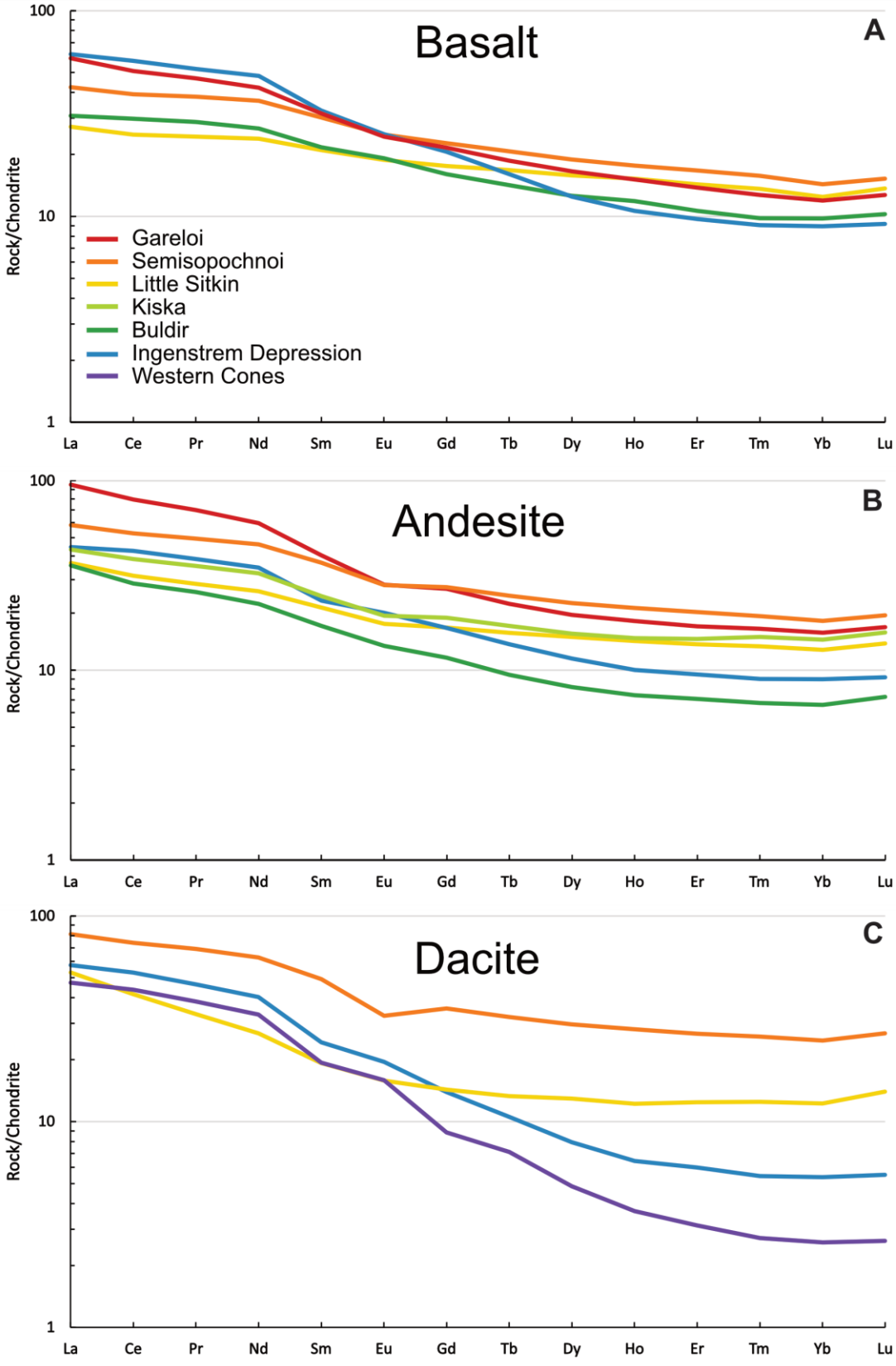
Basalt
A
Andesite
B
Dacite
C
Rock/Chondrite
100
10
1
La
Ce
Pr
Nd
Sm
Eu
Gd
Tb
Dy
Ho
Er
Tm
Yb
Lu
Gareloi
Semisopochnoi
Little Sitkin
Kiska
Buldir
Ingenstrem Depression
Western Cones

Figure 33. Major and trace element plots of distal Aleutian rocks. A) La/Yb vs. SiO_2 for Ingenstrem Depression and Western Cones samples. B) La/Yb vs. SiO_2 for Gareloi-Buldir samples. C) Eu/Eu* vs. SiO_2. Eu/Eu* defined as $Eu_N \div [\sqrt{(Sm_N + Gd_N)}]$ (Taylor and McLennan, 1985) where all elemental concentrations are normalized to the C1 chondrite values of Sun and McDonough (1989). Eu/Eu* >1 indicates plagioclase accumulation while Eu/Eu* <1 indicates plagioclase fractionation. D) Mg# vs. SiO_2.

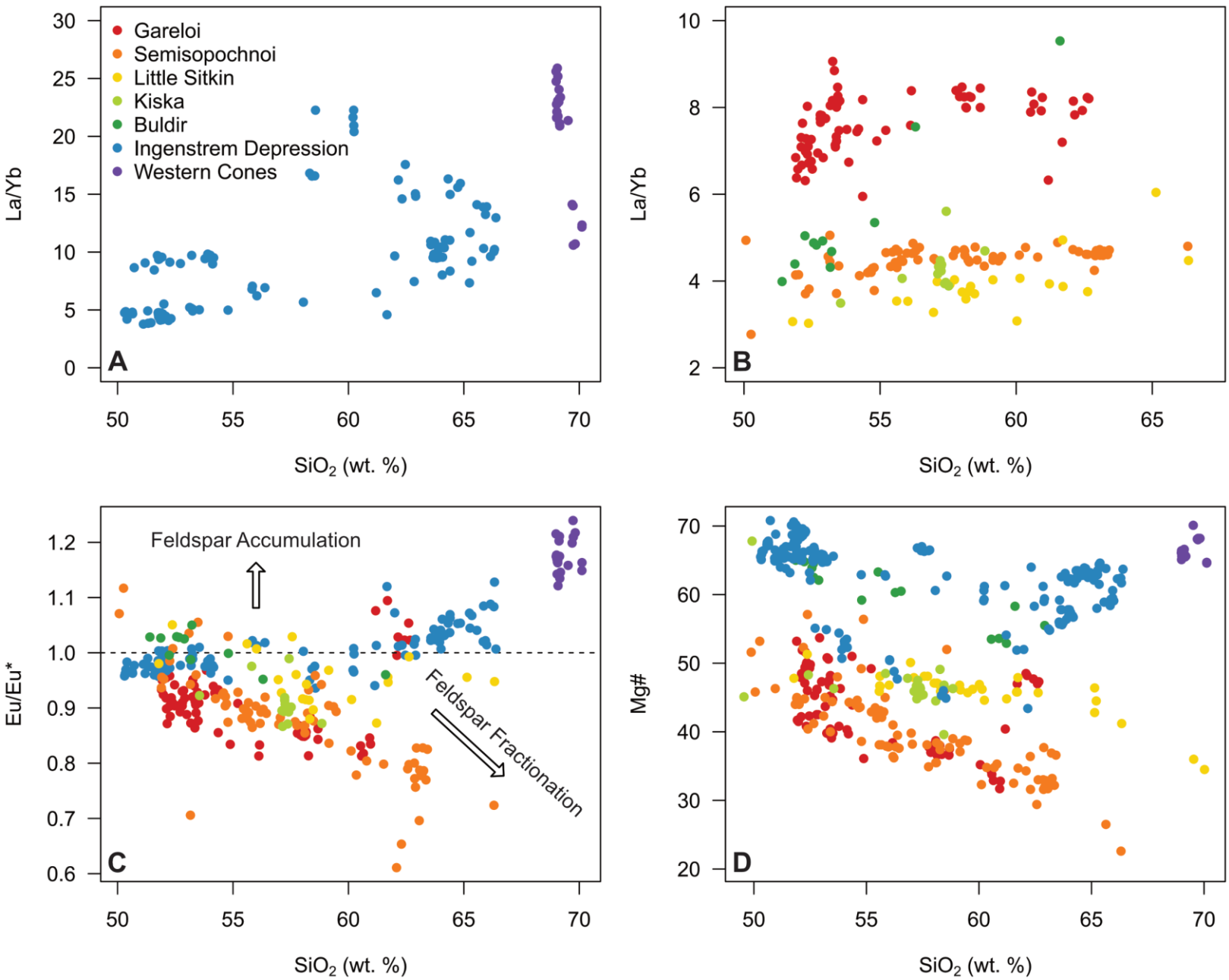
Gareloi
Semisopochnoi
Little Sitkin
Kiska
Buldir
Ingenstrem Depression
Western Cones
La/Yb
SiO2 (wt. %)
A
B
Eu/Eu*
Feldspar Accumulation
Feldspar Fractionation
C
Mg#
D

Figure 34. Trace element plots of distal Aleutian samples. A) Sr/Y vs. Mg#. Sr/Y >50 is indicative of an eclogite melt component (Kelemen et al., 2003b). B) Th/La vs. Mg#. Th/La correlates with Pb radiogenic isotopic concentration within the Aleutians and is therefore inferred to represent a terrigenous subducted sediment component (Kelemen et al., 2003b). C) Ba vs. Sr. The fractionation vector inset is from Rollinson and Pease (2021). D) U/Th vs. Th. U/Th vs. Th has been used to constrain the extent sediments and fluids derived from the subducted slab have influenced arc magmatic compositions (Hawkesworth et al., 1997).

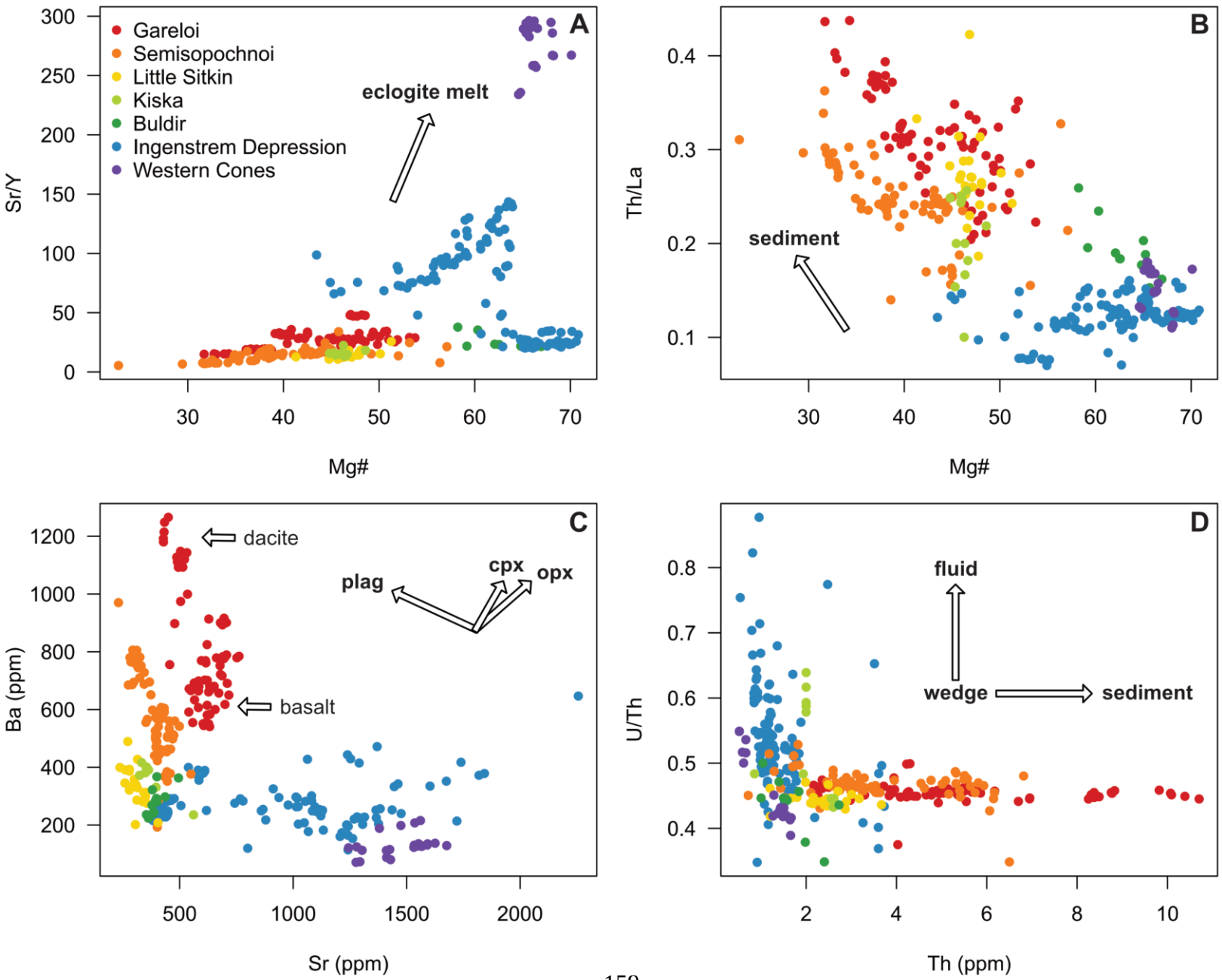
A
Gareloi
Semisopochnoi
Little Sitkin
Kiska
Buldir
Ingenstrem Depression
Western Cones
eclogite melt
Sr/Y
Mg#
B
sediment
Th/La
Mg#
C
dacite
plag
cpx
opx
basalt
Ba (ppm)
Sr (ppm)
D
fluid
wedge
sediment
U/Th
Th (ppm)

Figure 35. Anhydrous phase relations of high-Mg basalt of Makushin sample MK-15 as a function of temperature and pressure after Gust and Perfit (1987). Both Kiska and Gareloi magmas are derived from a shared high-Al basalt parent. The green arrow represents the differentiation path of Kiska magmas, and the red arrow represents the differentiation path of Gareloi magmas.

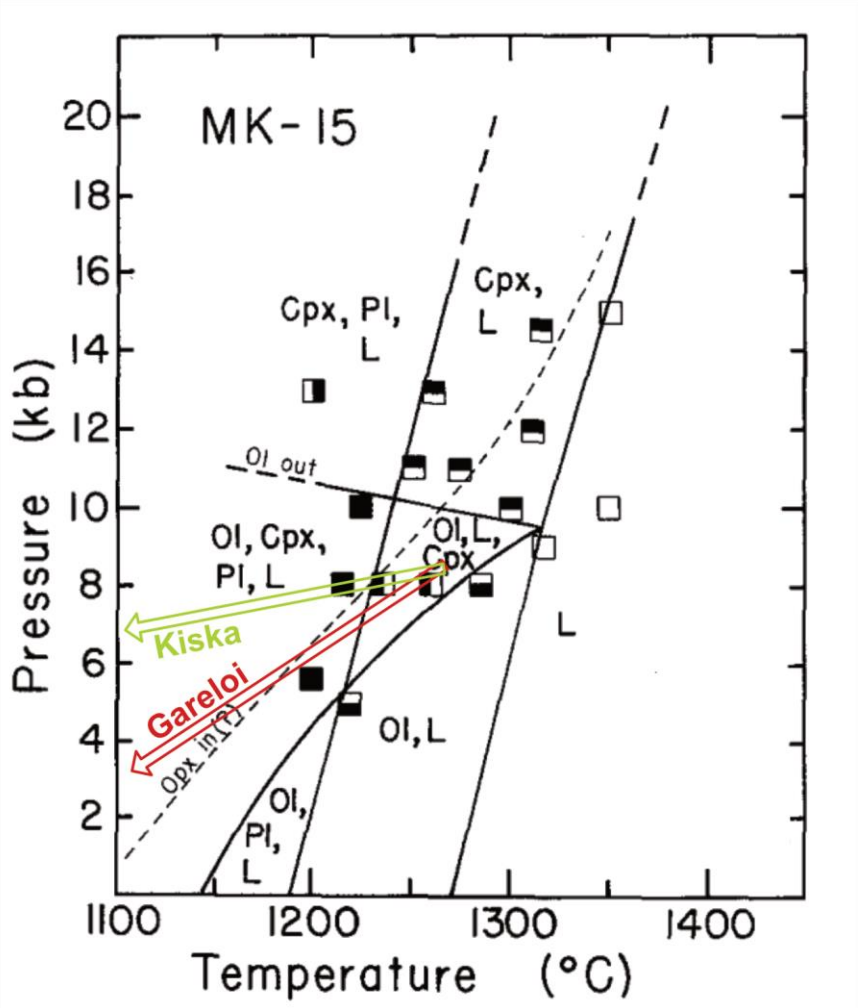
MK-15
Pressure (kb)
Temperature (°C)
20
18
16
14
12
10
8
6
4
2
1100
1200
1300
1400
Cpx, Pl, L
Cpx, L
Ol out
Ol, Cpx, Pl, L
Ol, L, Cpx
L
Kiska
Gareloi
Opx in(?)
Ol, L
Ol, Pl, L